

Annual Report
Jahresbericht

2003



WALTHER-MEISSNER-INSTITUT
für Tieftemperaturforschung
Bayerische Akademie der Wissenschaften



Contact:

Prof. Dr. Rudolf Gross
Walther–Meissner–Institut für Tieftemperaturforschung
Bayerische Akademie der Wissenschaften
and
Lehrstuhl für Technische Physik – E23
Technische Universität München

Address:

Walther–Meissner–Str. 8	Phone:	+49 – (0)89 289 14201
D - 85748 Garching	Fax:	+49 – (0)89 289 14206
GERMANY	e–mail:	Rudolf.Gross@wmi.badw.de
	WWW–address:	http://www.wmi.badw.de

Secretary's Office:

Jutta Laaser	Phone:	+49 – (0)89 289 14202
	Fax:	+49 – (0)89 289 14206
	e–mail:	Jutta.Laaser@wmi.badw.de

Emel Dönertas	Phone:	+49 – (0)89 289 14205
	Fax:	+49 – (0)89 289 14206
	e–mail:	Emel.Doenertas@wmi.badw.de

Preface

The Walther–Meissner–Institute for Low Temperature Research (WMI) is operated by the Commission for Low Temperature Physics of the Bavarian Academy of Sciences. At the same time the WMI is the host institute of the chair for Technical Physics (E 23) of the Technical University of Munich with the director of the WMI being ordinarius at the Faculty of Physics of the Technical University of Munich. The WMI carries out research projects at low and ultra–low temperatures and supplies liquid helium to both universities in Munich. It also provides the technological basis for low and ultra–low temperature techniques and methods. The research program of the WMI is devoted to both **fundamental** and **applied research** in the field of **low temperature solid state physics**.

With respect to **basic research** the main focus of the WMI is on

- superconductivity and superfluidity,
- magnetism and spin transport,
- mesoscopic systems and quantum phenomena in nanostructures,
- and the general properties of metallic systems at low and very low temperatures.

The WMI also conducts **applied research** in the fields of

- solid state based quantum information processing systems,
- superconducting and spintronic devices,
- oxide electronics,
- and the development of low and ultra low temperature systems and techniques.

With respect to **materials science** the research program is focused on

- the synthesis of superconducting and magnetic materials,
- the single crystals growth of oxide materials,
- and the epitaxial growth of complex oxide heterostructures.

In 2003 the set-up of the new experimental facilities and the reconstruction of the laboratories has almost been completed. In particular, the new clean room facility with the electron beam and the optical lithography and the new thin film laboratory could be routinely operated. The new laboratory for the synthesis of bulk materials and single crystal growth has been finished and the new four-mirror image furnace has already been successfully used for the growth of various oxide materials using the travelling solvent floating zone technique. Finally, a new dilution refrigerator system developed for the study of coherent quantum phenomena in superconducting systems has been completed and successfully operated in a HF shielded room.

The various research projects of the WMI have been continued in 2003 and several new medium and long term projects have been successfully started. In particular, the WMI took the leadership in setting up the new **Collaborative Research Center 631** (SFB 631) on *Solid State Based Quantum Information Processing: Physical Concepts and Materials Aspects*. The SFB 631 was installed by the German Science Foundation effective in July 1, 2003. Within 15 projects research groups from the Bavarian Academy

of Sciences, the Technical University of Munich, the Ludwig-Maximilians-University, the Max-Planck-Institute for Quantum Optics, as well as the University of Regensburg and the University of Augsburg are collaborating. In addition to 30 senior scientists, more than 30 PhD and diploma students as well as a large number of guests are involved in the research activities. The goal of this long-term research effort is to develop the physical concepts and materials aspects for scalable quantum information processing systems by bringing together research groups with competence in the fields of experimental and theoretical solid state physics, materials and nanotechnology, quantum information theory, low temperature techniques and quantum optics.

Beyond the SFB 631, the WMI has started a new research project on *New Functional Thin Film Systems Based on Artificial Heterostructures of Transition Metal Oxides* within the **Priority Programme 1157** on *Integrated Electroceramic Functional Systems*. The Priority Programme 1157 has been installed by the German Science Foundation in 2003 and is planned to continue until 2008. The goal of the project is to integrate electroceramic materials with different properties in artificial heterostructures to achieve new physical properties and new functions. The WMI also took the leadership in setting up a new **Research Unit** of the German Science Foundation on *High Temperature Superconductivity*. Within this Research Unit groups from the WMI, the IFW Dresden, the Max-Planck-Institute for Solid State Research at Stuttgart and the University of Würzburg are planning to make a coordinated effort to further clarify the mechanism of high temperature superconductivity. The programme of the new Research Unit already has been evaluated by a reviewing committee in November 2003 and has been recommended to start in 2004.

The research at the WMI has been very successful in 2003 as demonstrated by more than 40 scientific papers (with several articles in *Nature* and *Physical Review Letters*) and a large number of invited presentations at national and international conferences as well as seminar talks and colloquia. Throughout 2003, an average of 13 scientific staff members, 18 members of the administrative and technical staff, 14 doctorate candidates, 12 diploma candidates and more than 20 short and long-term guests belonged to the institute. Of course, the scientific productivity of the WMI would not be possible without the collaborative atmosphere, the high motivation of our research and technical staff and the support of various funding agencies. In particular, we acknowledge the financial support from the Bavarian Academy of Sciences, the German Science Foundation, the Bavarian Ministry for Science and Arts, the BMBF and the EU. Unfortunately, the general decrease of the budgets available for science and technology in Germany also strongly affects the research at WMI. In 2003 the WMI has to suffer a 20% cut-back of its annual total budget. Since it was impossible to reduce the running costs of the institute (electricity, heating, water etc.) by this amount, a much larger reduction of the “research budget” was caused. On the short hand, this reduction at least in part can be compensated by the extra money coming from the acquired research projects. However, on the long term similar cut-backs as in the years 2002 and 2003 will continuously destroy the apparatus and technological basis of the WMI and in turn its competitiveness in acquiring external research projects.

This Annual Report gives an overview on the scientific results of the WMI, which in many cases have been obtained within joint national and international research projects and in close collaboration with international guests. Our 2003 Annual Report is intended to provide an overview on our work to our friends and partners in research and industry and thereby to intensify our numerous collaborations. I would be particularly pleased, if the report would stimulate new collaborations. In order to be useful also for our numerous international partners the report is written in English.

I finally would like to thank all the colleagues, guests, students, post-docs and cooperating partners, who contributed to the success of our work within the last year, and last but not least all our friends and

sponsors for their interest, trust and continuous support.

A handwritten signature in blue ink, appearing to read 'R. Gross', with a large circular flourish above the 'o'.

Rudolf Gross

Garching, December 2003

Contents

Preface	1
The Walther–Meissner–Institute	7
Reports:	9
Basic Research	9
The New Collaborative Research Center 631	9
Superconductivity in the Charge Density Wave Organic Compound α -(BEDT-TTF) ₂ KHg(SCN) ₄	12
Orbital Quantization in the High Magnetic Field State of a Charge-Density-Wave System	15
Dynamical Properties of Stripes in $\text{La}_{2-x}\text{Sr}_x\text{CuO}_4$	18
Viscous Transport in Dirty Fermi Superfluids	20
Superconductivity in a Hydrated Layered Cobalt Oxide	22
Magnetic Interactions in the Double Perovskites	23
Study of the Magnetic Properties of Nb-based Double Perovskites	31
Magnetization of the Nuclear Spin Ordered Phases of Solid ³ He: Pulsed NMR and SQUID Magnetometry	34
Application Oriented Basic Research	39
Observation of Phase Coherent Transport in Superconductor/Manganite Junctions	39
Single Charging Effects in (Ferromagnetic) Metallic Nanostructures	43
Room Temperature TMR-effect in Magnetite Based Magnetic Tunnel Junctions	47
Diffusion and Segregation Effects in Doped Manganite/Titanate Heterostructures	50
Mn-doped ZnO - A ferromagnetic Semiconductor?	54
Hydrogen control of ferromagnetism in a dilute magnetic semiconductor	56
Diffusion Coefficients of Interlayer Water Molecules in Graphite Oxide	59

Materials and Experimental Techniques	61
Superconducting Qubits: Setup for Experimental Characterization	61
Epitaxial Growth of Sr ₂ CrWO ₆ Thin Films	65
Single Crystal Growth of Cuprate Superconductors	68
Redox Reactions and Iron Uptake in Vermiculites from Spain	70
Dilution Refrigerator with Pulse-Tube Precooling: a "Dry" Millikelvin Cooler	72
Experimental Facilities	75
Publications	87
Completed Diploma and Ph.D. Theses	91
Research Projects and Cooperations	93
Invited Conference Talks and Seminar Lectures	98
Seminars, Courses, Lectures and other Scientific Activities	101
Staff of the Walther-Meissner-Institute	107
Guest Researchers	108
Commission for Low Temperature Physics	109

The Walther–Meissner–Institute

The Walther–Meissner–Institute for Low Temperature Research (WMI) is operated by the Commission for Low Temperature Physics of the Bavarian Academy of Sciences (BAW). The Commissions (Research Groups) of the Bavarian Academy are set up in order to carry out long–term projects, which are too ambitious for the lifetime or capacity of any single researcher, or which require the collaboration of specialists in various disciplines. At present, the Bavarian Academy of Sciences consists of 36 Commissions with more than 300 employees. The WMI also is the host institute of the chair for Technical Physics (E 23) of the Technical University of Munich. The director of the WMI at the same time is ordinarius at the Faculty of Physics of the Technical University of Munich.

The research at the Walther–Meissner–Institute is focused on low temperature physics (see reports below). The WMI also develops systems and techniques for low and ultra–low temperature experiments. As typical examples we mention a dry mK–system that can be operated without liquid helium by using a pulse–tube refrigerator for precooling, a nuclear demagnetization cryostat for temperature down to below 100 μ K, or very flexible dilution refrigerator inserts for temperatures down to about 20 mK fitting into a 2 inch bore. These systems have been engineered and fabricated at the WMI. Within the last years, several dilution refrigerators have been provided to other research groups for various low temperature experiments. The WMI also operates a helium liquifier with a capacity of more than 120.000 liters per year and supplies both Munich universities with liquid helium. To optimize the transfer of liquid helium into transport containers the WMI has developed a pumping system for liquid helium that is commercialized in collaboration with a company.

The individual research groups of the WMI offer a wide range of attractive research opportunities for diploma (graduate) students, PhD students and postdoctoral fellows. The WMI is equipped with state of the art facilities for the preparation and characterization of superconducting and magnetic materials as well as for various low and ultra–low temperature experiments. The main experimental and technological resources of the WMI are listed in the following.

Materials Preparation and Fabrication of Nanostructures

- Laser Molecular Beam Epitaxy system for oxide heterostructures (equipped with in–situ RHEED, AFM/STM system, atomic oxygen source, laser heating system, metallization)
- magnetron sputtering system for oxide heteroepitaxy (equipped with four sputtering guns and an oxygen ion gun)
- ion beam sputtering system
- metallization system (equipped with e–gun and thermal evaporators)
- ion beam etching system equipped with a LN₂ cooled sample holder
- polishing machine for substrate preparation
- ultrasonic bonding machine
- 50 m² class 1000 clean room facility
- optical lithography (Süss maskaligner MJB 3, projection lithography)
- electron beam lithography (based on Philips XL 30 SFEG scanning electron microscope and Raith Elphy Plus lithography system including a laser stage)
- four-mirror image furnace for crystal growth

Characterization

- 2–circle x–ray diffractometer (Bruker D8 Advance, sample temperature up to 1 600°C)

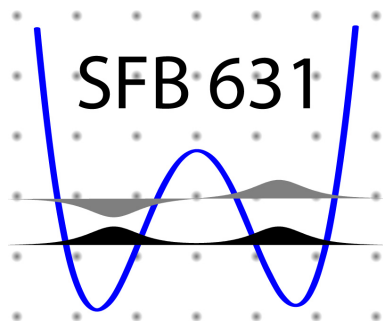
- high resolution 4-circle x-ray diffractometer (Bruker D8 Discover)
- scanning electron microscope with EDX analysis
- AFM/STM system
- two Raman spectroscopy systems (1.5 to 300 K, in-situ sample preparation)
- SQUID magnetometer (1.5 to 700 K, up to 7 Tesla)
- several high field magnet systems (up to 17 Tesla)
- experimental set-ups for the measurement of noise including low noise SQUID amplifiers and signal analyzers
- high frequency network analyzer (up to 40 GHz) for the determination of high frequency parameters

Low temperature systems and techniques

- several $^3\text{He}/^4\text{He}$ dilution refrigerators inserts for temperatures down to 10 mK
- “dry” mK-cooler based on a dilution refrigerator with pulse-tube precooling
- ultra-low temperature facility for temperatures down to below $100\ \mu\text{K}$ based on a nuclear demagnetization cryostat
- experimental set-ups for the measurement of specific heat, magnetization, thermal expansion as well as electrical and thermal transport properties as a function of temperature, magnetic field and pressure

The New Collaborative Research Center 631

Rudolf Gross, Achim Marx, Matthias Opel¹



The Collaborative Research Center 631 (SFB 631) on *Solid State Based Quantum Information Processing: Physical Concepts and Materials Aspects* was installed by the German Science Foundation effective in July 1, 2003. The Walther-Meissner-Institute was one of the main actors in setting up the new Collaborative Research Center 631. It was coordinating the research programme and provides the spokesman of the SFB 631. Within 15 projects research groups from the Walther-Meissner-Institute, the Technical University of Munich, the Ludwig-Maximilians-University, the Max-Planck-Institute for Quantum Optics, as well as the University of Regensburg and

the University of Augsburg are collaborating (see Fig. 1). In addition to 30 senior scientists, more than 30 PhD and diploma students as well as a large number of guests are involved in the research activities.

The research activities within the SFB 631 are directed towards the interdisciplinary research field of *Solid State Based Quantum Information Processing*, which is involving ideas and concepts from information theory, physics, mathematics and materials science. This research initiative is aimed at the basic understanding of the fascinating physics as well as the materials and technological aspects of solid state based quantum information processing. The vision is to provide the physical concepts and technological basis required for the transition from classical to quantum mechanical information processing (see Fig. 2). The key questions to be attacked within the SFB 631 are:

- How can we realize solid state based quantum bits with sufficiently large quantum coherence by using?
- How can we control, manipulate, couple and effectively read out these phase coherent quantum states?
- How can we scale individual solid state based quantum bits to more complex systems?

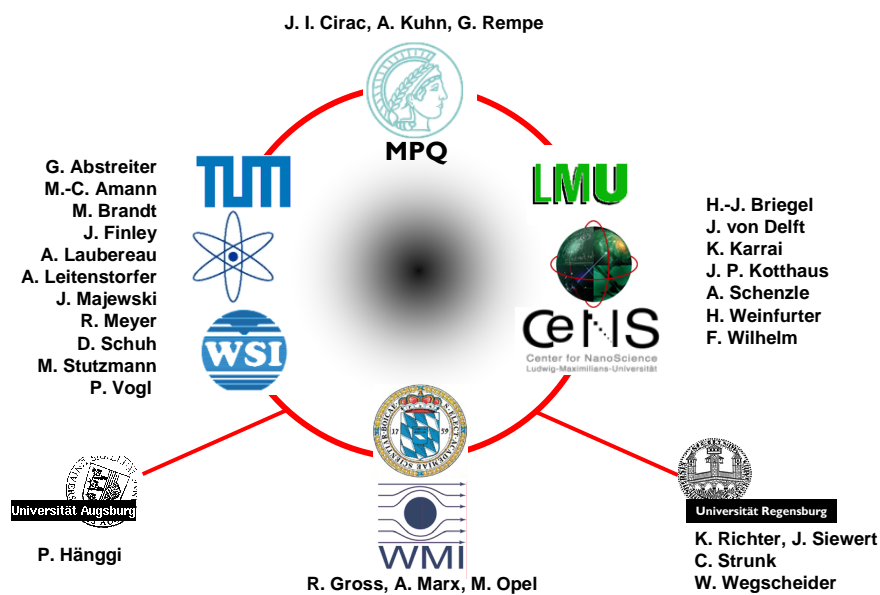


Figure 1: The institutions participating in the new Collaborative Research Center 631.

¹This work is supported by the Deutsche Forschungsgemeinschaft through SFB 631.

- Which concepts can we employ to reduce decoherence?
- Which degrees of freedom in solid state systems are most suitable for the implementation of solid state based quantum bits?
- How can we solve the materials issues and technological problems showing up in the realization of solid state based quantum bits?
- How can we establish an interface between solid state based qubits and quantum communication systems?

Vision: from mechanical to quantum mechanical information processing

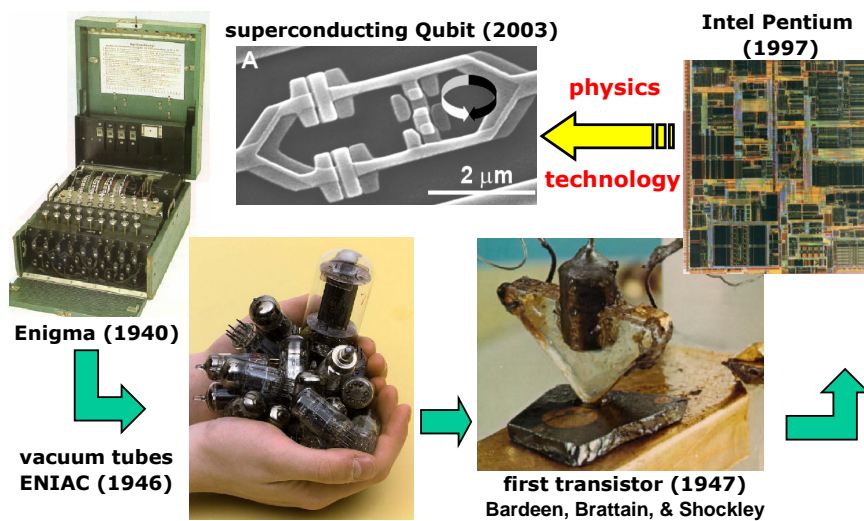


Figure 2: One of the main visions of the new Collaborative Research Center 631 is to provide the physical concepts and technologies required for the step from mechanical to quantum mechanical information processing.

implementation of solid state based quantum bits. In this way we can approach the vision of realizing a useful quantum information system including quantum computing and quantum communication.

Solid state based quantum information processing systems are promising, since they can lead to scalable systems with short quantum-gate switching times. However, at the same time solid state based systems often suffer from the problem of strong coupling to the environment, which usually leads to a fast decoherence of the involved quantum states. The research projects A3/A4 and C5 at the WMI are aiming at the development and understanding of qubits based on superconducting and spin systems.

The research objectives of project A3/A4 at WMI are focussed on the fabrication and characterization of superconducting phase qubits involving π -Josephson junctions as phase batteries. The goal is to obtain in this way naturally degenerate two level quantum systems as the basis for calm qubits with long phase coherence time. The phase qubits will be implemented using both metallic and oxide superconductors and studied with respect to their suitability for quantum information processing. Here, priority is given to the clarification of the physical properties of the phase qubits as well as the analysis of decoherence. Our research activities are aiming at the optimization of phase qubits and the peripheral circuits. Moreover, methods for the manipulation of the qubits as well as concepts for the coupling of two qubits have to be developed and tested.

To answer these question research activities in the fields of quantum information theory, experimental and theoretical solid state physics, quantum optics, materials science and nanotechnology are coordinated (see Fig. 3). The long-term goal of the coordinated research within SFB 631 is to develop a deep understanding of physical concepts of solid state based quantum information processing and to establish the materials and technology basis for a successful imple-

The research objective of project C5 is focused on the experimental study of individual electron spins in semiconductor nanostructures employing electrical transport. Here, the spin degree of freedom is accessed via the charge channel by using the Pauli exclusion principle, which is tightly linking the spin and charge degree of freedom. Individual spins in nanostructured solids represent interesting systems for the

implementation of qubits. In particular, the long phase decoherence time of spins in semiconductors indicates that it may be possible to realize spin-based quantum information processing systems. The aim of project C5 is to get information on the properties and coherence of spin states in semiconductor nanostructures by performing electrical measurements. Priority is given to the initialization and read-out of spin states as well as to the determination of the transverse spin relaxation time.

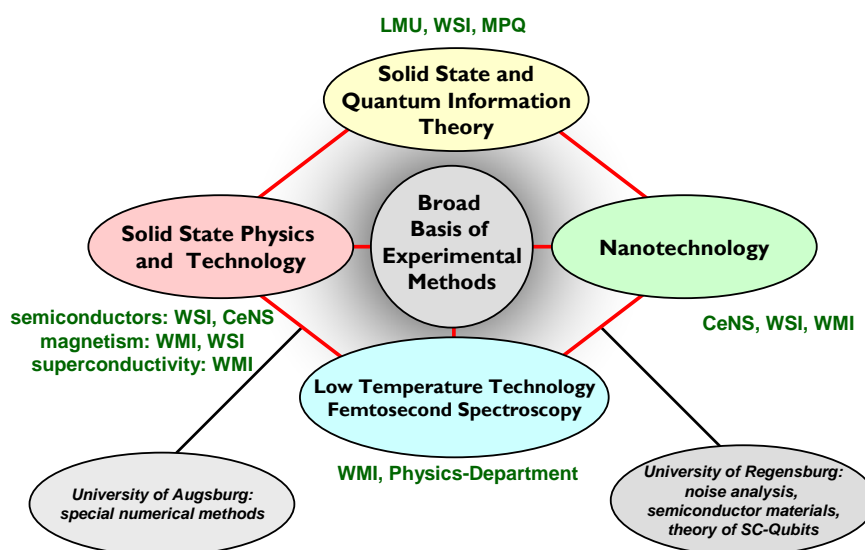


Figure 3: Different fields of competence required for the interdisciplinary research goals are brought together within the new SFB 631.

Superconductivity in the Charge Density Wave Organic Compound α -(BEDT-TTF) $_2$ KHg(SCN) $_4$

D. Andres, M. Kartsovnik, W. Biberacher, K. Neumaier, E. Schubert

The layered organic metal α -(BEDT-TTF) $_2$ KHg(SCN) $_4$ has a strongly anisotropic electron system, with closed cylinders and open sheets on its Fermi surface (FS). The sheets correspond to a quasi-one-dimensional (Q1D) electron band. It emerges due to an enhanced electron transfer integral in the crystallographic a -direction between the organic BEDT-TTF molecules, resulting in a chain-like coupling within the conducting plane. At about 8 K there is a phase transition to a charge-density wave (CDW) state [1], in which the sheets on the FS become nested and the Q1D carriers become gapped. The system, however, keeps its metallic character due to the remaining Fermi surface from the second conducting band. Remarkably, the iso-structural salt α -(BEDT-TTF) $_2$ NH $_4$ Hg(SCN) $_4$ (hereafter we refer to both compounds as NH $_4$ - and K-salt) does not undergo a density wave transition but instead becomes superconducting (SC) at ≈ 1 K. The absence of a density wave is interpreted to be due to a higher interchain coupling of the organic molecules within the layers [2], which strongly deteriorates the nesting conditions of the open sheets of the FS. Moreover, it has been shown [3] that by tuning the ratio of the inplane lattice constants c/a under uniaxial strain a density wave can be even (i) induced in the NH $_4$ -compound and (ii) suppressed in the K-compound with a SC state being stabilized at ≈ 1 K. Similarly, hydrostatic pressure turns out to deteriorate the nesting conditions in the K-salt, and at about $P = 2.5$ kbar the density wave is completely suppressed [4] a normal metallic (NM) state being stabilized. Superconductivity was also found in hydrostatic pressure studies at $T < 300$ mK [5]. Remarkably, it was shown to exist in the whole measured pressure range up to 4 kbar, i.e. it exists both within the CDW as well as in the NM regimes. Since superconductivity is theoretically proposed to become strongly suppressed by the presence of a CDW system [6], the question arises how these states can coexist in the title compound.

As shown in Fig. 1, the resistive SC transition starts to broaden on entering the CDW state with lowering the pressure. At ambient pressure no zero-resistance is observed, but a slight decrease of the resistance, that can easily be suppressed by magnetic field or higher currents, indicates an incomplete transition to the SC state. The latter observation is in agreement with the previous ambient pressure results by Ito *et al.* [7]. As already shown in last year's report, the SC transitions are found to be strongly sample dependent. To demonstrate this, an example of a zero-pressure transition on another sample is presented in the inset of Fig. 1. The resistance of this sample approaches zero at 20 mK. This however does not mean that the whole sample is in the SC state: first d.c. magnetization measurements performed on the same sample down

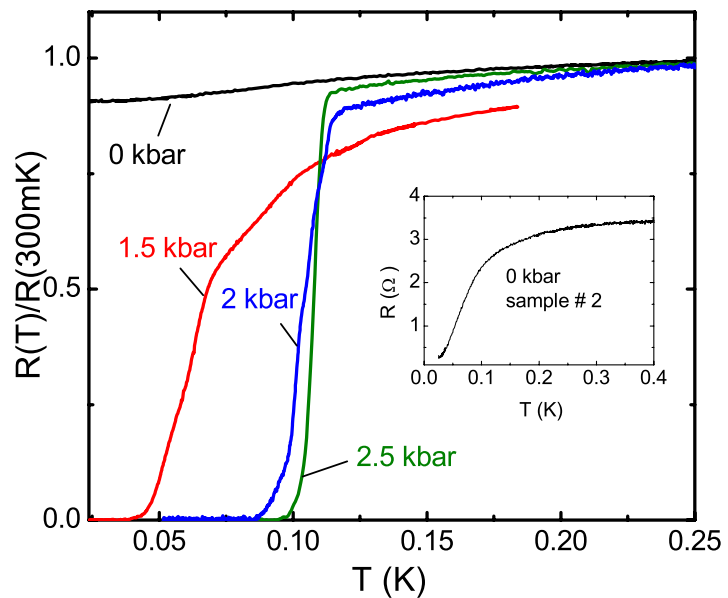


Figure 1: Superconducting transitions seen in the interlayer resistance at different pressures within the CDW state. The inset shows the transition at ambient pressure for another sample.

to 6 mK using the SQUID technique have not shown any Meissner signal at all. Therefore the zero resistance is most likely achieved via a percolation network of thin SC paths. This suggestion is corroborated by the resistive behavior in a magnetic field perpendicular to the conducting ac-plane on entering the CDW pressure regime, $P < 2.5$ kbar.

Fig. 2 presents the temperature dependence of the critical field, determined as shown in the inset of Fig. 2, at pressures around P_c . At zero-field, the critical temperature does not change by more than 10% within this pressure interval. In contrast, the critical field shows a considerable enhancement at lowering the pressure, i.e. at entering the CDW region of the phase diagram. Moreover, the slope of the temperature dependence, linear above P_c , exhibits a clear positive curvature at the lowest pressure. Noteworthy, this behavior does not depend on the point of the resistive transition, in either temperature or field sweeps, that was chosen for the definition of the critical field. Similar results have been obtained on NbSe_3 in the region of coexisting CDW and SC phases [8] and in $(\text{TMTSF})_2\text{PF}_6$, in which SDW and SC phases coexist [9] in a narrow pressure range.

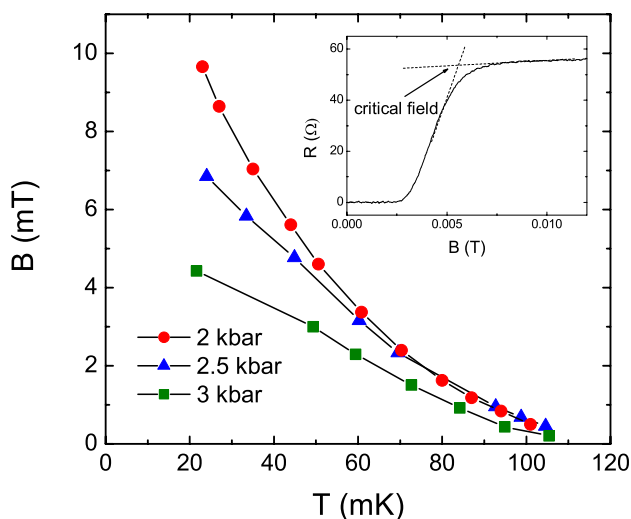


Figure 2: Critical fields at different pressures around P_c . The inset shows the determination of the critical field on a field sweep taken at 2 kbar and 44 mK.

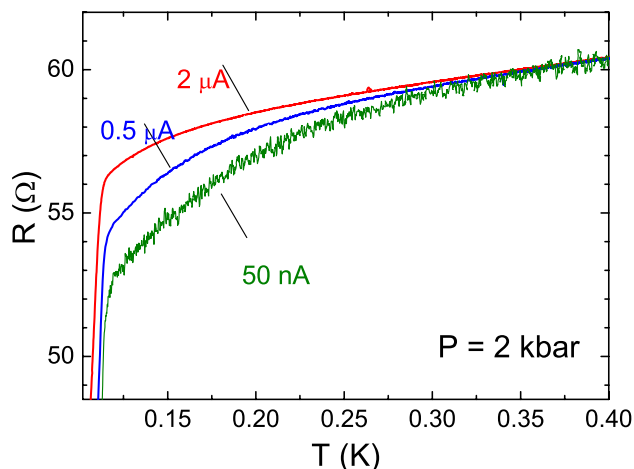


Figure 3: Resistance versus temperature curves at 2 kbar and different values of the measuring current.

the resistance shows a negative curvature up to 300 mK. An example is shown in Fig. 3 for $P = 2$ kbar. This effective decrease of the resistance is found to become suppressed by applying higher currents or a magnetic field of ~ 10 mT. Such a behavior suggests that traces of superconductivity already exist well above the maximum temperature of the bulk transition. The effect is either absent or greatly reduced at pressures above P_c . Further studies are needed to understand this apparent enhancement of superconduc-

These results lead us to the conclusion that below P_c the compound is in an inhomogeneous state in which tiny SC fractions are included in a non-SC (actually CDW) matrix. The exact structure is unknown at present; however, in analogy with NbSe_3 , one could suppose that the SC is realized within boundaries between CDW domains, where the CDW order parameter is suppressed.

The described behavior under hydrostatic pressure can thus be understood by a competition of SC and CDW phases. With lowering the pressure into the CDW state the main SC transition gradually becomes suppressed and the SC inclusions are assumed to become smaller or fewer. However, looking carefully on the temperature sweeps within the CDW state one finds that

tivity at entering the CDW state.

References

- [1] P. Christ, W. Biberacher, M. V. Kartsovnik, E. Steep, E. Balthes, H. Weiss and H. Müller, *JETP Lett.* **71**, 303 (2000).
- [2] R. Kondo, S. Kagoshima and M. Maesato, *Phys. Rev. B* **67**, 134519 (2003).
- [3] M. Maesato, Y. Kaga, R. Kondo and S. Kagoshima, *Phys. Rev. B* **64**, 155104 (2001).
- [4] D. Andres, M. V. Kartsovnik, W. Biberacher, H. Weiss, E. Balthes, H. Müller and N. Kushch, *Phys. Rev. B* **64**, 161104(R) (2001).
- [5] D. Andres, M. V. Kartsovnik, W. Biberacher, K. Neumaier and H. Müller, *J. Phys. IV France* **12**, PR9-87 (2002).
- [6] A. M. Gabovich, A. I. Voitenko and M. Ausloos, *Phys. Rep.* **367**, 583 (2002).
- [7] H. Ito, M. V. Kartsovnik, H. Ishimoto, K. Kono, H. Mori, N. D. Kushch, G. Saito, T. Ishiguro and S. Tanaka, *Synth. Met.* **70**, 899 (1995).
- [8] A. Briggs, P. Monceau, M. Nunez-Regueiro, M. Ribault and J. Richard, *J. Phys.* **42**, 1453 (1981).
- [9] I.J. Lee, P. M. Chaikin and M. J. Naughton, *Phys. Rev. Lett.* **88**, 207002 (2002).

Orbital Quantization in the High Magnetic Field State of a Charge-Density-Wave System

D. Andres, M. V. Kartsovnik, and W. Biberacher^{1,2}

Due to a very high crystal quality and low critical temperature of the charge-density-wave (CDW) transition, $T_c = 8 - 10\text{K}$, the molecular metal α -(BEDT-TTF)₂KHg(SCN)₄, is an ideal material for studying the effect of strong magnetic fields on the CDW.

Generally, two different mechanisms of coupling of a magnetic field to a CDW should be considered. On the one hand, the *Pauli* response of spins of the interacting electrons leads to a gradual suppression of the CDW. The relevant "magnetic field - temperature" ($B - T$) phase diagram is to a large amount similar to that of a clean superconductor or a spin-Peierls system [1]. In particular, it includes the high-field, low-temperature phase CDW_x corresponding, respectively, to the Larkin-Ovchinnikov-Fulde-Ferrel or soliton lattice phases in the latter two cases. It is mainly the Pauli effect which determines the shape of the $B - T$ phase diagram of α -(BEDT-TTF)₂KHg(SCN)₄ at ambient pressure, in a magnetic field perpendicular to the highly conducting *ac* plane [2].

While the Pauli effect is operative in any CDW system, provided the field is strong enough, on the other hand the *orbital* effect becomes important, when the nesting of the Fermi surface (FS) is sufficiently imperfect. In quasi-one-dimensional (q1D) conductors, the imperfectness of nesting can be introduced by a finite second-order interchain transfer integral t'_\perp describing the next-nearest-chain transfer in the plane of conducting layers. If t'_\perp is comparable to the characteristic CDW energy $t'^*_\perp \simeq \Delta_0/2$ (Δ_0 is the CDW gap at $t'_\perp = 0$), the zero-field critical temperature $T_c(0)$ becomes considerably lower than for a perfectly nested FS. However, a magnetic field applied perpendicular to the layers restricts electron orbits to the chain direction, i.e. enhances their one-dimensionality, and restores the density-wave state. In particular, if $t'_\perp \geq t'^*_\perp$, the system is predicted [3] to undergo a cascade of phase transitions to field-induced CDW (FICDW) subphases with quantized values of the nesting vector, in analogy with the field-induced spin-density waves (FISDW). The FISDW effect is well known for q1D organic conductors (TMTSF)₂X and has been a matter of strong interest for more than a decade as a macroscopic quantum phenomenon (see [4] for a review). To obtain the FISDW in (TMTSF)₂X, one has first to suppress the SDW groundstate which is characteristic of these compounds at normal conditions. This is usually achieved by applying a pressure of a few kbar. The pressure leads to an increase of the "antinesting" term t'_\perp and, when $t'_\perp \geq t'^*_\perp$, the zero-field SDW is suppressed and conditions for the FISDW at low temperatures and high magnetic fields are satisfied [4]. In a similar way, the CDW groundstate was shown to be destroyed by pressure in α -(BEDT-TTF)₂KHg(SCN)₄ and first signatures of the FICDW phenomenon were observed [5]. One should, however, keep in mind that in contrast to the case of a SDW system the CDW instability is subject to the additional Pauli effect.

In this work, we propose that the interplay between the *orbital quantization* and *Pauli* effects gives rise to a novel kind of quantum FICDW transitions, which do not require the large t'_\perp and can be realized in α -(BEDT-TTF)₂KHg(SCN)₄ even at ambient pressure.

Figure 1 shows magnetoresistance (a) and magnetic torque (b) measured on α -(BEDT-TTF)₂-KHg(SCN)₄ at ambient pressure and different field orientations. The orientation is defined by a tilt angle θ between the field and the normal to the conducting *ac* plane and azimuthal angle φ between the field projection on the *ac* plane and the *c* axis. All the curves display a series of hysteretic anomalies suggestive of multiple first order phase transitions. Fig. 1b illustrates that the positions of the anomalies are independent of the azimuthal angle φ . On the other hand,

¹In collaboration with P. Grigoriev, L.D. Landau Institute for Theoretical Physics, Chernogolovka, Russia.

²This work is supported by EU through the Infrastructure Cooperative Network and INTAS programmes.

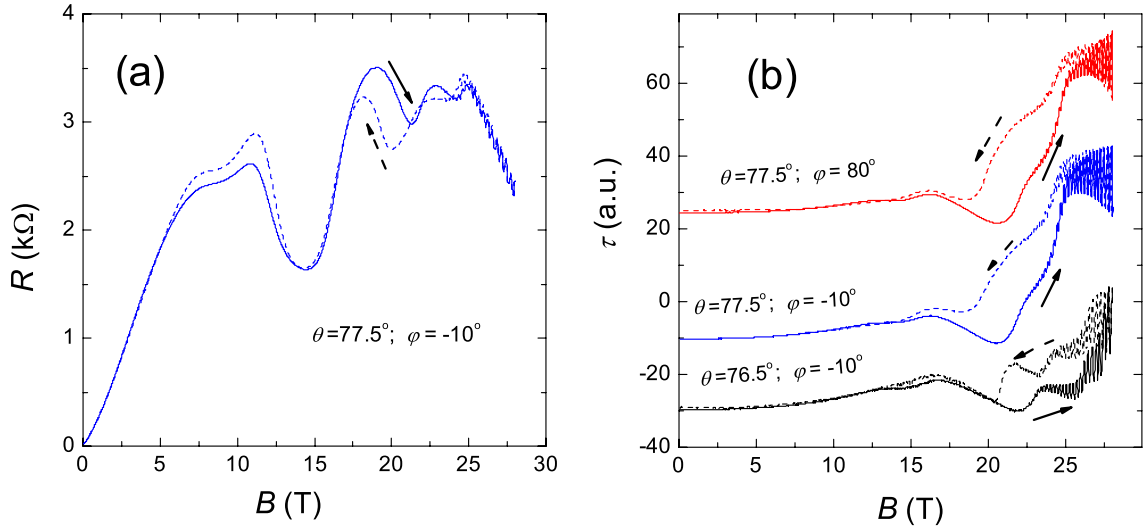


Figure 1: Interlayer resistance (a) and magnetic torque (b) versus magnetic field strongly tilted towards the ac plane. Angles θ and φ define the polar and azimuthal orientation of the field, respectively (see text).

they strongly depend on the tilt angle θ . Fig. 2 shows the positions of local maxima of the torque derivative $(\partial\tau/\partial B)_\theta$ versus angle θ . Crosses correspond to the so-called kink field B_k , which is associated with the transition between the low-field state CDW_0 and high-field state CDW_x [2, 3]. At $\theta \leq 40^\circ$ the kink field is constant, $B_k \approx 23$ T; at higher θ it starts moving to lower fields. The anomalies above B_k emerge at $\theta \geq 65^\circ$ and also rapidly shift down, approaching B_k at $\theta \rightarrow 90^\circ$. The increasingly high sensitivity of the structure to changes in the tilt angle θ near 90° and its independence of the azimuthal orientation φ suggests that the orbital effect determined by the field component $B_z = B \cos \theta$ plays a crucial role. On the other hand, it is important that the anomalies occur at $B > B_k$, i.e. in the fields producing a very strong Pauli effect. Therefore it is very likely that the observed transitions originate from an interplay between the Pauli and orbital effects on the high field CDW state.

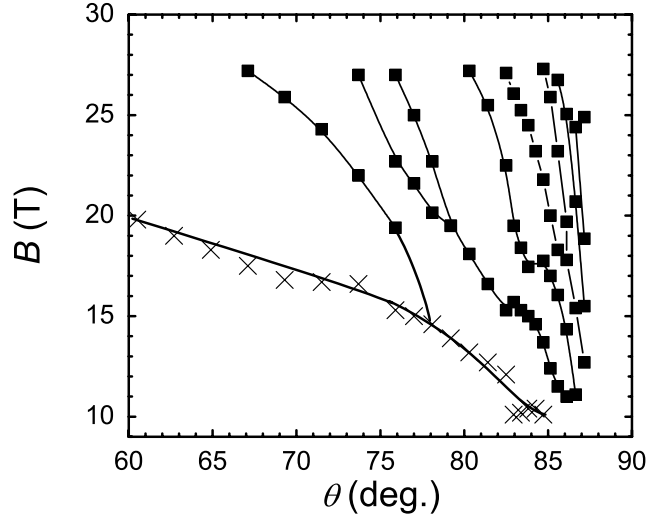


Figure 2: $B - \theta$ phase diagram of α -(BEDT-TTF) $_2$ KHg(SCN) $_4$. Crosses and solid symbols are, respectively, the kink transition and the multiple transitions within the high-field state.

In order to qualitatively understand the origin of the new transitions, we consider the field dependence of the Q_x component of the nesting vector in a CDW system with a moderately imperfect nesting ($0 < t_\perp < t_\perp^*$). At zero field, $Q_{0x} \approx 2k_F$ corresponds to the optimal nesting; the entire FS is gapped. At a finite magnetic field the degeneracy between the CDW's with different spin orientations is lifted. Treating each spin subband independently, one can express the optimal nesting conditions as $Q_{\text{opt},x}(B) = Q_{0x} \pm 2\mu_B B / \hbar v_F$, where μ_B is Bohr magneton, v_F the Fermi velocity in the chain direction and the sign $+(-)$ stands for the spins parallel (antiparallel) to the applied field. This splitting of the optimal nesting conditions is illustrated by dashed lines in Fig. 3. Nevertheless, both subbands remain fully gapped and the system

as a whole maintains the constant nesting vector Q_{0x} up to the critical field $B_k \sim \Delta(B=0)/2\mu_B$. Above B_k , Q_{0x} is no longer a good nesting vector as it leads to ungapped states in both subbands. As shown by Zanchi *et al.* [3], the CDW energy can be minimized in this case by introducing a field dependent term $q_x^{\text{Pauli}} = Q_x(B) - Q_{0x}$ which is schematically represented in Fig. 3 by the thin solid line asymptotically approaching the value $2\mu_B B/\hbar v_F$. This obviously improves the nesting conditions for one of the spin subbands (say, the spin-up subband) at the cost of an additional "unnesting" of the other (spin-down).

Now it is important to take into account that the spin-down subband becomes unnested at $B > B_k$ and, therefore, is subject to a strong orbital effect. The situation is analogous to that with a large antineesting term $t'_\perp \geq t'_\perp^*$. One can therefore expect that, like in the "conventional" FISDW or FICDW case, an orbital quantization condition is imposed on the system. However, unlike in the FISDW case, the quantized levels are counted from $(Q_{0x} - 2\mu_B B/\hbar v_F)$ rather than from Q_{0x} . The corresponding values $q_{xN} = -2\mu_B B/\hbar v_F + NG$ (where $G = ea_y B_z/\hbar c$) are shown by dotted lines in Fig. 3. As a result, the most favorable values of the nesting vector above B_k are determined by intersections of the continuous curve q_x^{Pauli} with the straight lines q_{xN} , i.e. by the superposition of the Pauli and quantum orbital effects. Thus, with changing the field we obtain a series of first order transitions between CDW subphases characterized by different quantized values of the nesting vector as schematically shown by thick lines in Fig. 3. Note that the quantum number N increases with the field, in contrast to what is usually observed in known orbital quantization phenomena.

The multiple FICDW transitions can be observed when the distance G between the quantized levels is smaller than $\mu_B B/\hbar v_F$. This condition is obviously not fulfilled for α -(BEDT-TTF)₂KHg(SCN)₄ at the field perpendicular to the layers. With a finite tilt of the applied magnetic field, G reduces and is determined by $B_z = B \cos \theta$, whereas the Pauli effect remains unchanged. This causes the transitions at low enough $\cos \theta$. With further increasing θ , the transitions shift to lower fields, in agreement with the experiment.

Thus, the presented qualitative model seems to explain the physical origin of the multiple field-induced transitions in α -(BEDT-TTF)₂KHg(SCN)₄ and their evolution with changing the field orientation. The real phase lines shown in Fig. 2 look somewhat more complicated than one would derive from this simple consideration. A more thorough theoretical analysis aiming at a more quantitative description of the new phenomenon is in progress.

References

- [1] A. Buzdin and V. Tugushev, *Sov. Phys. JETP* **58**, 428 (1984).
- [2] P. Christ, W. Biberacher, M. V. Kartsovnik, E. Steep, E. Balthes, H. Weiss, and H. Müller, *JETP Lett.* **71**, 303 (2000).
- [3] D. Zanchi, A. Bjelis, and G. Montambaux, *Phys. Rev. B* **53**, 1240 (1996).
- [4] T. Ishiguro, K. Yamaji, and G. Saito, *Organic Superconductors*, 2nd edition (Springer-Verlag Berlin Heidelberg, 1998).
- [5] D. Andres, M. V. Kartsovnik, W. Biberacher, H. Weiss, E. Balthes, H. Müller, and N.D. Kushch, *Phys. Rev. B* **64**, 161104(R) (2001).

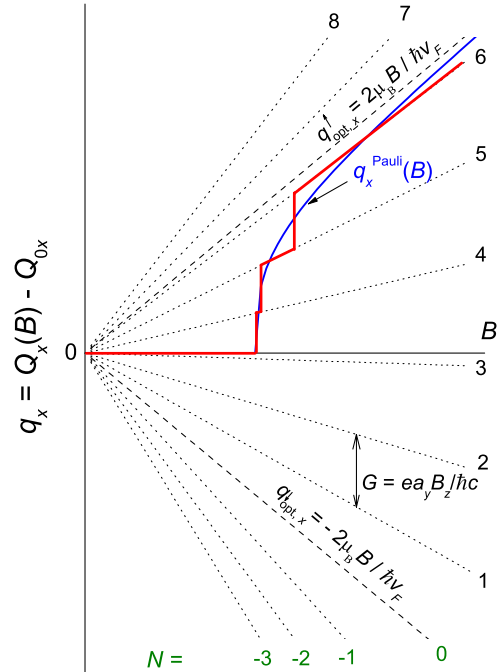


Figure 3: Schematic illustration of the superposition of the Pauli effect and orbital quantization on the CDW wave vector.

Dynamical Properties of Stripes in $\text{La}_{2-x}\text{Sr}_x\text{CuO}_4$

L. Tassini, F. Venturini, Q.-M. Zhang, R. Hackl^{1,2}

The physics of copper-oxide systems is determined by several instabilities such as long-range antiferromagnetism below T_N , charge and spin ordering and superconductivity below T_c (Fig. 1). The strong interactions mediated by critical fluctuations above a potential quantum-critical point (QCP) provide an effective mechanism for the formation of Cooper pairs. [3] This implies that the tendency of the originally two-dimensional charge distribution in the planes to order into one-dimensional structures or “stripes” (Fig. 2) could be a precursor of superconductivity. [4, 5] Therefore, the study of the dynamics of the carrier properties in the relevant range of doping and temperature is one of the key issues in improving the understanding of the cuprates in general and their superconductivity in particular. While the existence of charge and/or spin ordering seems to be proved at least for some of the compounds such as $\text{La}_{2-x-y}(\text{Re})_y\text{Sr}_x\text{CuO}_4$ with $\text{Re} = \text{Eu}, \text{Nd}$ the electrodynamics is still an open issue. In fact, some clues could be found in systems with static stripes, i.e. whenever the charge instability couples strongly to the lattice. However, in most of the compounds, in particular at doping levels in the metallic state the stripes are usually fluctuating and do not lead to anisotropies in the conductivity, for instance. Consequently, one has to look for indirect rather than for direct indications.

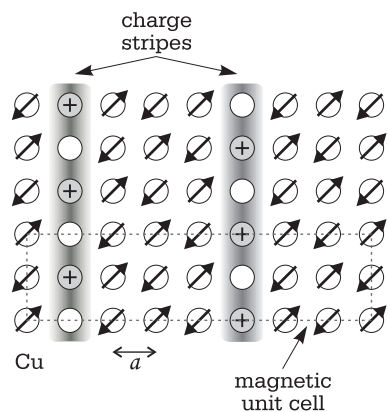


Figure 2: Sketch of charged stripes on an antiferromagnetic background.

Fig. 3).

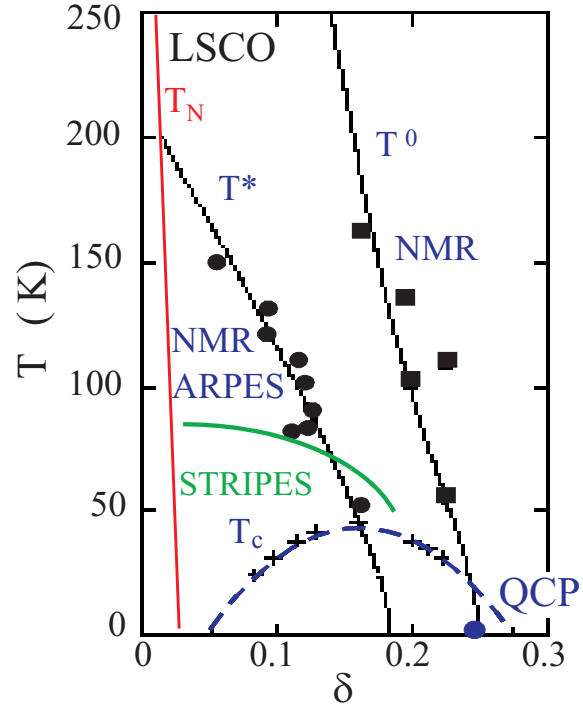


Figure 1: Phase-separation and cross-over lines in $\text{La}_{2-x}\text{Sr}_x\text{CuO}_4$ (LSCO). The experimental points and the theoretical lines for T^* and T^0 are adopted from refs. [1] and [2], respectively. T_N denotes the Néel and T_c the superconducting transition temperature.

The conductivity in the CuO_2 plane is not isotropic even if there are no charge ordering phenomena. This holds true particularly in the underdoped range as has been shown recently by Raman scattering experiments in $\text{Bi}_2\text{Sr}_2\text{CaCu}_2\text{O}_{8+\delta}$ (Bi-2212). [6] There, the conductivity in the vicinity of the M points (anti-nodes) of the Brillouin zone, is strongly suppressed at low doping while it is essentially doping independent in the nodal regions along the diagonals. This type of behavior can clearly be observed only in Bi-2212. In $\text{YBa}_2\text{Cu}_3\text{O}_{6+x}$ (Y-123) the variation with doping is much weaker. In LSCO the anisotropy exists only at high temperature and disappears below 100 K. For $\text{La}_{1.9}\text{Sr}_{0.10}\text{CuO}_4$ a new type of response was observed at low frequencies and temperatures in B_{1g} symmetry [7] which is similar to the spectra found for quasi one-dimensional materials [8] and which over-compensates the expected suppression of spectral weight with decreasing temperature below 200 cm^{-1} (see

¹In collaboration with N. Kikugawa and T. Fujita, University of Hiroshima.

²This work is supported by the DFG and the Alexander von Humboldt Foundation.

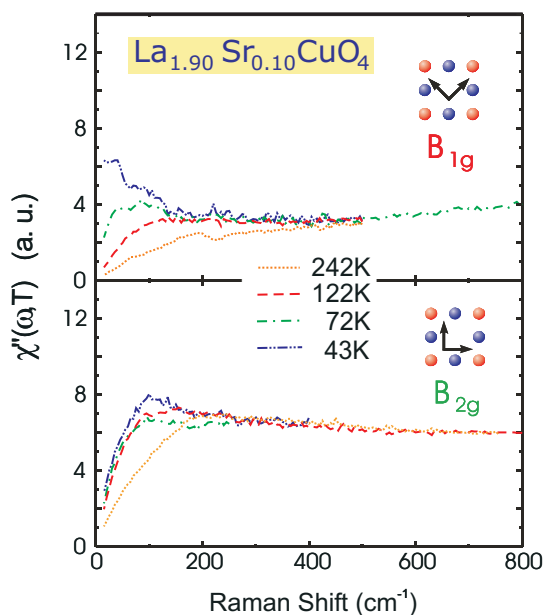


Figure 3: Raman spectra of $\text{La}_{1.90}\text{Sr}_{0.10}\text{CuO}_4$.

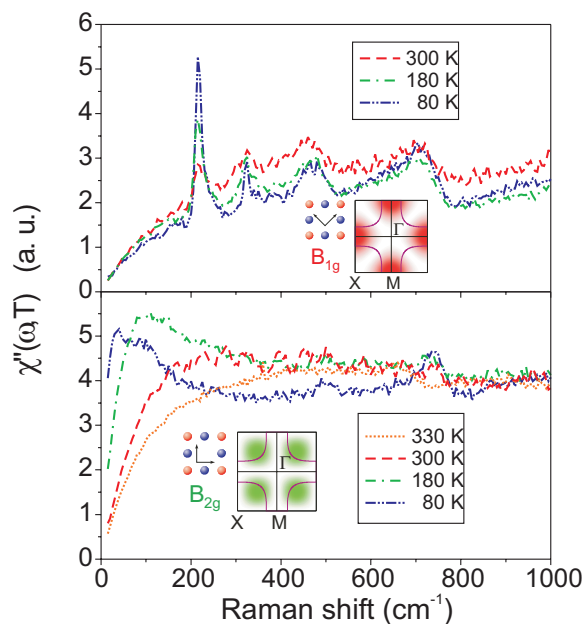


Figure 4: Raman spectra of $\text{La}_{1.98}\text{Sr}_{0.02}\text{CuO}_4$.

In $\text{La}_{1.98}\text{Sr}_{0.02}\text{CuO}_4$ (Fig. 4) no indication of 1D response is found any more in B_{1g} symmetry but rather the temperature resistivity and/or the metal-insulator transition [6]. In B_{2g} symmetry, on the other hand, the slope in the dc limit ($\omega \rightarrow 0$) looks metallic exhibiting a very large $d\Gamma/dT$ with Γ the “Raman” relaxation rate. Comparing the two doping levels $x = 0.1$ and $x = 0.02$ it becomes clear that the 1D response is now superimposed on the B_{2g} spectra.

The symmetry dependence is straightforwardly and completely explained by the orientation of the stripes: whenever one of the photons either incoming or scattered is polarized perpendicular to the direction of the 1D structure the light cannot couple any more to the carriers (see Fig. 5).

of 1D response is found any more in dependence anticipated from the c-axis

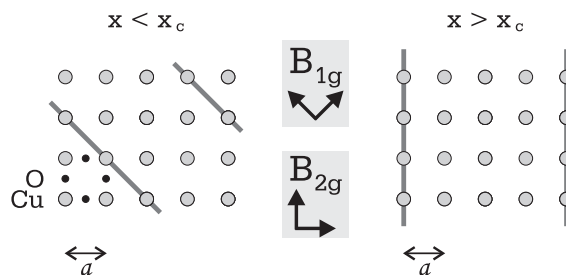


Figure 5: Charge ordering in the CuO_2 plane. There exist two possible orientations of the stripes above and below the critical doping $x_c \simeq 0.55$. Quasi 1D response can therefore be observed in either B_{1g} or B_{2g} symmetry.

References

- [1] M. Gutmann, E.S. Božin, S.J.L. Billinge, cond-mat 0009141 (2000).
- [2] S. Andergassen, S. Caprara, C. Di Castro, and M. Grilli, Phys. Rev. Lett. **87**, 56401 (2001).
- [3] C. Castellani, C. Di Castro, and M. Grilli, Phys. Rev. Lett. **75**, 4650 (1995).
- [4] V. Emery and S. Kivelson, Nature **374**, 434 (1995).
- [5] A. Perali *et al.*, Phys. Rev. B **54**, 16216 (1996).
- [6] F. Venturini *et al.*, Phys. Rev. Lett. **89**, 107003 (2002).
- [7] F. Venturini *et al.*, Phys. Rev. B **66**, 060502(R) (2002).
- [8] G. Blumberg *et al.*, Science **297**, 584 (2002).

Viscous Transport in Dirty Fermi Superfluids

Dietrich Einzel

As is well known, the superfluid phases of liquid ^3He are characterized by *unconventional* pairing correlations, reminiscent of those in the unconventionally paired heavy fermion superconductors, hole doped high- T_c cuprate superconductors, the Ruddlesden–Popper system Sr_2RuO_4 and others. This unconventionality is defined through the vanishing Fermi surface average of the energy gap $\langle \Delta_{\mathbf{p}} \rangle_{\text{FS}} \equiv 0$, and is manifested by the sensitivity of thermodynamic, response and transport properties to the presence of even small concentrations of nonmagnetic impurities. Low density aerogels, dilute correlated aggregates of silica whose constituents' size is of near atomic scale (1.5 nm mean diameter) provide the opportunity to study the effects of disorder on the superfluidity of ^3He , by itself the purest material known at low temperature.

We explore quasiparticle dissipation effects in superfluid ^3He –B in aerogel and provide the first model for the shear viscosity of Bogoliubov quasiparticles (BQP) in superfluid ^3He –B in the presence of impurities. The shear viscosity, together with a Drude contribution govern the attenuation of transverse sound which is closely related to the decrease in dissipation seen in an experiment below T_c [1]. We interpret this decrease as the first experimental evidence for an impurity-limited viscosity aside from metallic superconductivity.

In the presence of both inelastic (η_i) and elastic (η_e) collisions the shear viscosity η of superfluid ^3He –B may be well approximated by the Matthiessen rule expression

$$\frac{1}{\eta} = \frac{1}{\eta_i} + \frac{1}{\eta_e} ; \quad \eta_v = \frac{1}{5} \rho_{n0} \bar{V} 2 \tau_2^v ; \quad v = i, e \quad (1)$$

Here ρ_{n0} is the normal fluid density in the absence of Fermi liquid renormalization, \bar{V} is the thermal average of the BQP group velocity and τ_2^v denotes the relaxation time of the BQP momentum current in the elastic ($v = e$) and the inelastic ($v = i$) scattering channel, respectively. The viscosity η drops sharply below T_c due to the nonanalytic dependence of the BQP group velocity on energy arising from the onset of the energy gap, and assumes a *finite low T limiting value* of approximately $\frac{1}{5}$ of the value at T_c . The results for the impurity limited viscosity η_e depends on the strength of the impurity scattering (Born vs. unitary limit) believed to be relevant for aerogel as the impurity system. In what follows, we adopt arguments in favor of strong impurity scattering close to the unitary limit [2]. If one neglects the pair-breaking impurity band contribution at low T to η , the viscosity η_e assumes the form identical to the case of s -wave pairing, Born scattering:

$$\eta_e(T) = 2\eta_{eN} \left\{ \exp\left(\frac{\Delta(T)}{k_B T}\right) + 1 \right\}^{-1} \quad (2)$$

with η_{eN} the impurity limited viscosity of the normal state and $\Delta(T)$ the energy gap of the BW state. This form implies that η_e drops below T_c , though not as fast as η_i , and *vanishes exponentially* $\propto \exp(-\Delta/k_B T)$ in the low temperature limit.

The viscosity η dominates the attenuation of the transverse sound mode in pure ^3He , which is diffusive in the hydrodynamic limit. Its wavenumber q reduces to the well-known result

$$q = \frac{(1+i)}{\delta} ; \quad \delta = \sqrt{\frac{2\eta}{\rho_n \omega}} \quad (3)$$

with δ the viscous penetration depth. The attenuation

$$\alpha_0(\omega) = \text{Im}q = \frac{1}{\delta(\omega)} \quad (4)$$

varies therefore like $(\rho_n/\eta)^{1/2}$ and is expected to *increase* below T_c .

Ordinarily, liquids cannot support a propagating transverse sound mode. However, the presence of the dilute aerogel, which introduces stiffness to shear, enables the propagation of a transverse sound mode, which, at frequency ω and wavenumber q , is characterized by the dispersion relation

$$\omega^2 = c_{\perp}^2(\omega)q^2 ; c_{\perp}^2(\omega) = c_{\perp 0}^2 \{1 - i\zeta(\omega)\} \quad (5)$$

Here $c_{\perp}(\omega)$ denotes the complex sound velocity with $\zeta(\omega)$ the dissipation. In Eq. (5) we have defined the transverse sound velocity $c_{\perp 0}^2 = \rho_a c_a^2 / (\rho_n + \rho_a)$ with c_a the corresponding transverse sound velocity of the empty aerogel matrix. Clearly $c_{\perp 0}$ vanishes in the limit $\rho_a = 0$. The velocity $c_{\perp 0}$ describes the coupling (mass loading) of the $^3\text{He-B}$ BQP, characterized by their normal fluid density ρ_n to the aerogel system (mass density ρ_a). The attenuation of transverse sound is conveniently expressed as the imaginary part of the complex wave number q

$$\alpha(\omega) = \text{Im}q = \frac{\omega}{2c_{\perp 0}} \zeta(\omega) = \frac{\omega^2}{2c_{\perp 0}^3} \frac{\rho_n}{\rho_n + \rho_a} \left\{ \frac{\eta}{\rho_n} + c_{\perp 0}^2 \tau_1 \right\} \quad (6)$$

In deriving the result (6) we have generalized the collision–drag model of Higashitani *et al.* [3] to the superfluid B–phase. The first term in curly brackets is the viscous diffusivity of the BQP, characterized by the shear viscosity η and contains contributions from both inelastic and elastic collisions whereas the second term is a Drude type diffusivity characterizing elastic collisions with impurity transport time τ of the BQP with the moving impurity matrix. Rewriting the attenuation as

$$\alpha(\omega) = \frac{\omega^2 \eta(T)}{2c_{\perp 0}^3 (\rho_n + \rho_a)} \left\{ 1 + \frac{c_{\perp 0}^2}{\bar{V}^2} \left(\frac{\rho_n}{\rho_{n0}} \right) 2 \frac{\tau_1}{\tau_2} \right\} \quad (7)$$

one observes that the temperature dependence of $\alpha(T)$ is determined essentially by that of the viscosity η with a correction proportional to the inverse BQP group velocity. Applying the parameters relevant to the experimental situation at $P = 20$ bar, it turns out that the shear viscosity η is impurity–limited ($\eta \approx \eta_e$) and gives the dominant contribution to α . Most importantly, the attenuation *drops* below T_c , and develops a shallow plateau at intermediate temperatures originating from the Drude contribution to α . The increase of this Drude term (the second term on the r.h.s. of Eq. (7)) with decreasing temperature has its origin in the temperature dependence of $\lim_{T \rightarrow 0} \bar{V}^2 \propto T/T_c$.

The assumption that the aerogel system supports a transverse sound mode to which the BQP system may be coupled, allows for a qualitative understanding of the experimentally observed decrease of dissipation below T_c in superfluid $^3\text{He-B}$ [1]. The increase of dissipation observed below T_c in $^3\text{He-}^4\text{He}$ mixtures, follows the prediction of Eq. (4) and can therefore possibly be attributed to a reduction of the relative importance of impurity scattering due to the increased specularly at the ^4He covered aerogel.

References

- [1] A. I. Golov, D. Einzel, G. Lawes, K. Matsumoto, and J. M. Parpia, submitted to PRL
- [2] X. Y. Higashitani, *J. Low Temp. Phys.* **114**, 161 (1999)
- [3] X. Y. Higashitani *et al.*, *Phys. Rev. Lett.* **89**, 215301 (2002)

Superconductivity in a Hydrated Layered Cobalt Oxide

Anton Lerf, Werner Biberacher, Robert Schöllhorn

In the spring of this year a transition to the superconducting state has been found for a layered cobalt oxide with the composition $\text{Na}_{0.33}(\text{H}_2\text{O})_y\text{CoO}_2$ [1]. This rather new compound was prepared by oxidizing $\text{Na}_{0.7}\text{CoO}_2$ with bromine in acetonitrile. Treating this sample subsequently with water yields the hydrated sample mentioned above. The authors [1] discuss the similarity with the high- T_c oxide compounds. In our opinion the superconductivity of this sample resembles strongly the situation in the metal intercalation compounds of the layered dichalcogenide 2H-TaS_2 . There, we found a strong influence of water on the superconducting transition temperature [2]. The T_c values of both sodium compounds with the same sodium content $\text{Na}_{0.33}(\text{H}_2\text{O})_y\text{CoO}_2$ and $\text{Na}_{0.33}(\text{H}_2\text{O})_y\text{TaS}_2$ are obviously very similar ($T_c = 5$ K and 5.5 K, respectively) and show a cusp like behaviour of T_c vs. sodium content with a maximum at $x = 0.33$.

Our preliminary trials to reproduce this interesting observation for the cobalt oxide system and to modify T_c by chemical reactions led to the following results: We measured the transition to the superconducting states on powders via an a.c. susceptibility method. The best of our samples gave a $T_{c\text{-onset}}$ of about 4 K. This is in good agreement with the results of Rivadulla *et al.* [3] and Schaak *et al.* [4]. A $\text{Na}_{0.7}\text{CoO}_2$ sample annealed in pure oxygen according to Takada *et al.* [1] was not completely oxidized however within seven days. The very low T_c and the low signal intensity with respect to the amount of material used in the measurement may be caused by this incomplete oxidation. After hydration of the oxidized samples for one day we found a pH value of 11-12 in the supernatant water. Storing the samples under water may be detrimental for the superconducting state. Treating the sample after the T_c -measurement with a slightly acidic solution destroys superconductivity immediately. It does not recover by treating this sample with neutral Na_2SO_4 -solution. By means of x-ray diffraction no significant changes have been observed. In agreement with Takada *et al.* [1] superconductivity disappears also after drying the hydrated compound in air. Adding a potassium solution to the hydrated sodium compound, there is an ion exchange with reduction of the layer distance. This sample is also not superconducting. If the hydrated compound is treated with dodecylpyridinium ions, this ion is not intercalated instead of sodium but the layer distance collapses to a value typical for the non-superconducting CoOOH . Although the oxidation of the ternary sodium cobalt oxide leads to the formation of a hydrated intercalation compound, its behaviour is in some respect rather different from the behavior of the corresponding tantalum disulfide compound. In the latter case we can stabilize intermediate hydration states with remarkably different T_c -values, and loading of the sodium compound with other di- and trivalent ions via ion exchange leads to different superconductors with some variation in T_c [2]. In contrast, the cobalt compound reacts on rather small modifications (degree of hydration, oxidation level, pH) with a complete breakdown of superconductivity.

Single crystals of Na_xCoO_2 and K_xCoO_2 have been prepared successfully from basic melts. They can be transformed by chemical and anodic oxidation to the corresponding hydrated phases. Galvanostatic curves exhibit a small potential window between oxidized and reduced states and a complex reaction pattern with several intermediate states. No superconducting transitions could be detected. This most likely is caused by Al^{3+} defects on Co^{3+} sites introduced via the aluminum oxide reaction vessels.

References

- [1] K. Takada, H. Sakurai, E. Takayama-Muromachi, F. Izumi, R.A. Dilanian, and T. Sasaki, *Nature* **422**, 53 (2003)
- [2] W. Biberacher, A. Lerf, J.O. Besenhard, H. Möhwald, T. Butz, and S. Saibene, *Il Nuovo Cim.* **2D**, 1706 (1983).
- [3] F. Rivadulla, J.-S. Zhou, and J.B. Goodenough, submitted for publication.
- [4] R.E. Schaak, T. Klimczuk, M.L. Foo, and R.J. Cava, *Nature* **424**, 527 (2003).

Magnetic Interactions in the Double Perovskites

Jan B. Philipp, Petra Majewski, Daniel Reisinger, Stephan Geprägs, Matthias Opel, Andreas Erb, and Rudolf Gross^{1,2}

Double perovskites of composition $A_2BB'O_6$ with A an alkaline earth such as Sr, Ba, or Ca and B, B' a magnetic and non-magnetic transition metal or lanthanide ion, respectively, are known since many decades [1, 2, 3, 4, 5]. However, only recently the study of ordered double perovskite materials has been strongly intensified both by their interesting magnetic properties ranging from antiferromagnetism to geometrically frustrated spin systems and ferromagnetism and, more importantly, the discovery of a large room temperature magnetoresistive effect at low magnetic fields in the system Sr_2FeMoO_6 [6]. With respect to applications, the fact that some magnetic double perovskites seem to be ferromagnetic metals with high Curie temperatures T_C of up to 635 K [7] and apparently have a highly spin polarized conduction band makes these materials interesting for spintronic devices such as magnetic tunnel junctions, low-field magnetoresistive sensors or spin injection devices [8]. Up to now large low-field magnetoresistive effects have been found not only in Sr_2FeMoO_6 [6, 9, 10], but also in many other double perovskites as for example Sr_2FeReO_6 [11], Sr_2CrReO_6 [7], Sr_2CrWO_6 [12, 13, 14], and $(Ba_{0.8}Sr_{0.2})_{2-x}La_xFeMoO_6$ [15]. With respect to fundamental aspects, the main research effort is focused on the understanding of the magnetic interactions in the various types of magnetic double perovskites and their relation to structural, electronic as well as magnetotransport properties.

The rich physics of the double perovskites $A_2BB'O_6$ is related to the fact that they are very flexible with respect to variations of the magnetic and/or non-magnetic BB' ions as well as the A -site cations. In this way they offer a wide range of possibilities to influence the structure and/or the magnetic interactions and, hence, to tailor the magnetic properties for specific applications or fundamental studies:

1. The magnetic ion on the B -site can be varied using either $3d$ or $4d$ transition metals (e.g. Fe, Cr, Mn, Ni, Co, Ru) with localized states or $4f$ lanthanides (e.g. Gd, Dy, Ho, Er) with highly localized states.
2. The non-magnetic ion on the B' -site can be varied. Here, we have to distinguish between ions with delocalized electrons (e.g. Mo^{5+} , W^{5+} , Re^{5+} , Re^{6+}) and those with a noble gas electronic configuration (e.g. Nb^{5+} , W^{6+}) or a completely filled $3d$ - or $4d$ -shell (e.g. Sb^{5+} , Te^{6+}).
3. We can dope electrons into the system by partially replacing the divalent alkaline earth ions on the A -site by a trivalent rare earth ion such as La^{3+} [14, 16, 15].
4. The crystal structure can be changed by using alkaline earth ions on the A -site with different ionic radii. This results in considerable steric effects (see Fig. 1b), which in turn change the bond angles thereby modifying the magnetic interactions.
5. We can also use magnetic ions on both the B - and B' -site as e.g. in $LaAVRuO_6$ and $LaAVMn_6$ with $A = Ca, Sr, Ba$, or La_2CrFeO_6 [17, 18]. This class of double perovskites, which we do not discuss here, may be interesting for the realization of half-metallic antiferromagnets [19].

Here, we discuss the magnetic interactions in the double perovskites with B a magnetic and B' a non-magnetic ion, which are still discussed controversially. We summarize the present knowledge based on our own experimental results and the data available in literature. Experimental results already have been reported in the last year's report and can be found in Refs. [12, 13, 14, 53, 54].

¹In collaboration with M.S. Brandt and T. Graf (Walter Schottky Institute), J. Simon, T. Walther, and W. Mader (University of Bonn), M. S. Ramachandra Rao (IIT Madras, India), as well as D. Topwal and D.D. Sarma (Indian Institute of Science, Bangalore, India).

²This work is supported in part by the Deutsche Forschungsgemeinschaft and the BMBF (13N8279).

Magnetic Interactions in the Double Perovskites

The perovskites of composition ABO_3 are ubiquitous in oxide chemistry. The perovskite structure in the simplest case consists of a 3D lattice of fully corner sharing BO_6 octahedra forming a cavity, in which the larger atom A is 12-fold coordinated to oxygen. Many variants are known. The double perovskites of composition $A_2BB'O_6$ have chemical supercells, in which two kinds of ions are found at the B -site in alternating octahedra (see Fig. 1a).

A particularly interesting configuration, which we will discuss in the following, is the case of an ordered double perovskite, in which only the ion on the B -site carries

a magnetic moment. In this case the ordered sublattices of the B and B' ions form two interpenetrating fcc networks. In reality, of course, there is always a certain amount of B/B' cationic disorder (antisite defects), which may considerably affect the magnetic properties.

The magnetic interactions in the double perovskites with the B - and B' -site ions being magnetic and non-magnetic ions, respectively, are very interesting and complex. They strongly depend on the details of the crystal structure, the amount of B/B' antisites, and the magnetic and electronic properties of the B and B' ions. In the following we discuss the various types of magnetic interactions dominating in different systems and classify the double perovskite materials into different categories accordingly. With respect to the magnetic ion on the B -site, we will distinguish the following two cases:

- the magnetic ion is a magnetic lanthanide ion with highly localized $4f$ states such as Gd^{3+} , Dy^{3+} , Ho^{3+} , or Er^{3+} . There is negligible hopping of the $4f$ electrons preventing a hopping based magnetic interaction mechanism.
- the magnetic ion is a transition metal ion with less localized $3d$ or $4d$ states such as Fe^{2+} , Fe^{3+} , Cr^{3+} , Ni^{2+} , Co^{2+} , Mn^{2+} , V^{3+} or Ru^{4+} . There is sizable hopping resulting in a hopping based magnetic interaction mechanism, which depends on the electronic structure of the non-magnetic B' -site ion.

With respect to the non-magnetic ion on the B' -site, we will distinguish the following two cases:

- The non-magnetic B' -ion has a partially filled outer shell with one or two delocalized electrons (e.g. Mo^{5+} , W^{5+} , Re^{5+} , Re^{6+}). Typical examples are Sr_2FeMoO_6 [6, 9, 10, 20], Sr_2CrReO_6 [7], Sr_2CrWO_6 [12, 13, 14] as well as Sr_2FeReO_6 [11, 21] or Ca_2FeReO_6 [21, 22, 23].
- the non-magnetic B' -ion has a noble gas electronic configuration (e.g. Nb^{5+} , Ca^{2+} , W^{6+}) or a completely filled $3d$ - or $4d$ -shell (e.g. Sb^{5+} , Te^{6+}). Typical examples are Sr_2FeNbO_6 [24, 25, 26], Sr_2FeWO_6 [5, 27, 28, 29], Ca_2NiWO_6 and Ca_2CoWO_6 [30], A_2MnWO_6 with $A = Ca, Sr, Ba$ [31, 32, 33], Sr_2ReCaO_6 [34], Sr_2NiTeO_6 [35], or Sr_2LnSbO_6 with $Ln = Dy, Ho, Gd$ [36].

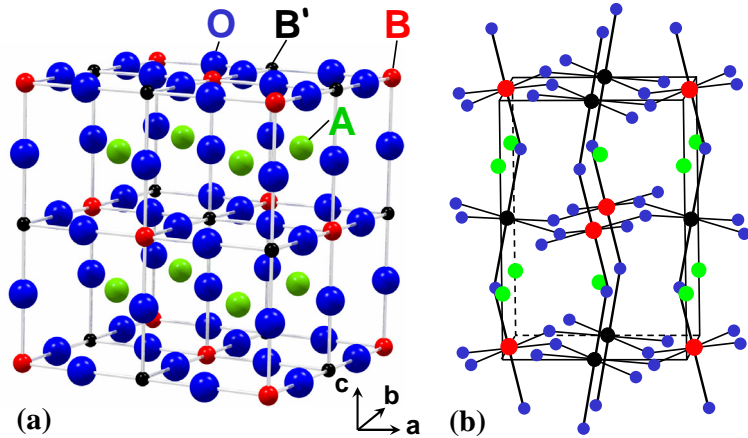


Figure 1: Sketch of the crystal structure of a cubic double perovskite (a) with tolerance factor close to unity. In (b) a distorted structure is shown. For a tolerance factor significantly deviating from unity the tilt and rotation of the BO_6 octahedra result in a non-cubic crystal structure and $B-O-B'$ bonding angles deviating from 180° . The B and B' ions are assumed to be perfectly ordered.

Double perovskites with $B =$ magnetic lanthanide ion

In double perovskite systems $A_2BB'O_6$ with B a magnetic lanthanide ion with highly localized $4f$ states, any magnetic exchange based on the hopping of electrons such as antiferromagnetic superexchange of ferromagnetic double exchange cannot operate, since the probability for an electron to hop from a $4f$ state at one site to another at a neighboring site is too small. This is independent on the type of ion on the B' -site. However, in this situation there may be a weak near-neighbor indirect exchange via the conduction electrons (RKKY-type interaction) or dipolar interactions. In this case the magnetic properties of the system may be very interesting due to frustration effects. For example, interpenetrating fcc networks fall into the class of geometrically frustrated spin systems, since an fcc lattice is comprised of a network of edge-shared tetrahedra (see Fig. 2). If we assume that there is only a simple antiferromagnetic near-neighbor coupling among the magnetic B -ions, the magnetic sublattice consisting of edge-shared tetrahedra (see Fig. 2) is known to result in geometric magnetic frustration. Magnetic materials in which long-range magnetic ordering is frustrated by the geometry of the crystalline lattice have attracted much attention recently, since the geometrical magnetic frustration results in the existence of many energetically equivalent magnetic ground states [37, 38, 39]. So far, magnetic frustration has been studied in 2D Kagomé lattice

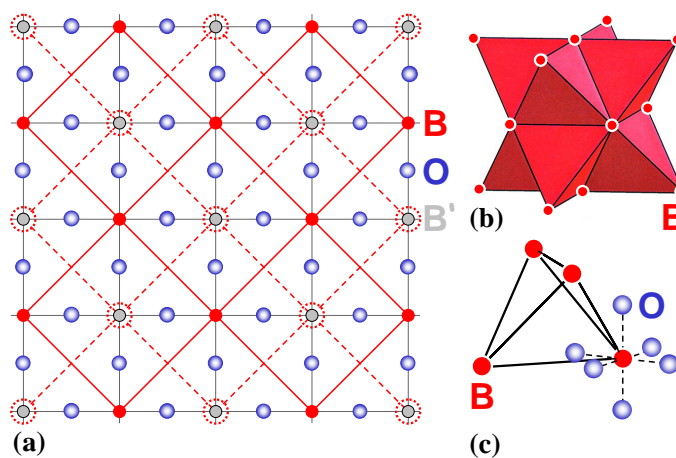


Figure 2: The atom positions and magnetic sublattice in double perovskites with $B =$ magnetic lanthanide ion. In (a) the positions of the magnetic B -site ions in the second plane or marked by dotted circles. The thick lines indicate the near neighbor magnetic interactions within the planes. In (b) the 3D arrangement of the edge-shared magnetic ion tetrahedra is shown. (c) shows the B -O coordination polyhedra.

systems consisting of corner-shared triangles of magnetic ions. The 3D extension is a *corner sharing* tetrahedron lattice is realized in the magnetic lanthanide pyrochlores [40, 41]. Perfectly ordered double perovskites have magnetic sublattices consisting of *edge-sharing* tetrahedra and represent another frustrating geometry in three dimensions. So far, reports on the magnetic properties of these highly interesting magnetic systems are rare [36].

Double perovskites with $B =$ magnetic transition metal ion

In double perovskite systems $A_2BB'O_6$ with B a magnetic transition metal ion with less localized $3d$ or $4d$ states, the magnetic exchange is dominated by hopping of electrons between the different sites. These processes can result both in ferromagnetic or antiferromagnetic coupling. Antiferromagnetic superexchange via the B -O- B' -O- B exchange path is usually dominant for B' ions with noble gas configuration such as Nb^{5+} or W^{6+} . Ferromagnetic exchange mechanisms (double exchange type [42, 43, 44] or hybridization type mechanism [45, 46, 47]) are dominant for B ions with delocalized $4d$ or $5d$ electrons such as Mo^{5+} , W^{5+} , Re^{5+} or Re^{6+} . The hybridization between the delocalized B and the localized B' states usually results in a kinetic energy driven mechanism causing a strong ferromagnetic exchange between the B -sites.

Antiferromagnetic superexchange: The situation for the antiferromagnetic superexchange via the B -O- B' -O- B exchange path is sketched in Fig. 3. This exchange mechanism is dominant for B ions with noble gas configuration such as Nb^{5+} or W^{6+} , i.e. a completely empty $4d$ - or $5d$ -band. Using the simple rule that there is an antiferromagnetic exchange between two empty orbitals (e.g between empty $Fe\ 3d\ \downarrow/Fe\ 3d\ \uparrow$ and the $Nb\ 4d$ orbitals as sketched in Fig. 3), we obtain an anti-

ferromagnetic coupling between the B -sites. In a band-like picture, both the Fe $t_{2g} \downarrow$ and the Nb t_{2g} states are empty. In general, for the double perovskites the antiferromagnetic superexchange is

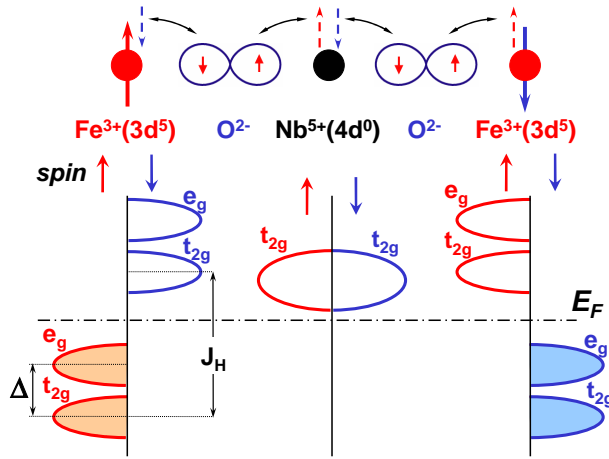


Figure 3: Superexchange mechanism via the B - O - B' - O - B exchange path in double perovskites, where the B' has a completely empty d -shell. The superexchange causes an antiferromagnetic configuration between the localized Fe $3d \uparrow$ spins. The thick arrow mark the Fe $3d^5$ core spins, the broken arrows indicate the spin configuration of an excited state. The lower part shows the situation in a band-like picture for the two spin directions. Here, Δ denotes the crystal field splitting between the t_{2g} and the e_g band, J_H the exchange splitting. The Nb e_g band is well above the t_{2g} band and not shown.

weak due to the long exchange path and therefore results in low Néel temperatures T_N of the order of a few 10 K. Typical examples are $\text{Sr}_2\text{FeNbO}_6$ with a Néel temperature of about 25 K [24, 25, 26] Ca_2CoWO_6 and Ca_2NiWO_6 with $T_N = 26$ and 56 K, respectively [30], as well as Sr_2FeWO_6 with $T_N = 37$ K [27, 28, 29]. We also note that the exchange strength depends on the bonding angles along the exchange path and usually is maximum for a 180° superexchange. Furthermore, disorder on the BB' sublattices can result in spin glass like behavior. On electron doping the system by replacing e.g. Sr^{2+} by La^{3+} in $\text{Sr}_2\text{FeNbO}_6$ shifts the Fermi level into the Nb $4d t_{2g}$ band. In this way mobile electrons are available on the B' -site favoring a ferromagnetic interaction as discussed below. At low doping, a competition between antiferromagnetic super- and ferromagnetic dou-

ble exchange occurs what may result in a spin glass state.

Ferromagnetic double exchange: One of the puzzling features of magnetic double perovskites is the strong ferromagnetic exchange with Curie temperatures up to 635 K [7] in systems, where we have non-magnetic B' ions with delocalized electrons. The origin of ferromagnetism in these double perovskite is still discussed controversially. Recently Moritomo *et al.* found a strong correlation between the room temperature conductivity and the Curie temperature in $\text{Sr}_2\text{FeMoO}_6$, implying that the mobile conduction electrons mediate the exchange interaction between the local Fe^{3+} spins [42, 43]. Therefore, in analogy to the doped manganites it was tempting to explain the ferromagnetic coupling between the Fe sites based on a double exchange mechanism, where the delocalized t_{2g} electron provided by the Mo $4d^1$ configuration plays the role of the delocalized Mn $3d e_g$ electron in the manganites. The situation for the double exchange type exchange mechanism is sketched in Fig. 4 using the example of $\text{Sr}_2\text{FeMoO}_6$. If the Fe $t_{2g} \downarrow$ and the Mo $t_{2g} \downarrow$ bands are almost

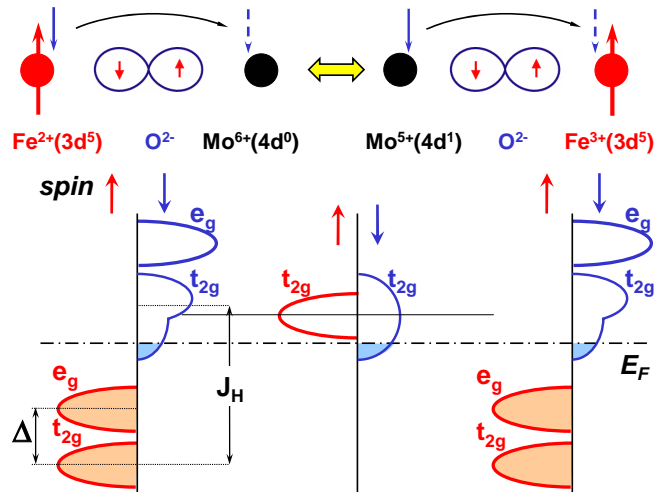


Figure 4: Double exchange type exchange mechanism in double perovskites, where the B' has a partly filled d -shell. The two configurations shown in the top part are degenerate. The thick arrow mark the localized Fe $3d^5$ core spins, the thin arrow the spin of the itinerant electron. The bottom part show the band picture. The Fe $t_{2g} \downarrow$ and the Mo $t_{2g} \downarrow$ bands are almost degenerate resulting in degenerate valence states $\text{Fe}^{3+}\text{-Mo}^{5+}$ and $\text{Fe}^{2+}\text{-Mo}^{6+}$. The hopping of the $3d t_{2g} \downarrow$ electrons results in a broadening of the Mo $4d t_{2g} \downarrow$ and Fe $3d t_{2g} \downarrow$ bands.

degenerate, a competition between antiferromagnetic super- and ferromagnetic dou-

degenerate (this is equivalent to degenerate valence states $\text{Fe}^{3+}\text{-Mo}^{5+}$ and $\text{Fe}^{2+}\text{-Mo}^{6+}$ (see top part of Fig. 4), the t_{2g} electron can easily hop between these states producing a double exchange type interaction [48, 49]. That is, hopping of itinerant spin-down electrons between the Fe and Mo sites yields a kinetic energy gain. Since the Fe $3d \uparrow$ band is completely filled, this hopping of the t_{2g} electrons is only possible, if the Fe core spins are all oriented antiparallel to the spins of the itinerant electrons. As a consequence, a ferromagnetic state with all Fe spin parallel will be energetically favored. The Mo $4d t_{2g} \uparrow$ electrons cannot hop in this situation. Therefore, only the Mo $4d t_{2g} \downarrow$ is broadened resulting in a half-metallic behavior (see bottom part of Fig. 4).

We note that the situation in the double perovskites is different to the double exchange in CMR manganites, where the itinerant $e_g \uparrow$ spins are parallel to the localized $t_{2g} \uparrow$ core spins. In the double perovskites the completely full Fe $3d \uparrow$ band makes it impossible for another spin-up electron to hop between Fe sites and thus forcing the delocalized electrons to be spin-down electrons. Moreover, in the manganites both the localized Mn t_{2g} electrons and the delocalized Mn e_g electron reside at the same site and their spins are coupled ferromagnetically by a strong on-site Hund's coupling J_H . In the double perovskites, the localized Fe $3d$ electrons ($\text{Fe}^{3+}: 3d^5, S = 5/2$) and the delocalized Mo $4d$ electron ($\text{Mo}^{5+}: 4d^1, S = 1/2$) nominally are at two different sites although the Mo $4d$ electron obtains a finite Fe character by sizable hopping interaction. Therefore, at first glance the double exchange scenario is different in the manganites and the double perovskites.

If the B -site $t_{2g} \downarrow$ and the B' -site $t_{2g} \downarrow$ bands are not degenerate, as it is the case for the system $\text{Sr}_2\text{MnMoO}_6$ [50, 51], the hopping is very weak and, hence, a much weaker ferromagnetic interaction is expected within a double exchange type model.

Kinetic energy driven ferromagnetic exchange:

Sarma [9, 45] has proposed another mechanism to explain ferromagnetism in the double perovskites, which has been extended to many other systems by Fang, Kanamori and Terakura [46, 47]. In the Sarma-Fang-Kanamori-Terakura (SFKT) model, the hybridization of the Mo $4d (t_{2g})$ and Fe $3d (t_{2g})$ states plays the key role in stabilizing ferromagnetism at high Curie temperatures [45, 46, 47]. The essence of this model is summarized in Fig. 5 for the case of $\text{Sr}_2\text{FeMoO}_6$. Without any hopping interactions, the $\text{Fe}^{3+} 3d^5$ configuration has a large exchange splitting of the $3d$ levels in the spin-up and spin-down states and there is also a crystal field splitting Δ into the t_{2g} and the e_g states. The exchange splitting of the $\text{Mo}^{5+} 4d^1$ configuration (better the Mo- $4d$ - O - $2p$ hybridized states) is vanishingly small, however, there is a large crystal field

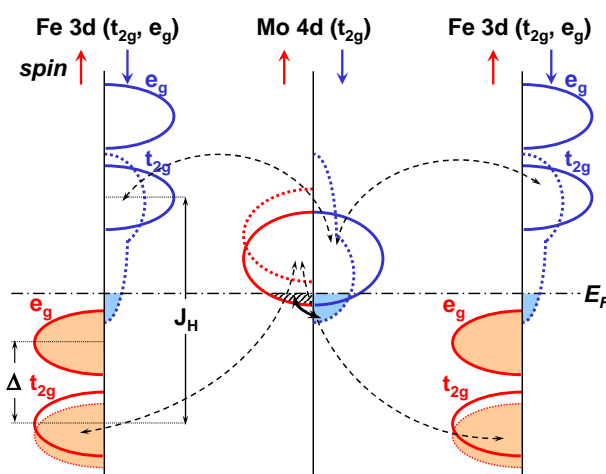


Figure 5: Sketch of the band structure for the illustration of the mechanism stabilizing the ferromagnetic state in the double perovskites using A_2FeMoO_6 as an example. The Fermi energy lies between the exchange split $3d$ spin-up and -down states. The solid lines mark the bands without hybridization, whereas the broken lines mark the bands with hybridization. The broken arrows connect the hybridizing bands. The hybridization between the e_g level has been neglected. The Mo $4d e_g$ band is not shown.

splitting (the e_g states are several eV above the t_{2g} states and not shown in Fig. 5). Switching on the hopping interactions results in a finite coupling between states of the same symmetry and spin. The hopping interaction not only leads to an admixture of the Fe $3d$ to the Mo $4d$ states, but more importantly to a shift of the bare energy levels. As shown in Fig. 5, the delocalized Mo t_{2g} spin-up states are pushed up, whereas the Mo t_{2g} spin-down states are pushed down (bonding-antibonding splitting). This causes a finite spin polarization at the Fermi level (actually 100% in Fig. 5) resulting from the hopping interac-

tions. It is evident that this mechanism leads to an antiferromagnetic coupling between the delocalized Mo $4d$ and the localized Fe $3d$ electrons, since the energy is lowered by populating the Mo $4d$ spin-down band [45]. The magnitude of the spin polarization derived from this mechanism obviously is governed by the hopping strength and the charge transfer energy between the localized and the delocalized states [46]. Furthermore, the itinerant electrons in the Mo $t_{2g} \downarrow$ band cause kinetic energy gain via a double exchange type interaction, which further stabilizes ferromagnetism as discussed above. In view of kinetic energy gain the SFKT model is similar to the double exchange model discussed above.

The essential point in the SFKT scenario is that the hybridized states are located energetically between the exchange-split Fe $3d_{\uparrow}$ and the Fe $3d_{\downarrow}$ levels. Only in this case a bonding-antibonding splitting is obtained. We also note that in the SFKT model the magnetic moment at the Mo site is merely induced by the Fe magnetic moments through the hybridization between the Fe $3d$ and the Mo $4d$ states what can be viewed as a magnetic proximity effect. In this sense the double perovskites should be denoted ferromagnetic and not ferrimagnetic. Recently, it has been shown that the magnetism in Sr_2FeMoO_6 can be well described by two interacting sublattices: the localized $Fe^{3+} 3d^5$ core and the delocalized $Mo^{5+} 4d^1$ delocalized electron spins with a strong antiferromagnetic interaction between the two sublattices in good agreement with the SFKT model [52].

We have pointed out recently [14] that the mechanism discussed above also works for the A_2CrWO_6 system, where only the Cr $3dt_{2g} \uparrow$ band is full, however, the Cr $3de_g \uparrow$ band completely empty. The key concept of the model again is the energy gain contributed by the spin polarization of the non-magnetic element (now W) induced by the hybridization with the magnetic transition metal (now Cr). It has been pointed out by Sarma [9, 45] that the underlying mechanism will always be operative, whenever the conduction band is placed within the energy gap formed by the large exchange splitting of the localized electrons at the transition metal site. As shown in Fig. 6, this is also the case for the A_2CrWO_6 compounds: the W $5dt_{2g}$ band resides in between the exchange split Cr $3dt_{2g}$ spin-up and spin-down bands. The schematic band structure of Fig. 6 has been confirmed by band structure calculations [14]. The only difference between the system A_2CrWO_6

and the systems A_2FeMoO_6 (or also A_2FeReO_6) is the fact that in the former the majority spin band is only partly full. Furthermore, band structure calculations show that the crystal field splitting in the Cr compounds (~ 2 eV) is slightly larger than in the Fe compounds. On the other hand, the exchange splitting in the Cr $3d$ bands is somewhat smaller than for the Fe $3d$ bands due to the valence configuration Cr $3d^3$ with less electrons and weaker Hund's coupling. Taking these facts into account we have to split up the Cr $3d$ spin-up and spin-down band into two separate $3dt_{2g}$ and $3de_g$ bands with the Fermi level lying in the gap between the bands as shown in Fig. 6. Indeed band structure calculations [14] show that the Cr $3de_g$ spin-up band is about 0.5 eV above the Fermi level. However, the above mechanism still works as long as the W $5dt_{2g}$ band is placed within the energy gap between the Cr $3dt_{2g}$ spin-up and the Cr $3dt_{2g}$ spin-down band. Then, again the W $5dt_{2g}$ levels hybridize with the Cr $3dt_{2g}$ levels

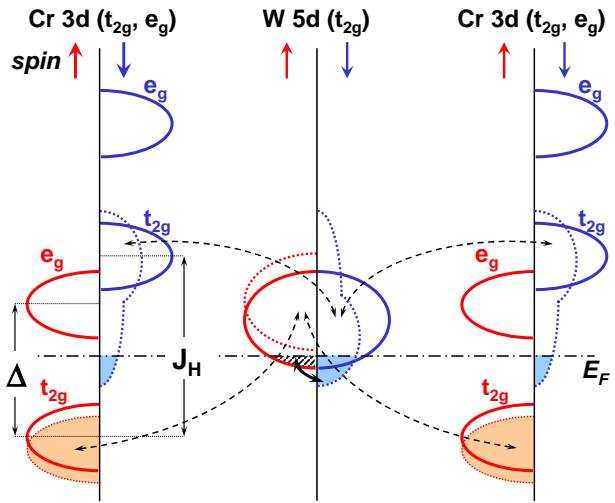


Figure 6: Sketch of the band structure for the illustration of the mechanism stabilizing the ferromagnetic state in the double perovskites using A_2CrWO_6 as an example. In contrast to the A_2FeMoO_6 system the Fermi energy lies between the crystal field split $3d t_{2g} \uparrow$ and $3d e_g \uparrow$ states. The solid lines mark the bands without hybridization, whereas the broken lines mark the bands with hybridization. The broken arrows connect the hybridizing bands. The hybridization between the e_g level has been neglected. The W $5d e_g$ band is not shown.

resulting in a negative spin polarization of the non-magnetic element W $5d_{t_g}$ and a stabilization of ferromagnetism and half-metallic behavior. We note that no hybridization takes place between the Cr $3d_{e_g}$ spin-up band and the W $5d_{t_g}$ spin-up band due to the different symmetry of these levels. Therefore, the exact position of the Cr $3d_{e_g}$ spin-up band is not relevant. Summarizing our discussion we can state that within the SFKT model the essential physical mechanism leading to ferromagnetism is very similar for the A_2CrWO_6 and the A_2FeMoO_6 compounds.

In our experimental work we have studied the structural, magnetotransport, magnetic and optical properties of the ferromagnetic double perovskites (see Refs. [12, 13, 14, 53, 54]). In particular, we studied the impact of steric effects resulting in a distorted perovskite structure, doping effects obtained by a partial replacing of the divalent alkaline earth ions on the A site by a trivalent lanthanide as well as B/B' cationic disorder on the Curie temperature T_C , the saturation magnetization and the magnetotransport properties. Our results support the presence of a kinetic energy driven mechanism in the ferromagnetic double perovskites, where ferromagnetism is stabilized by a hybridization of states of the nonmagnetic B' -site positioned in between the high spin B -sites.

References

- [1] F. Galasso, F. C. Douglas, R. Kasper, *J. Chem. Phys.* **44**, 1672 (1966); see also *Structure, Properties and Preparation of Perovskite-type Compounds*, Pergamon, London (1969).
- [2] F. K. Patterson, C. W. Moeller, R. Ward, *Inorg. Chem.* **2**, 196 (1963).
- [3] J. Longo, R. Ward, *J. Am. Chem. Soc.* **83**, 2816 (1961).
- [4] G. Blasse, *J. Inorg. Nucl. Chem.* **27**, 993 (1965).
- [5] T. Nakagawa, K. Yoshikawa, S. Nomura, *J. Phys. Soc. Jpn.* **27**, 880 (1969).
- [6] K.-I. Kobayashi, T. Kimura, H. Sawada, K. Terakura, and Y. Tokura, *Nature* **395**, 677 (1998).
- [7] H. Kato, T. Okuda, Y. Okimoto, Y. Tomioka, Y. Takenoya, A. Ohkubo, M. Kawasaki, and Y. Tokura, *Appl. Phys. Lett.* **81**, 328 (2002).
- [8] S. A. Wolf, D. D. Awschalom, R. A. Buhrman, J. M. Daughton, S. von Molnar, M. L. Roukes, A. Y. Chtchelkanova, D. M. Treger, *Science* **294**, 1488 (2001).
- [9] D. D. Sarma, E. V. Sampathkumaran, Sugata Ray, R. Nagarajan, S. Majumdar, A. Kumar, G. Nalini, and T. N. Guru Row, *Sol. State Comm.* **114**, 465 (2000).
- [10] M. García-Hernández, J. L. Martínez, M. J. Martínez-Lope, M. T. Casais, and J. A. Alonso, *Phys. Rev. Lett.* **86**, 2443 (2001).
- [11] K.-I. Kobayashi, T. Kimura, Y. Tomioka, H. Sawada, K. Terakura, and Y. Tokura, *Phys. Rev. B* **59**, 11159 (1999).
- [12] J. B. Philipp, D. Reisinger, M. Schonecke, A. Marx, A. Erb, L. Alff, J. Klein, R. Gross, *Appl. Phys. Lett.* **79**, 3654 (2002).
- [13] J. B. Philipp, D. Reisinger, M. Schonecke, A. Marx, A. Erb, L. Alff, and R. Gross, *J. Appl. Phys.* **93**, 6853 (2003).
- [14] J. B. Philipp, P. Majewski, L. Alff, A. Erb, R. Gross, T. Graf, M.S. Brandt, J. Simon, T. Walther, W. Mader, D. Topwal, D.D. Sarma, *Phys. Rev. B* **68**, 144431 (2003).
- [15] D. Serrate, J. M. De Teresa, J. Blasco, M. R. Ibarra, L. Morellón, and C. Ritter, *Appl. Phys. Lett.* **80**, 4573 (2002).
- [16] J. Navarro, C. Frontera, Ll. Balcells, B. Martínez, and J. Fontcuberta, *Phys. Rev. B* **64**, 092411 (2001).
- [17] J.H. Park, S.K. Kwon, B.I. Min, *Phys. Rev. B* **65**, 174401 (2002).
- [18] K. Ueda, H. Tabata, T. Kawai, *Science* **280**, 1064 (1998).
- [19] W.E. Pickett, *Phys. Rev. B* **57**, 10613 (1998); see also *Science* **281**, 1571a (1998).
- [20] Ll. Balcells, J. Navarro, M. Bibes, A. Roig, B. Martínez, and J. Fontcuberta, *Appl. Phys. Lett.* **78**, 781 (2001).
- [21] J. Gopalakrishnan, A. Chattopadhyay, S. B. Ogale, T. Venkatesan, R. L. Greene, A. J. Millis, and K. Ramesha, B. Hannoyer, and G. Marest *Phys. Rev. B* **62**, 9538 (2000).
- [22] W. Westerburg, O. Lang, C. Ritter, C. Felser, W. Tremel, and G. Jakob, *Solid State Comm.* **122**, 201 (2002).
- [23] W. Prellier, V. Smolyaninova, A. Biswas, C. Galley, R. L. Greene, K. Ramesha, and J. Gopalakrishnan, *J. Phys.: Condens. Matter* **12**, 965 (2000).
- [24] P. D. Battle, T. C. Gibb, A. J. Herod, S.-H. Kim, P. M. Munns, *J. Mater. Chem.* **5**, 865 (1995).
- [25] R. Rodriguez, A. Fernandez, A. Isalgue, J. Rodriguez, A. Labarta, J. Tejada, and X. Obradors, *J. Phys.* **18**, L401 (1985).
- [26] T.C. Gibb, *J. Mater. Chem* **3**, 441 (1993).
- [27] A.K. Azad, S.-G. Erikson, A. Mellergard, S.A. Ivanov, J. Eriksen, H. Rundlöf, *Mat. Res. Bull.* **37**, 1797 (2002).
- [28] H. Kawanaka, I. Hase, S. Toyama, Y. Nishihara, *Physica B* **284-288**, 1428 (2000); see also *Physica B* **281-282**, 518 (2000).
- [29] K.-I. Kobayashi, T. Okuda, Y. Tomioka, T. Kimura and Y. Tokura, *J. Magn. Magn. Mater.* **218**, 17 (2000).
- [30] M.J. Martinez-Lope, J.A. Alonso, M.T. Casais, M.T. Fernandez-Diaz, *Z. Naturforsch.* **58b**, 127 (2003).

- [31] A. K. Azad, S. A. Ivanov, S.-G. Eriksson, J. Eriksen, H. Rundlöf, R. Mathieu, and P. Svedlindh, *Materials Research Bulletin* **36**, 2215 (2000).
- [32] A. K. Azad, S. A. Ivanov, S.-G. Eriksson, J. Eriksen, H. Rundlöf, R. Mathieu, and P. Svedlindh, *Materials Research Bulletin* **36**, 2485 (2000).
- [33] A. K. Azad, S. Ivanov, S. -G. Eriksson, H. Rundlöf, J. Eriksen, R. Mathieu, and P. Svedlindh, *J. Magn. Magn. Mater.* **237**,124 (2001).
- [34] C. R. Wiebe, J. E. Greedan, G. M. Luke, *Phys. Rev.* **B 65**, 144413 (2002).
- [35] D. Iwanga, Y. Inaguma, M. Itoh, *Mat. Res. Bull.* **35**, 449 (2000).
- [36] H. Karundasa, Q. Huang, B. G. Ueland, P. Schiffer, R. J. Cava, *PNAS* **100**, 8097 (2003).
- [37] A. P. Ramirez, *Annu. Rev. Mater. Sci.* **24**, 453 (1994).
- [38] J. E. Greedan, *J. Mater. Chem.* **11**, 37 (2001).
- [39] R. Moessner, *Can. J. Phys.* **79**, 37 (2001); see also *Phys. Rev. Lett.* **93**, 3293 (1999).
- [40] M. J. Harris, S. T. Bramwell, P.C.W. Holdsworth, J.D.M. Champion, *Phys. Rev. Lett.* **79**, 2554 (1997); see also *Phys. Rev. Lett.* **81**, 4496 (1998) and *Nature* **399**, 311 (1999).
- [41] A. P. Ramirez, A. Hayashi, R. J. Cava, R. Siddharthan, B. S. Shastry, *Nature* **399**, 333 (1999); see also *Phys. Rev. Lett.* **89**, 067202 (2002).
- [42] Y. Moritomo, Sh. Xu, A. Machida, T. Akimoto, E. Nishibori, M. Takata, and M. Sakata, *Phys. Rev. B* **61**, R7827 (2000).
- [43] Y. Moritomo, Sh. Xu, T. Akimoto, A. Machida, N. Hamada, K. Ohoyama, E. Nishibori, M. Takata, and M. Sakata, *Phys. Rev. B* **62**, 14224 (2000).
- [44] K. Phillips, A. Chattopadhyay, and A. J. Millis, *Phys. Rev. B* **67**, 125119 (2003).
- [45] D. D. Sarma, P. Mahadevan, T. Saha-Dasgupta, Sugata Ray, and A. Kumar, *Phys. Rev. Lett.* **85**, 2549 (2000); see also *Curr. Opinion in Solid State Mat. Sci.* **5**, 261 (2001).
- [46] J. Kanamori and K. Terakura, *J. Phys. Soc. Jpn.* **70**, 1433 (2001).
- [47] Z. Fang, K. Terakura, and J. Kanamori, *Phys. Rev. B* **63**, R180407 (2001).
- [48] C. Zener, *Phys. Rev.* **82**, 403 (1951).
- [49] P.W. Anderson, H. Hasegawa, *Phys. Rev.* **100** 67 (1955).
- [50] J.H. Jung, S.-J. Oh, M.W. Kim, T.W. Noh, J.-Y. Kim, J.-H. Park, H.-J. Lin, C.T. Chen, Y. Moritomo, *Phys. Rev. B* **66**, 104415 (2002).
- [51] H. Wu, *Phys. Rev. B* **64**, 125126 (2001).
- [52] M. Tovar, M. T. Causa, and A. Butera, J. Navarro, B. Martinez, and J. Fontcuberta, M. C. G. Passeggi, *Phys. Rev. B* **66**, 024409 2002.
- [53] J. B. Philipp, P. Majewski, D. Reisinger, S. Geprägs, M. Opel, L. Alff, A. Erb, R. Gross, *Acta Polonica Physica*, in press (2003).
- [54] J. B. Philipp, Ph.D. Thesis, Technical University of Munich (2003).

Study of the Magnetic Properties of Nb-based Double Perovskites

N. Rama^a, M. Opel, J.B. Philipp, K. Chandrasekaran^a, V. Sankaranarayanan^b, M.S. Ramachandra Rao^a, and R. Gross¹

^a Materials Science Research Centre, Indian Institute of Technology Madras, Chennai 600036, India

^b Department of Physics, Indian Institute of Technology Madras, Chennai 600036, India

Within a bilateral German-Indian cooperation project, we have studied the magnetic properties of $A_2B\text{NbO}_6$ ($A = \text{Ba}, \text{Sr}, (\text{BaSr})$; and $B = \text{Fe}, \text{Mn}$) double perovskites. It is found that $\text{Ba}_2\text{FeNbO}_6$ is an antiferromagnet revealing weak ferromagnetic correlations below 5 K, while $\text{Ba}_2\text{MnNbO}_6$ shows two magnetic transitions: one at 45 K and the other at 12 K (see Fig. 1). It is also seen that the Néel temperatures T_N of the $A_2\text{FeNbO}_6$ ($A = \text{Ba}, \text{Sr}, \text{BaSr}$) compounds do not vary significantly. However, variations in the average A-site ionic radius influence the formation of short range correlations that persist above T_N .

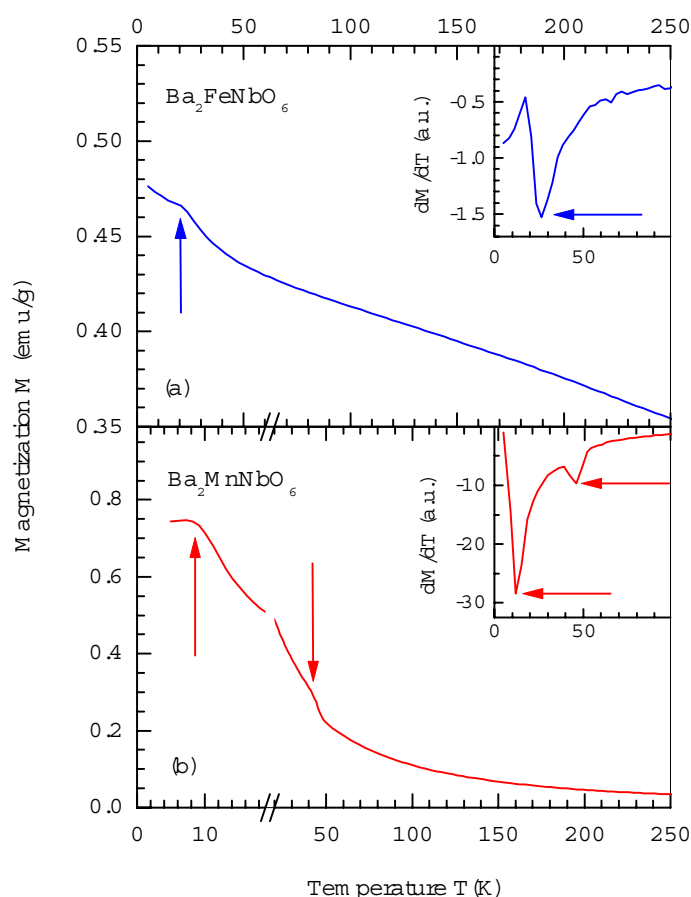


Figure 1: Temperature variation of the magnetization for $\text{Ba}_2\text{FeNbO}_6$ (a) and $\text{Ba}_2\text{MnNbO}_6$ (b). Vertical arrows point to T_N . The insets show the temperature derivative $dM(T)/dT$ in arb. units. Horizontal arrows point to the minima (see text).

Double perovskites of the general form $A_2B'B''O_6$ ($A = \text{Sr}, \text{Ca}, \text{Ba}$; $B = \text{Fe}, \text{Mn}, \text{Cr}$; $B' = \text{Mo}, \text{W}, \text{Ta}, \text{Nb}$) are actively investigated in order to understand the nature of magnetism and magnetotransport in ferromagnetic oxides. It is known that the B site can accommodate two kinds of metal ions. The cation arrangement on the B-sublattice of a double perovskite is controlled primarily by the charge difference between the B cations and secondarily by the ionic size difference between them. Depending on the valence state and the ionic radii, the B-site cations may show a sublattice ordering or may be more or less disordered [1]. Therefore, the B-site cations generally determine the physical properties of perovskites. Different kinds of B and B' ion pairs show a variety of physical properties of ordered perovskites. For example, $\text{Sr}_2\text{FeMoO}_6$ is a ferromagnetic metal with a Curie temperature T_C of about 400 K [2, 3], while $\text{Sr}_2\text{MnMoO}_6$ is an antiferromagnetic insulator with $T_N \approx 12$ K [3]. With this in mind, we have studied the magnetic properties of $\text{Ba}_2\text{FeNbO}_6$ and $\text{Ba}_2\text{MnNbO}_6$ to investigate the effect of the Jahn-Teller ion Mn^{3+} in comparison to Fe^{3+} . We have also studied the magnetic behaviour of

¹This work was done within a German-Indian science and technology cooperation project funded by the BMBF (project IND 01/009).

$A_2\text{FeNbO}_6$ with $A=\text{Ba}$, Sr , and (BaSr) to check the influence of the A-site ion on the magnetic properties.

For the preparation of the samples, pure (99.9 %) carbonates of the alkaline earths BaCO_3 and SrCO_3 , oxides of the transition metals Fe_2O_3 , MnO_2 , and Nb_2O_5 were taken and weighed stoichiometrically. The weighed powders were intimately mixed using an agate mortar and calcined at 1200°C for 24 h. This procedure was repeated three times and the resulting powder was pressed into pellets and sintered at 1350°C . The phase purity was checked using x-ray diffraction. The DC magnetization was measured using a SQUID magnetometer (MPMS XL-7, Quantum Design) in the field-cooled mode (FC).

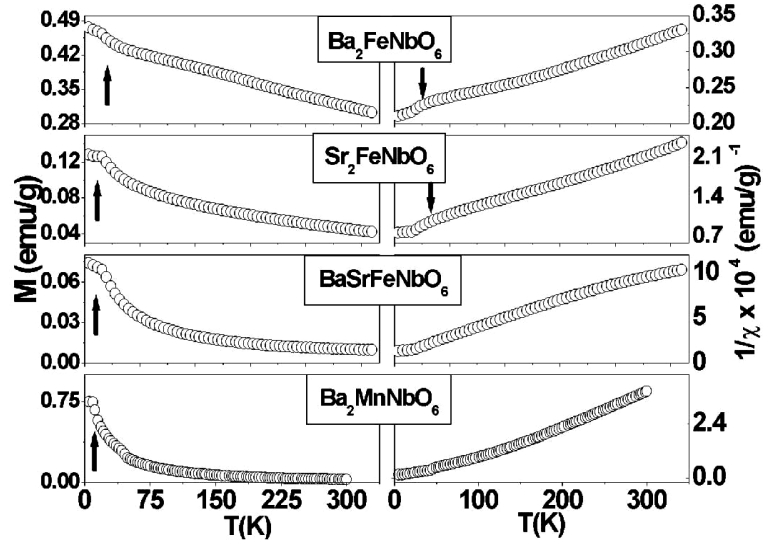


Figure 2: Left panel: $M(T)$ for $\text{Ba}_2\text{FeNbO}_6$, $\text{Sr}_2\text{FeNbO}_6$, $(\text{BaSr})_2\text{FeNbO}_6$, and $\text{Ba}_2\text{MnNbO}_6$. The arrows point to T_N . Right panel: Corresponding $\chi^{-1}(T)$ plots. The arrows indicate the magnetic correlations above T_N .

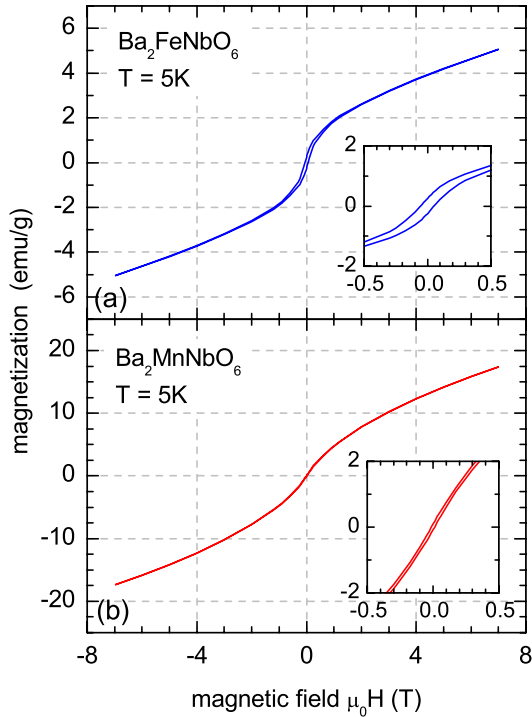


Figure 3: $M(H)$ for $\text{Ba}_2\text{FeNbO}_6$ (a) and $\text{Ba}_2\text{MnNbO}_6$ (b) at 5 K. $\text{Ba}_2\text{FeNbO}_6$ shows a weak ferromagnetic hysteresis (inset).

The temperature variation of the magnetization in $\text{Ba}_2\text{FeNbO}_6$ is shown in Fig. 1(a). The temperature derivative of the magnetization shows a minimum at 25 K (see inset of Fig. 1a). $\chi^{-1}(T)$ does not show a linear behavior throughout the entire measured temperature range, indicating the absence of Curie-Weiss behavior for $\text{Ba}_2\text{FeNbO}_6$ (Fig. 2b). Magnetic hysteresis is seen at 5 K (see Fig. 3a) revealing the presence of weak ferromagnetic behavior.

The magnetization for $\text{Ba}_2\text{MnNbO}_6$ shows two distinct minima, one at 45 K and the other at 12 K (Fig. 1b). The minimum at low temperature is attributed to the Néel temperature. To determine the origin of the high temperature minimum we refer to neutron and magnetization measurements in Ba_2MnWO_6 by Azad *et. al.*, who report a Néel temperature at 9 K and a canted antiferromagnetic like state below 45 K [4].

Comparing those data to ours, we attribute the high temperature minimum corresponding to the shoulder in the $M(T)$ plot to a canted antiferromagnetic state. Curie-Weiss behaviour is

seen at high temperatures (above 200 K), which yields a Curie constant of $3.33 \text{ emu mol}^{-1} \text{ K}^{-1}$ and a Weiss temperature of -59 K . The negative sign indicates a antiferromagnetic correlations. The value of the effective Bohr magneton number (μ_B) calculated from the fit yields a value of $5.18 \mu_B$, which is nearly equal to the expected spin-only value for Mn^{3+} equal to $4.9 \mu_B$. There is no magnetic hysteresis seen at 5 K (see Fig. 3b) indicating that there is a complete antiferromagnetic ordering below T_N unlike in $\text{Ba}_2\text{FeNbO}_6$.

All the three A_2FeNbO_6 compounds with $A = \text{Ba, Sr, (BaSr)}$ do not show a linear behaviour in $\chi^{-1}(T)$ in the measured temperature region up to 350 K (Fig. 2). However, it is seen that the persistence in magnetic correlations above T_N , (seen as hump in $\chi^{-1}(T)$) vary as we vary the ion at the A-site. The extent of this correlation is lowest for $(\text{BaSr})_2\text{FeNbO}_6$. This is because among the three compounds, $(\text{BaSr})_2\text{FeNbO}_6$ has the highest variance in the A-site cation radii [5], which could have hindered the formation of short-range magnetic correlations.

In conclusion, we have studied the magnetic properties of different Nb-based double perovskites A_2BNbO_6 with $A = \text{Ba, Sr, (BaSr)}$ and $B = \text{Fe, Mn}$. $\text{Ba}_2\text{FeNbO}_6$ and $\text{Ba}_2\text{MnNbO}_6$ are antiferromagnetic insulators with Néel temperatures of $T_N = 25 \text{ K}$ and 12 K respectively. The Néel temperatures of the A_2FeNbO_6 compounds with $A = \text{Ba, Sr, (BaSr)}$ do not vary significantly. However variations in the average A-site ionic radius influences the formation of short range correlations that persist above T_N .

References

- [1] M.T. Anderson, K.B. Greenwood, G.A. Taylor, and K.R. Poeppelmeier, *Progress in Solid State Chemistry* **22**, 197 (1993).
- [2] K.I. Kobayashi, T. Kimura, H. Sawada, K. Terakura, and Y. Tokura, *Nature (London)* **395**, 677 (1998).
- [3] M. Itoh, I. Ohta, and Y. Inaguma, *Materials Science and Engineering B* **41**, 55 (1996).
- [4] A.K. Azad, S.A. Ivanov, S.-G. Eriksson, J. Eriksen, H. Rundolf, R. Mathieu, and P. Svedlindh, *Materials Research Bulletin* **36**, 2215 (2001).
- [5] J.P. Attfield, *Chemistry of Materials* **10**, 3239 (1998).

Magnetization of the Nuclear Spin Ordered Phases of Solid ^3He : Pulsed NMR and SQUID Magnetometry

Erwin Schubert^a, Carmen Millan-Chacartegui, Matthias Kath, Stephan Schöttl^a, and Konrad Siemensmeyer^b¹

^a National Physics Laboratory, London, UK.

^b Hahn-Meitner Institute, Berlin, Germany.

Regarding the nuclear spin structure of the magnetically ordered phases of solid ^3He there is still need to increase the experimental data basis to clarify the nature of the magnetic exchange interactions. For this purpose we perform neutron scattering measurements at the Hahn-Meitner Institute at Berlin. It is crucial for these experiments that a single crystal can be formed in the sinter needed to cool the solid ^3He and that the sample remains in the ordered state long enough under neutron irradiation. On the way to meet these goals we built a cell for pulsed NMR measurements on solid ^3He in a 700 \AA sinter and looked for the existence of a single crystal, which would be indicated by the characteristic line splitting of the U2D2 phase. [1] The cell temperature and its warmup behavior after demagnetization of our 0.9 mole PrNi₅ nuclear stage was monitored by pulsed NMR on a Cu sample thermally connected to it.

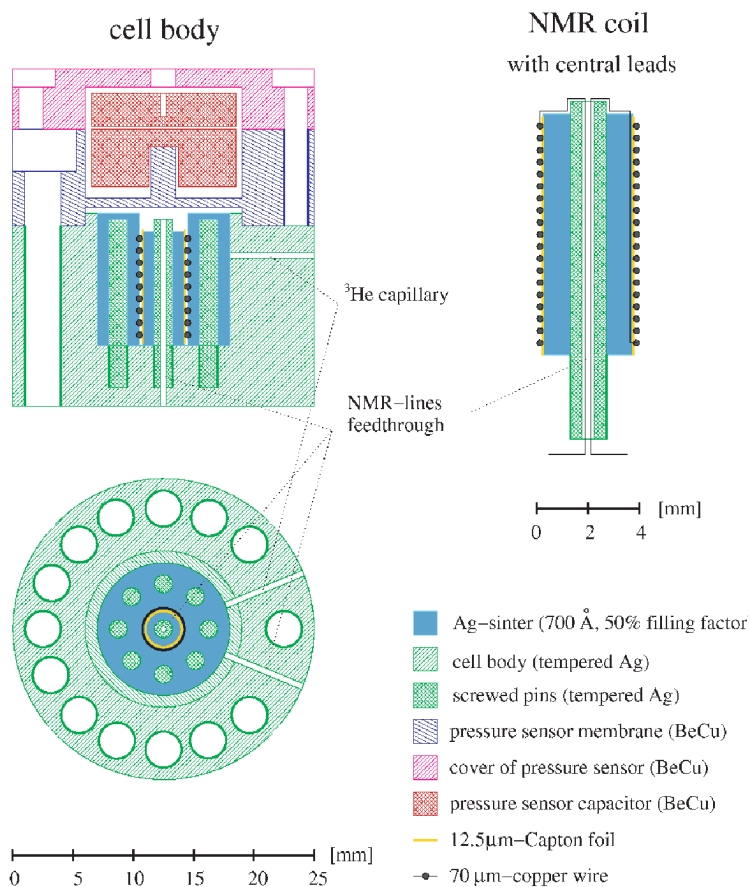


Figure 1: Drawing of pressure cell with internal NMR coil and capacitive Straty-Adams pressure transducer.

NMR spectra from solid ^3He were taken with a copper coil around a Ag sinter through which the solid is cooled. This sinter is connected to a 2 mm diam. Ag rod screwed into the cell body. Details of the cell design are shown in Fig. 1. For the pulsed NMR thermometry on ^{63}Cu a pulse interval of 4 h was necessary to ensure full recovery of the magnetization and thermal equilibrium of the coil. From the warming rate below 1 mK and knowing the specific heat capacity of our nuclear stage, we calculated the warming under neutron irradiation of the Berlin pressure cell, which is attached to a nearly identical nuclear stage. This simulation gave a time interval of the order of 30 min during which the solid ^3He sample should stay in the ordered state, long enough to search for the expected $(1/2,0,0)$ reflection of the U2D2 phase.

¹This work is supported by the the EU in collaborative network involving the HMI Berlin, the Royal Holloway University, London, the CNRS Grenoble, the Univesité Paris, Saclay, and the University of Florida, Gainesville.

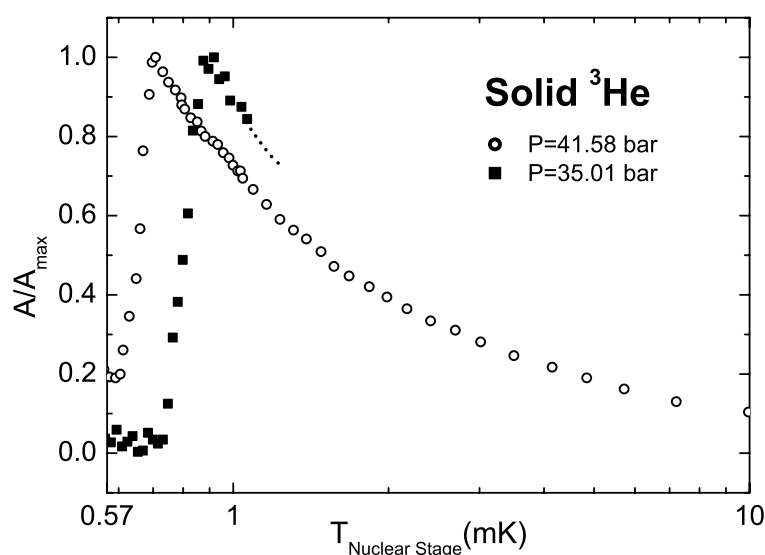


Figure 2: NMR intensity of solid ^3He vs the cell temperature at 2 different molar volumes: 23.4 cc/mole (open circles) and 24.15 cc/mole (filled squares).

body. The intensities were derived from the Fast Fourier Transform of the free induction decay. It is remarkable that the intensities are nearly zero in the U2D2 phase which has never been observed before. The first spectra at the lowest temperatures were taken 24 h after the end of the demagnetization to make sure that the solid was in thermal equilibrium with the sinter and with the cell body.

In the third attempt to grow a single crystal, more care was taken to stop the solidification just after reaching the melting curve and then to continue slowly (6h) to obtain full growth and additionally 4 h to cool the sample to sub-mK temperatures. The final cell pressure was again 35.01 bar and hence the molar volume 24.15 cc. In the NMR spectra this time two (or possibly three) extra peaks on the high frequency side of the Larmor line (955 kHz) were found which disappeared continuously while the sample warmed through T_N .

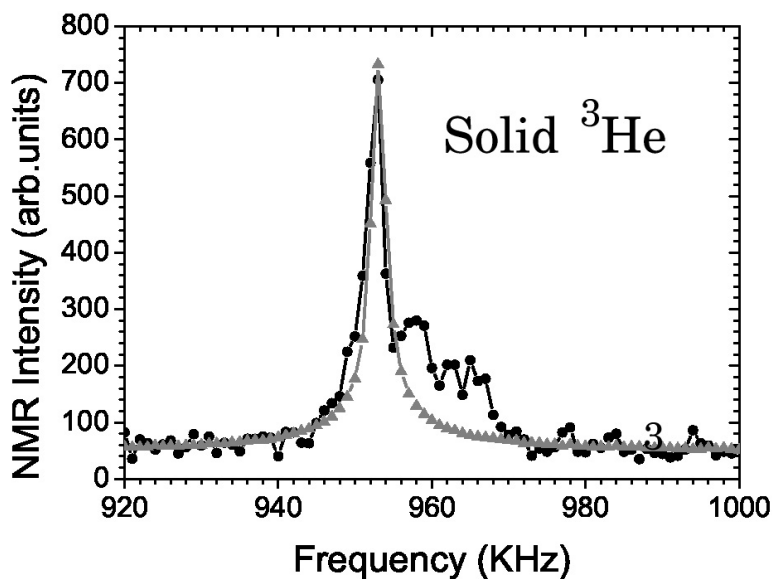


Figure 3: NMR spectrum of solid ^3He in a 700 Å Ag sinter in the nuclear ordered phase at $p=35.01$ bar and $T \approx 600 \mu\text{K}$ (dots). The tipping angle was $\approx 10^\circ$. The triangles show a scaled line from above T_N .

We also cooled the 23.4 cc/mole sample into the high field phase and measured NMR spectra and line intensities there. The result showed the expected enhancement for this weak ferromagnetic phase. Fig. 3. shows a comparison of the spectrum in the ordered phase and a scaled spectrum (to match the maximum) in the paramagnetic phase. Again it has to be noticed that the NMR intensities were very low, about 1% as compared to the maximum just above T_N . From Fig. 3 it

We performed several runs with the attempt to grow a single crystal in the sinter, all with the blocked capillary method starting around 58 bar at 4.2 K. The first ended at a cell pressure of 41.58 bar (i.e. 23.4 cc/mole), the second and third at 35.01 bar (24.15 cc/mole). NMR signal intensities of the first two solid ^3He samples grown to end at final pressures of 41.58 bar and 35.01 bar are shown in Fig. 2 versus the temperature of the nuclear stage which is practically identical to that of the cell

is quite clear that there is a line splitting for our 3^d sample which was not found in the first two cases. These two, on the other hand, had even lower intensities in the ordered phase with respect to the maximum just above T_N . The line splitting in the third attempt indicates that we had two magnetic domains of U2D2 structure oriented close to 90° of the plane normal vector with respect to the external field which would give only a small deviation from the Larmor line.

There may have been more randomly oriented crystallites and magnetic domains which distributed the intensities of their splittings over such a wide frequency range that we could not observe them. In the first two attempts, due to the fast crystal growth, we had only such crystallites. Another possibility is that the majority of the crystallites (or magnetic domains) do not order in the U2D2 phase in the sinter. The result of the third case gives us some encouragement, that with even longer growth times a single crystal with a small number of magnetic domains can be grown in the sinter for the neutron experiments. Indeed, the HMI group has already found a crystalline (1,0,0) reflection.

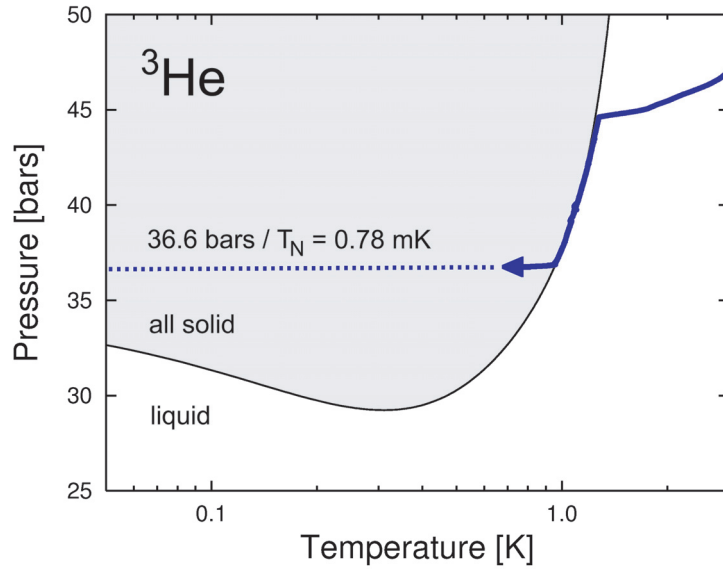


Figure 4: Pressure vs temperature during growth of a ^3He crystal

In order to further check the observed drop of the NMR intensity in the ordered phase we built a new pressure cell with an extension that fits into the pickup coil of our SQUID magnetometer (see Fig. 5). With this cell we put still more emphasis on the crystal growth conditions and regulated the temperature at the high side of the melting curve for several hours to ensure an homogeneous

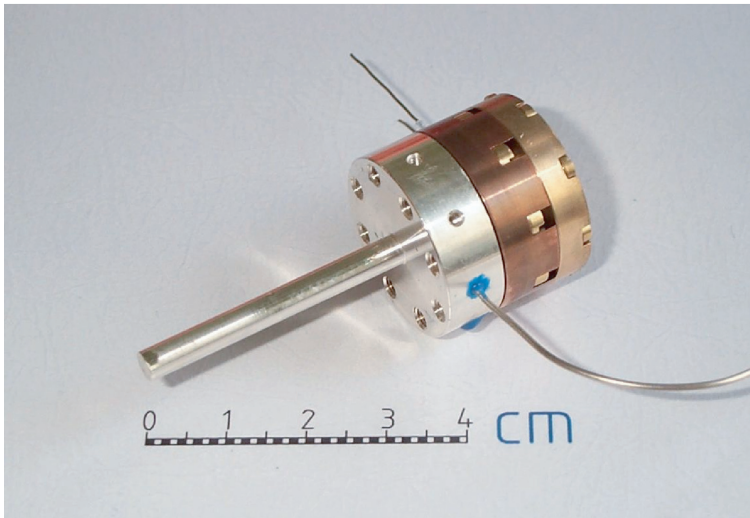


Figure 5: Pressure cell for measuring the static susceptibility of solid ^3He in a SQUID system.

growth throughout the sinter.

Up to now the solid in the cell has reached a final temperature of 1.2 mK but not yet the nuclear ordered state. The reason seems to be the high temperature of the pickup coil, which is thermally anchored at the distillation chamber which itself is done to provide a thermally stable reservoir dur-

ing the operation of the dilution refrigerator. Fig. 6 finally shows the first results for the inverse susceptibility obtained with this cell. They exhibit slight deviations from the Curie-Weiss law below 4 mK and a somewhat too large Weiss constant for the $23.75 \text{ cm}^2/\text{mole}$ sample. More experiments to reach the ordered states and to clarify the situation are under way. In Berlin, our efforts concentrate on reaching low temperatures, a final value of 5 mK has been reached recently.

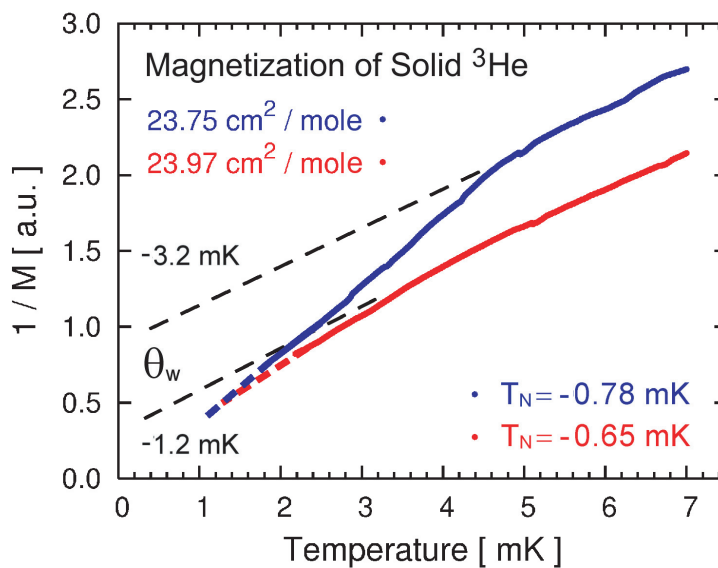


Figure 6: Result of 4th demagnetization: χ^{-1} vs T of solid ^3He for two different pressures and thus different molar volumes

References

- [1] D.D. Osheroff *Journ. Low Temp. Physics* **87**, 297 (1992)

Investigation of Superconductor/Manganite Junctions

Mitja Schonecke, Bettina Welter, Achim Marx, Lambert Alff, and Rudolf Gross¹

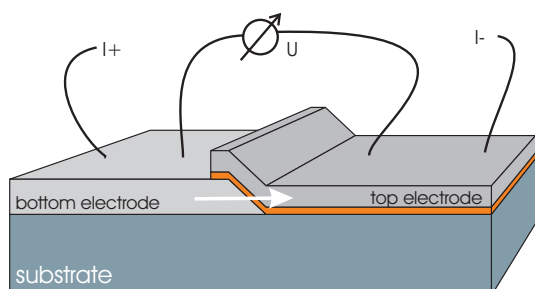


Figure 1: Geometry of a ramp-type junction. The c -axis oriented electrodes are coupled along their ab -plane.

The investigation of interfaces in high-temperature superconductors (HTS) is important both for the basic understanding of this class of materials and for applications. The so-called ramp-type junction is a universal sample structure to study the electrical transport properties across interfaces between oxides and other materials along the ab -plane. This is particularly important for the HTS materials, since one can take advantage of the larger coherence length in this crystallographic direction. Fig. 1 shows a sketch of the ramp junction geometry. After the deposition of the bottom electrode and an insulating layer, which prevents coupling of the electrodes in c direction, a ramp is formed by optical

photolithography and Argon ion beam etching. To remove the degraded layer developing near the interface because of the ion impact, an additional etching step is performed with oxygen ions at temperatures up to 780°C [1]. After this surface cleaning an optional insulating barrier is deposited on the ramp followed by the top electrode.

During the last year we prepared ramp-type junctions consisting of the HTS material $\text{YBa}_2\text{Cu}_3\text{O}_{7-\delta}$ (YBCO) and the ferromagnetic manganite $\text{La}_{2/3}\text{Ba}_{1/3}\text{MnO}_3$ (LBMO) in order to study the interplay of ferromagnetism (FM) and unconventional superconductivity as a function of the interface transparency. As epitaxial barrier material SrTiO_3 (STO) was used. Of particular interest was the influence of the high spin polarization in the doped manganite on the so-called Andreev bound states (ABS) [3] present at (110)-oriented surfaces of the superconductor. The ABS are known to give rise to a zero bias conductance peak (ZBCP) in tunnelling spectra.

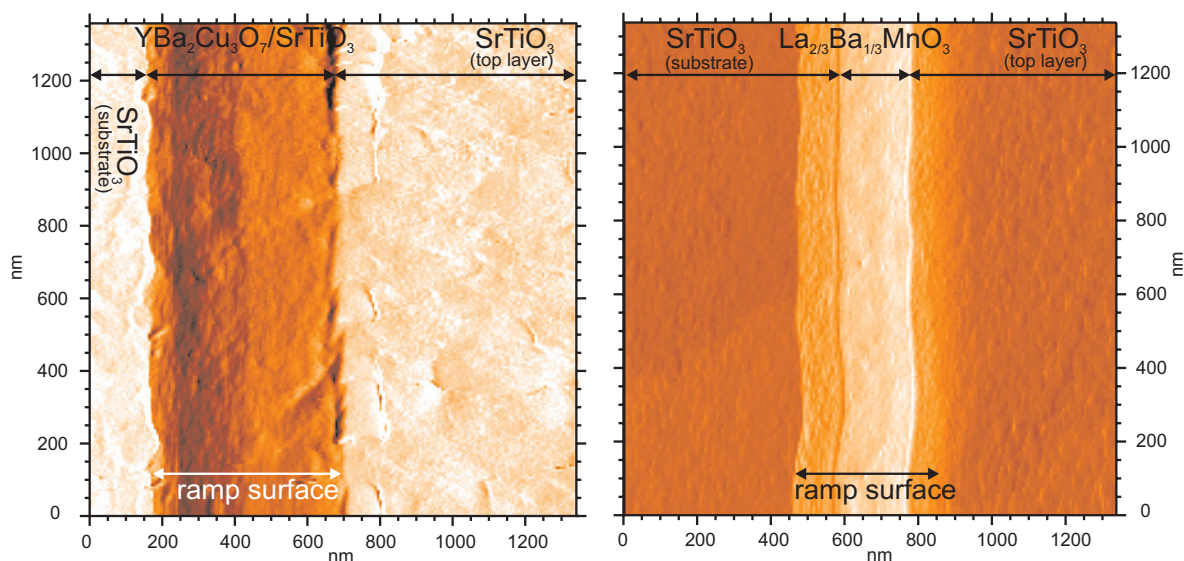


Figure 2: Comparison of atomic force microscopy images of the ramps in YBCO/STO (left) and LBMO/STO epitaxial bilayers (right). The manganite ramp has a much smoother surface.

¹This work is supported by the Deutsche Forschungsgemeinschaft.

It turned out that using the manganite as the bottom electrode yields a much smoother ramp surface in comparison to ramps in YBCO. Fig. 2 shows two Atomic Force Microscopy (AFM) force images of cleaned ramp surfaces in both materials. The advantage of the force images is the accentuation of edges and spots on the surface, which leads to a better insight in the topography on the ramp surface, although no real height information is contained in the image. The force images clearly show the ramp surface between two flat STO areas. To the left of the ramp area there is the STO substrate, whereas to the right we have the surface of the bilayer. Due to the different etching rates of LBMO and STO, the ramp region in the right picture is divided in three parts: the light stripe shows the ramp in LBMO, the orange stripes in the STO substrate and the top layer, respectively. In the YBCO ramp these regions can hardly be distinguished, because of the very similar etching rates of YBCO and STO. We used LBMO as a bottom layer to grow epitaxial heterostructures with optional STO barriers and YBCO as the counter electrode.

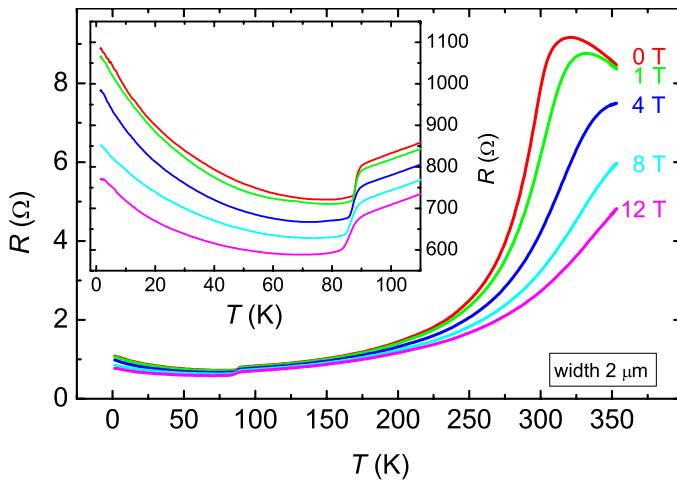


Figure 3: Resistance versus temperature of an LBMO/YBCO junction without artificial barrier. Above 80 K it is dominated by the resistance of the electrodes, while below this temperature an additional contribution gives rise to an increase with decreasing temperature.

In general, LBMO/YBCO junctions showed tunnelling behavior, even when no artificial barrier was deposited. A possible explanation is strain at the interface due to the lattice mismatch between the materials, which influences the transport properties of the junction [2]. The influence of this natural barrier can be seen in the $R(T)$ curve shown in Fig. 3. The resistance of the junction is a series connection of the resistance of both electrodes and the additional barrier. At temperatures above 80 K the electrodes dominate the resistance, the superconducting transition of the YBCO film can be seen at about 90 K. Below 80 K the resistance starts to increase, which is not caused by the electrodes. They show metallic respectively superconducting behavior. So there has to be an additional contribution to the junctions resistance, which dominates the transport properties at lower temperatures.

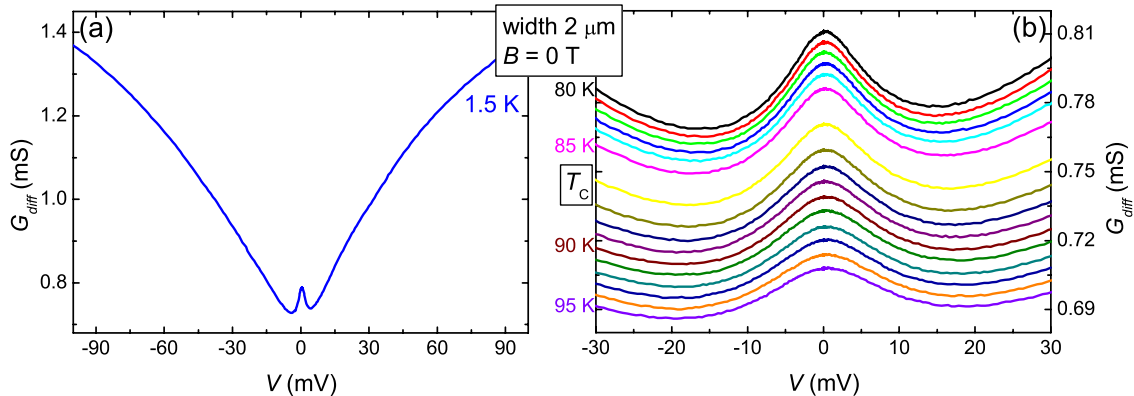


Figure 4: Differential conductance versus voltage of an LBMO/YBCO junction at zero magnetic field. (a) Spectrum at 1.5 K. (b) Series of spectra around the critical temperature of the YBCO.

Fig. 4a shows a the differential conductance $G_{\text{diff}} = dI/dV$ versus voltage dependence of an LBMO/YBCO junction at 1.5 K. Here, the existence of an insulating barrier is also obvious, as it results in an voltage dependent background conductivity, commonly observed in tunnelling spectra with

oxide barriers [4]. The maximum at zero bias is further investigated in Fig. 4b. Here, the spectra are plotted for the temperature range from 80 K, where the YBCO is in the superconducting state, up to 95 K, where the YBCO is normal conducting. In this temperature region the resistivity of the junctions is increasing with temperature, so that the conductivity is decreasing. The transition of the YBCO film to the normal state can be seen in the larger distance between the two spectra below the 85 K curve. As the ZBCP is still present above T_C , ABS can be ruled out as an explanation, because they are a manifestation of a phase shift in the superconducting pair potential.

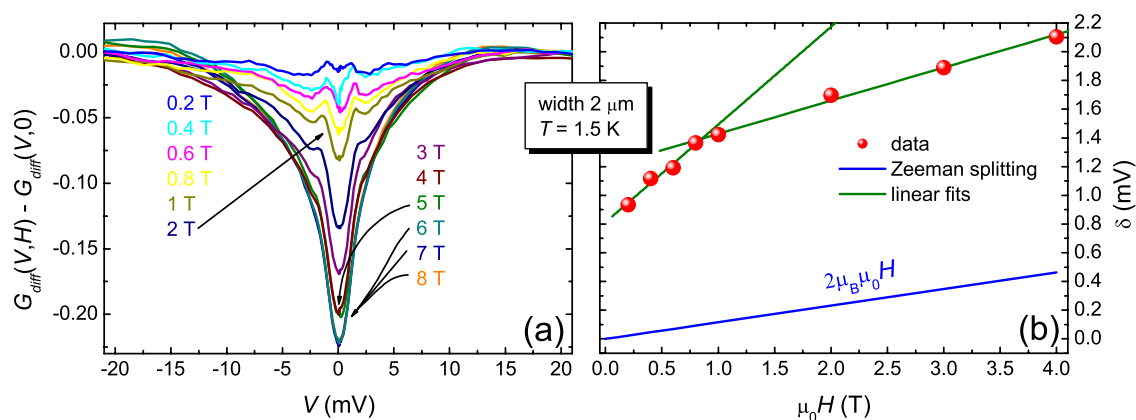


Figure 5: Tunneling spectra of a LBMO/YBCO junction for different applied magnetic fields at 1.5 K. (a) The curve at zero field has been subtracted to show the evolution in detail. (b) Splitting δ plotted versus the applied magnetic field. Also shown is the expected Zeeman splitting.

An alternative mechanism leading to ZBCP in tunnelling spectra is Kondo scattering at magnetic impurities in the interfaces region. This has been investigated theoretically by Anderson [5] and Appelbaum [6] in 1966. In the strained interface region this type of scattering can be caused by manganese ions. If the ZBCP is based on this scattering mechanism, one expects a Zeeman splitting on applying a magnetic field. Fig. 5a shows the normalized spectra in magnetic fields up to 8 T. Here, the zero field curve $G_{\text{diff}}(V,0)$ has been subtracted from the measured spectra $G_{\text{diff}}(V,H)$. The dip developing at zero bias is due to the suppression of the ZBCP in the magnetic field. Also visible are two maxima (located at M_+ and M_-), which can be interpreted as a splitting of the ZBCP. Fig. 5b shows the dependence of $\delta = 1/2(M_+ - M_-)$, which is half the distance between the maxima, on the magnetic field. In contrast to the linear Zeeman splitting also drawn in Fig. 5b, the observed dependence shows a change in slope, as indicated by the linear fits. Thus, Kondo scattering in the barrier region cannot be the only reason for the observed ZBCP.

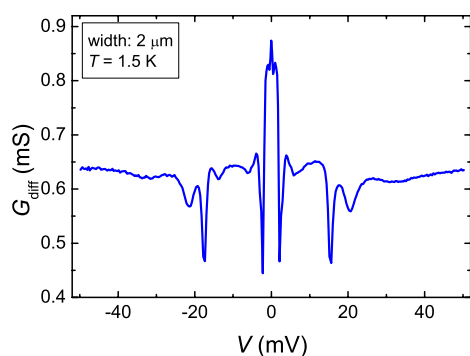


Figure 6: Differential conductivity versus voltage of a YBCO/STO/LBMO ramp junction with a 2 nm thick STO barrier.

The development of the natural barrier can be prevented by depositing a thin barrier of STO between the electrodes. The thickness has to be sufficiently small, so that no closed film is obtained and micro shorts provide a good contact between the electrodes. In these holes there seems to exist a highly transparent interface and the junction conductance is then dominated by Andreev-reflection. The differential conductance vs. voltage curves of junctions prepared with a manganese bottom electrode and a thin barrier (2 nm) showed multiple sharp dips and a peak at zero bias (Fig 6). The origin of these features is still unclear. Kashiwaya *et al.* [8, 9] recently published measurements on tunnelling junctions composed of $\text{La}_{2/3}\text{Sr}_{1/3}\text{MnO}_3$ and

$\text{YBa}_2\text{Cu}_3\text{O}_{7-\delta}$. They observed a pair of dips symmetrically around zero bias, which might be due to phase coherent transport in the junction. In our samples it is possible that some current paths through the leaky barrier show quantum interference effects, which manifest themselves as peaks and dips in the conductance spectra. In a magnetic field the central peak persists up to 15 T, while the dip features are shifted to lower voltages and get suppressed. High peaks at zero bias have been reported by Pan *et al.* [7] in tunnelling spectra of $\text{Bi}_2\text{Sr}_2\text{CaCu}_2\text{O}_8$ surfaces with Zn impurities. Scattering at nonmagnetic impurities might lead to a zero bias peak, which should not be sensitive to magnetic fields.

A crucial feature of oxide junctions is the interdependence between their transport properties and the local oxygen stoichiometry at the interface in the tunnelling barrier, respectively. At low temperatures the diffusion of oxygen is largely reduced compared to room temperature, so the oxygen distribution remains the same. In our samples we have often seen a change in the shape of the spectra after thermal cycling up to room temperature. Fig. 7a shows as an example the dramatic change of the spectrum already discussed above. While the dips disappear, the background conductance is getting bias dependent, which is a characteristic of tunnelling junctions. An oxygen annealing step partially recovered the spectral features, as is shown in Fig. 7b. This demonstrates that the transport properties of oxide junctions can be strongly influenced by a small change in the oxygen stoichiometry at the interface and that this process is, at least partially, reversible.

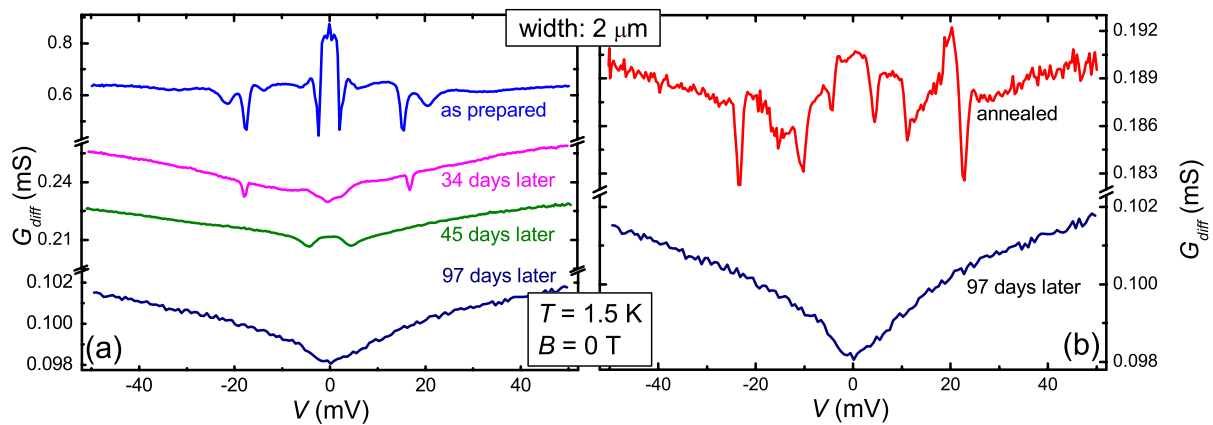


Figure 7: (a) Differential conductance versus voltage curves of a YBCO/STO/LBMO ramp junction measured after different storing periods. (b) Effect of oxygen annealing at 600°C .

In conclusion we have developed a thin film process technology, which allows the preparation of heterostructures in ramp-type geometry, containing different materials. The formation of the ramp has been extensively investigated and samples with superconducting and ferromagnetic electrodes have been prepared. Depending on the barrier transparency, the conductivity spectra showed features of, up to now, unknown origin. Further investigations are required to clarify the underlying transport mechanisms.

References

- [1] U. Schoop, M. Schonecke, S. Thienhaus, S. Schymon, L. Alff, R. Gross, *Physica C* **351**, 200 (2001).
- [2] U. Schoop, M. Schonecke, S. Thienhaus, F. Herbstritt, J. Klein, L. Alff, R. Gross, *Physica C* **350**, 237 (2001).
- [3] C. R. Hu, *Phys. Rev. Lett.* **72**, 1526 (1994); C. Yang and C. R. Hu, *Phys. Rev. B* **50**, 16766 (1994).
- [4] J. R. Kirtley, S. Washburn, and D. J. Scalapino, *Phys. Rev. B* **45**, 33 (1992).
- [5] P. W. Anderson, *Phys. Rev. Lett.* **17**, 95 (1966).
- [6] J. A. Appelbaum, *Phys. Rev. Lett.* **17**, 91 (1966).
- [7] S. H. Pan, E. W. Hudson, K. M. Lang, H. Eisaki, S. Uchida, and J. C. Davis, *Nature* **403**, 746 (2000).
- [8] H. Kashiwaya, A. Sawa, S. Kashiwaya, H. Yamasaki, M. Koyanagi, I. Kurosawa, Y. Tanaka, and I. Iguchi, *Physica C* **357-360**, 1610 (2001).
- [9] H. Kashiwaya, A. Sawa, S. Kashiwaya, I. Kurosawa, N. Yoshida, and Y. Tanaka, *Physica C* **329-333**, 1348 (2003).

Single Charging Effects in (Ferromagnetic) Metallic Nanostructures

Jürgen Schuler, Heribert Knoglinger, Christian Probst, Josef Höß, Thomas Brenninger, Karl Neumaier, Achim Marx, and Rudolf Gross

The steady reduction of the lateral dimensions in the field of solid state electronics entails the demand to take into account and to utilize quantum effects and quantization phenomena. It is evident that, apart from possible new applications, such devices offer a new approach to very interesting physics.

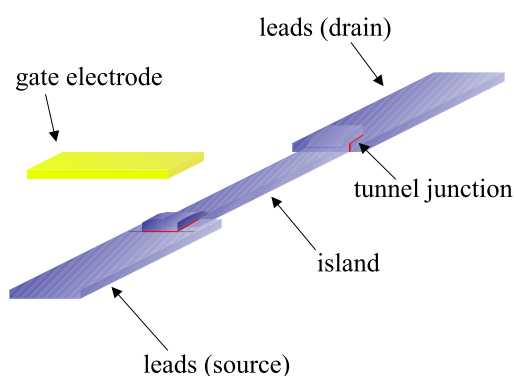


Figure 1: Sketch of a single electron transistor (SET) based on metallic materials.

A very well known system, which uses the discreteness of the electric charge, is the *Single Electron Transistor* (SET), which is schematically shown in Fig. 1. The SET consists in its simplest form of two tunnel junctions in series between normal conducting leads. As the region between the two tunnel junctions is only weakly connected to the rest of the electrical circuit, it is usually referred to as the *island* of the SET. As only one electron as a whole, or more generally speaking a quasi-particle, can pass the tunnel junction, the number of excess quasi-particles on the island n is an integer number, where $n > 0$ and $n < 0$ indicate excess and missing quasi-particles on the island, respectively. On the other hand, as long as no tunneling event takes place a tunnel junction is also a small capacitor. By applying a voltage the free

charge carriers can be moved as a whole with respect to the positively charged background leading to a continuous charging of the two tunnel junctions. Additionally, the island is capacitively coupled to a gate electrode, so that the chemical potential of the island can also be continuously shifted. It is this interplay of the discreteness of charge on the island and the continuous charging of the two tunnel junctions and the gate capacity, which leads to the interesting *single charging effects*.

By applying a transport voltage V_{SD} to the SET, which is in analogy to semiconducting transistors called *source-drain voltage*, the current I through the SET can be drastically influenced and, hence, controlled by applying a voltage V_G to the gate electrode of the SET. Under suitable conditions at low V_{SD} can even be completely blocked by changing V_G the current, a phenomenon called *Coulomb blockade*. At higher voltages by varying V_G the conductance of the SET can be periodically modulated with the period e/C_G , where C_G is the capacitance of the gate, which crucially depends on the distance between the gate electrode and the island. These periodic modulations are called *Coulomb oscillations*. Utilizing the Coulomb oscillations SETs are very often used as extremely sensitive electrometers.

To be able to observe single charging effects, the underlying energy scale for single charging effects, the Coulomb energy E_C , has to meet the condition $E_C = e^2/C_\Sigma \gg k_B T$, where C_Σ is the overall capacitance of the SET, k_B Boltzmann's constant and T the temperature. For an Al/AlO_x/Al-tunnel junction with a total capacitance of 1 fF, the Coulomb energy corresponds to a temperature of about 1 K. Therefore, it is vital to investigate the SETs at temperatures in the mK regime.

The normal conducting SET can be very well described in terms of the *orthodox theory* as long as the tunnelling resistance of the two tunnel junctions are large compared to the quantum resistance R_K , i.e. $R_1, R_2 \gg R_K = h/e^2$ [1]. The orthodox theory is based on time-dependent first order perturbation theory (Fermi's Golden Rule) to calculate the tunnelling rates. To compare our measurements with theoretical predictions we have implemented the orthodox theory for normal conducting SETs as a C++ programme.

Apart from the standard normal conducting SETs, there is a great variety of SET-like structures. Many of them consist of a single material only, in most cases of Al. Some are usually operated in magnetic fields

to quench superconductivity, e.g. the single electron pumps and single electron turnstiles, but there are also devices, where superconductivity is a prerequisite, e.g. charge-qubits [2]. Another interesting field are hybrid SETs, consisting of different materials, in particular ferromagnetic SETs, where the island and/or the leads are made of ferromagnetic metals such as Co or Ni [3]. In these devices the interplay of single charging and magnetoresistive effects can be studied. For instance, the tunnelling rates become spin dependent [4].

Sample Fabrication

We have fabricated several SETs with ferromagnetic islands or leads. The SETs were patterned by electron beam lithography using a two layer resist system, where the bottom layer consists of a 690 nm-thick PMMA/MAA layer, which is covered by a 70 nm-thick top layer of PMMA 950k. This resist system offers a profile with a substantial undercut. The structure is patterned into the top layer, while the PMMA/MAA-layer acts primarily as a spacer, so that the shadow evaporation technique can be applied, where the sample is tilted at different angles during the evaporation process. Not only the SETs but also all leads and bond pads are patterned during this single electron beam lithography step, so that there are no further lithography steps necessary.

The tunnel junctions are fabricated using standard Al/AlO_x-technique. In a first step Al is deposited by electron beam evaporation under an angle of +20°. Afterwards the Al is oxidized forming the tunnel barrier. In the second evaporation step under an angle of -20° Ni is evaporated. After a subsequent lift-off step the wafer is cleaved into chips. Figure 2 shows a typical SET structure. The distance of 250 nm between the gate electrode and the island results in this design in a gate capacitance of around $C_G = 0.08$ fF.

Experimental Setup

The electrical characterization of our devices was performed in a dilution refrigerator. The key component in the experimental setup is a compact current-voltage amplifier, which was built at the WMI this year. Fig. 3 shows a sketch of this amplifier, which has an amplification factor of 10^7 V/A with a resolution of less than 1 pA. The amplifier is built into a small RF-shielded box. All measurements were carried out as 2-terminal measurements, as the resistance of the SETs is much higher than that of the rest of the measurement setup. Apart from the amplifier the RF-shielded box also contained a two-step voltage divider, which reduced the source-drain voltage by 1000:1 and defines the ground potential for the voltage source, so that source and drain of the transistor are at a potential of $+V_{SD}/2$ and $-V_{SD}/2$, respectively.

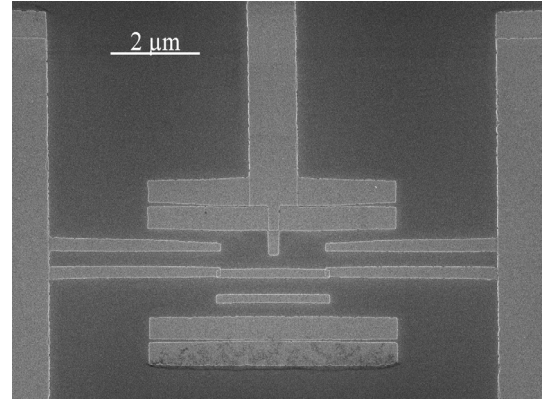


Figure 2: A scanning electron microscopy image of a typical SET structure. The leads and the island are 200 nm wide, the island is 2.5 μm long and the distance between the gate and the island is 250 nm.

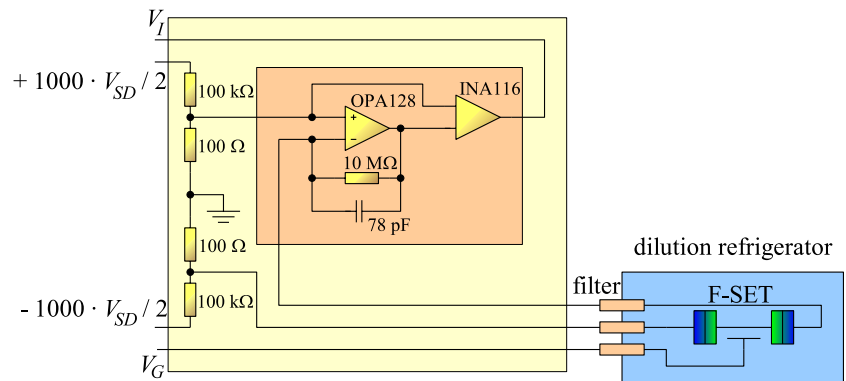


Figure 3: Sketch of the current-voltage amplifier. The light yellow box indicates a small RF-shielded box. The orange box encloses the current-voltage amplifier itself.

Although the samples were ferromagnetic SETs, we will only discuss the normal conducting properties of these devices here. The measurements were performed in a magnetic field of 2 T, which was applied parallel to the island of the SET shown in Fig. 2.

Experimental Results

Fig. 4 shows a direct comparison of two current-voltage characteristics (IVCs) and a simulated IVC, which was obtained using our simulation software. The agreement is only modest, as deviations are clearly visible. The temperature $T_{sim} = 120$ mK, which was used in the simulation differs from the temperature of the sample holder by a factor of 3 ($T_{exp} = 40$ mK). This is most probably due to insufficient microwave filtering of the bias lines in the dilution refrigerator. As microwave photons have an energy of the order of E_C , a single photon can initiate a tunneling process, which would otherwise be blocked. Higher temperatures have a similar effect, an increased T_{sim} compared to T_{exp} is understandable.

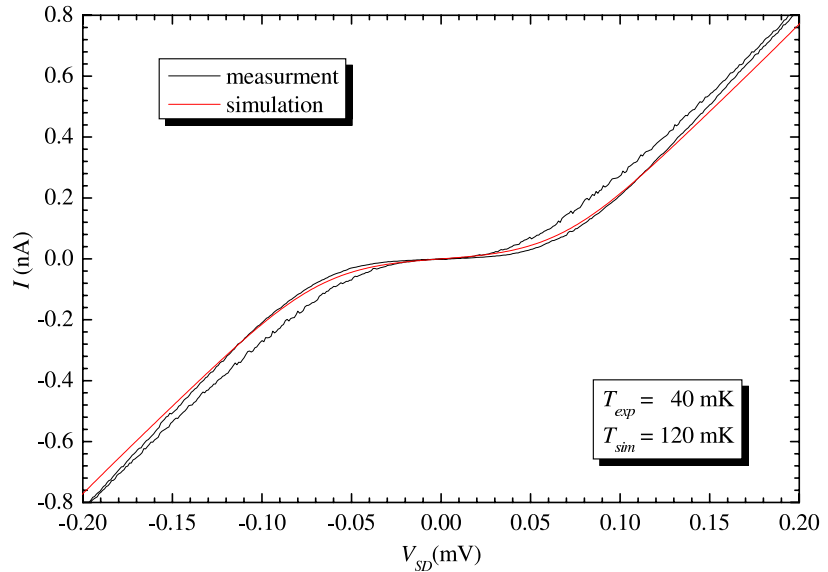


Figure 4: Comparison of measured current-voltage characteristics and simulations. The sample temperature was 40 mK during the experiment. The temperature of the simulation was 120 mK.

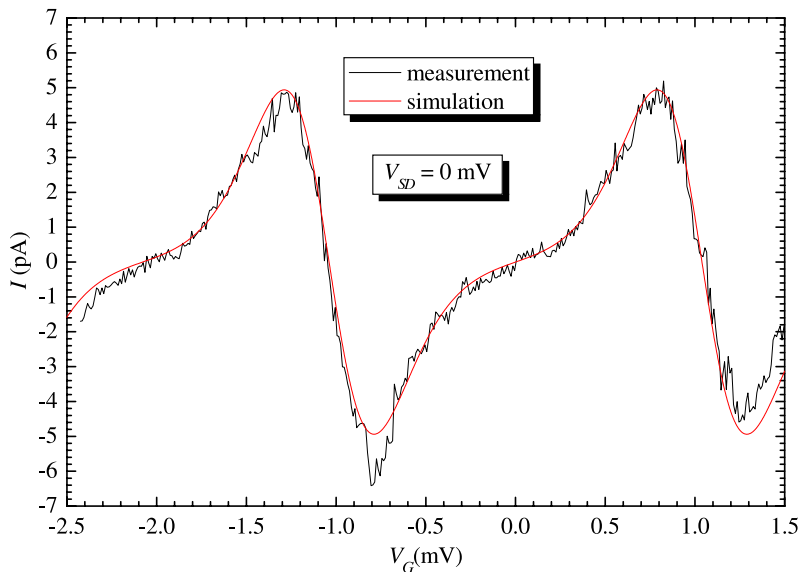


Figure 5: The SET shows a ratchet-like behaviour.

Fig. 5 shows that for vanishing source-drain voltage $V_{SD} = 0$ a finite current I of opposite polarity is measured as a function of the gate voltage V_G . This ratchet-like behavior [5] is of course not included in the orthodox theory, but is due to an asymmetry in the SET, i.e. both the resistances R_1 and R_2 and the capacities C_1 and C_2 of the two tunnel junctions are different, and due to fluctuating potentials.

We have extended our simulation software to include different fluctuating sources with different statistical properties [6]. The simulation shown in

Fig. 5 is based on an asymmetry $R_1 : R_2 = 7 : 3$, a temperature of $T_{sim} = 120$ mK and a ground fluctuation amplitude of $28 \mu\text{V}$. The agreement is very good and gives a strong hint that this device is asymmetric.

For temperatures $T \gg E_C/k_B$, Coulomb oscillations are no longer observable. However, single charging effects still influence the electron transport through the SET. In this high temperature regime the linear conductivity defined as the conductivity at $V_{SD} = 0$ of the SET can be approximated by [7, 8, 9]

$$G_0 \equiv \left. \frac{\partial I}{\partial V_{SD}} \right|_{V_{SD}=0} = \frac{1}{R_1 + R_2} \cdot \left\{ 1 - \frac{E_C}{3k_B T} + \frac{E_C^2}{k_B^2 T^2} \left(\frac{3g\zeta(3)}{2\pi^4} + \frac{1}{15} \right) \right\}, \quad (1)$$

where $g = R_K/R_1 + R_K/R_2$ is the dimensionless parallel conductivity of the SET and ζ is Riemann's zeta function. Fig. 6 shows both the linear conductance G_0 obtained in a temperature series from 40 mK to almost 9 K and the fit according to equation (1). From this fit the asymmetry of the SET $R_1 : R_2 = 7 : 3$ and a Coulomb energy $E_C/k_B = 934$ mK are obtained. The inset of Fig. 6 shows the low temperature regime of the linear conductance G_0 for both the minimal Coulomb blockade (black crosses) and the maximum Coulomb blockade (red symbols). At temperatures lower than 600 mK Coulomb oscillations develop. At the lowest measured temperature of 40 mK the ratio of the linear conductances for the maximum and the minimum Coulomb blockade is $G_0(\text{min. CB}) / G_0(\text{max. CB}) = 16.3$.

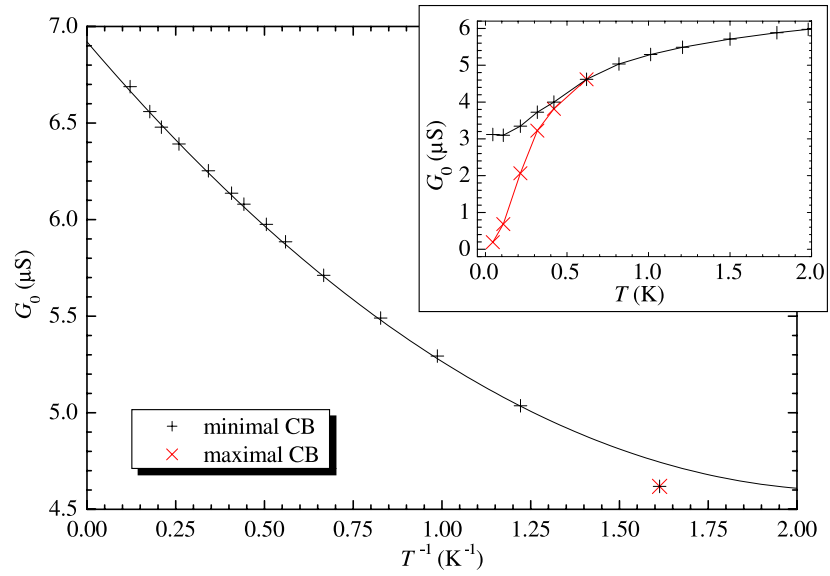


Figure 6: High temperature linear conductance G_0 as defined in equation (1) for both maximal and minimal Coulomb blockade (CB). The inset shows G_0 in the low temperature regime.

References

- [1] G. L. Ingold and Y. V. Nazarov, *Charge Tunneling Rates in Ultrasmall Junctions in Single Charge Tunneling – Coulomb Blockade Phenomena in Nanostructures* edited by H. Grabert and M. H. Devoret. NATO ASI Series B: Physics Vol. 294, pp. 21 – 108 (Plenum Press, New York, 1992)
- [2] Y. Nakamura, Y. A. Pashkin, and J. S. Tsai, *Nature* **198**, 786 (1999)
- [3] C. D. Chen, W. Kuo, D. S. Chung, J. H. Shyu, and C. S. Wu, *Phys. Rev. Lett.* **88**, 047004 (2002)
- [4] H. Imamura, Y. Utsumi, and H. Ebisawa, *Phys. Rev. B* **66**, 054503 (2002)
- [5] P. Reimann, *Phys. Rep.* **361**, 57 (2002)
- [6] C. Wallisser, *Einzelelektronentransistoren im Regime kleiner Widerstände*. Dissertation Universität Karlsruhe (TH) (Forschungszentrum Karlsruhe, 2002)
- [7] D. S. Golubev, J. König, H. Schoeller, G. Schön, and A. D. Zaikin, *Phys. Rev. B* **56**, 15782 (1997)
- [8] G. Göppert and H. Grabert, *Phys. Rev. B* **58**, R10155 (1998)
- [9] G. Göppert, B. Hüpfer, and H. Grabert, *Phys. Rev. B* **62**, 9955 (2000)

Room Temperature TMR-effect in Magnetite Based Magnetic Tunnel Junctions

*Daniel Reisinger, Petra Majewski, Mitja Schonecke, Jürgen Schuler, Matthias Opel, Andreas Erb, Lambert Alff, and Rudolf Gross*¹

Recently, the field of spintronics has been developing rapidly. Magnetic random access memory (MRAM) based on magnetic tunnel junctions (MTJs) has been announced by IBM and Infineon to come to the market already in the year 2005. Moreover, very recently a new programmable logic has been proposed by A. Ney and colleagues [1]. However, up to now a real half-metallic materials with a full spin polarization of the charge carriers at the Fermi level at room temperature is still missing. Such materials are a prerequisite for optimum spintronic device properties. At present, mostly classical magnetic materials such as Fe, Co, Ni and alloys of them are used, which reach only a maximum spin polarization of about 50%. Promising candidates for half-metallic behavior at room temperature are various transition metal oxides such as the doped manganites, the double perovskites, or magnetite as well as intermetallics such as the Heusler compounds.

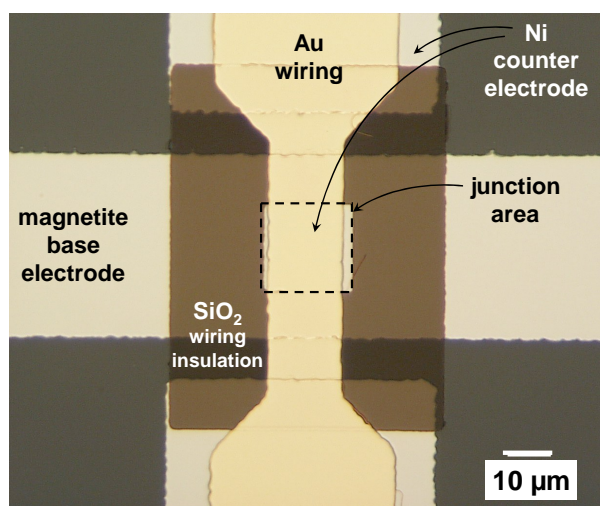


Figure 1: Optical micrograph of a $20 \times 20 \mu\text{m}^2$ magnetite/barrier/Ni magnetic tunnel junction.

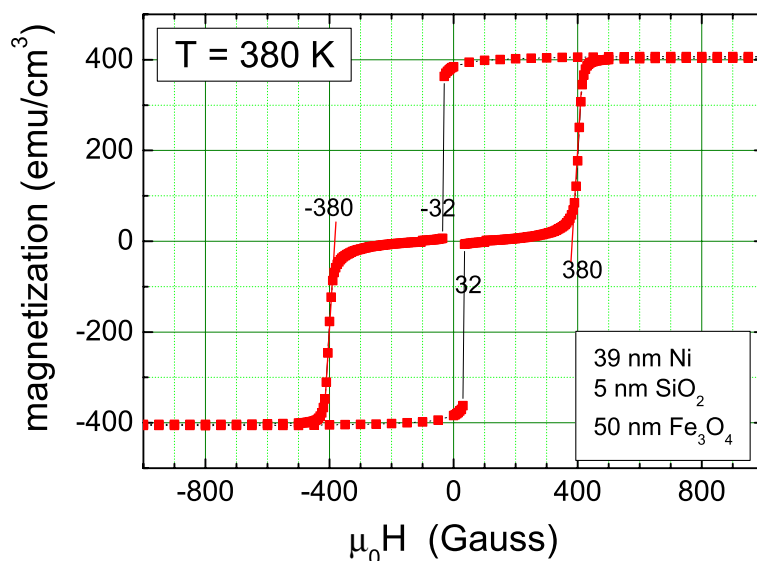


Figure 2: Magnetization versus applied field curves of a 50 nm Fe_3O_4 / 5 nm SiO_2 / 39 nm Ni trilayer film.

Magnetite (Fe_3O_4) is a particularly interesting material for spintronics, because it has a high Curie temperature above 800 K and has been predicted to be a half-metal with full spin polarization [2]. Recently, photoemission spectroscopy of magnetite thin films has shown a spin polarization of up to 80 % at room temperature [3]. However, so far it is not clear whether or not the values of the spin polarization obtained in a photoemission experiment are relevant to magnetic tunnel junctions (MTJs) involving complex interface between magnetic and nonmagnetic materials. In general, in view of spin

¹This work is supported by the BMBF.

transport in MTJs important questions concerning the role of interfaces between different materials, the influence of the tunnelling barrier, as well as the magnetic coupling are not clear at the moment.

We have prepared magnetic tunnel junctions based on epitaxial magnetite thin films as the bottom and Ni as the counter electrode on (001) MgO single crystal substrates. As tunnelling barrier the five materials MgO, SrTiO₃, NdGaO₃, SiO₂, and Al₂O_{3-x} have been tested. The thin film heterostructures have been prepared by pulsed laser deposition (magnetite, barrier layer) and electron beam evaporation (Ni) in an ultra high vacuum system [4, 5]. The thin film growth has to be done in a very well controlled way, because the tunnel barrier is only a few nanometer thick and pinholes have to be avoided. To improve the surface quality of the thin films a new zoom optics for the pulsed laser deposition system was developed. Into the completed thin film multilayers we have patterned tunnel junctions with areas ranging from $10 \times 10 \mu\text{m}^2$ to $20 \times 40 \mu\text{m}^2$ using optical lithography and ion beam etching (see figure 1). Even though the process contains 35 critical steps, after careful optimization we got a yield of working tunnel contacts of about 50%.

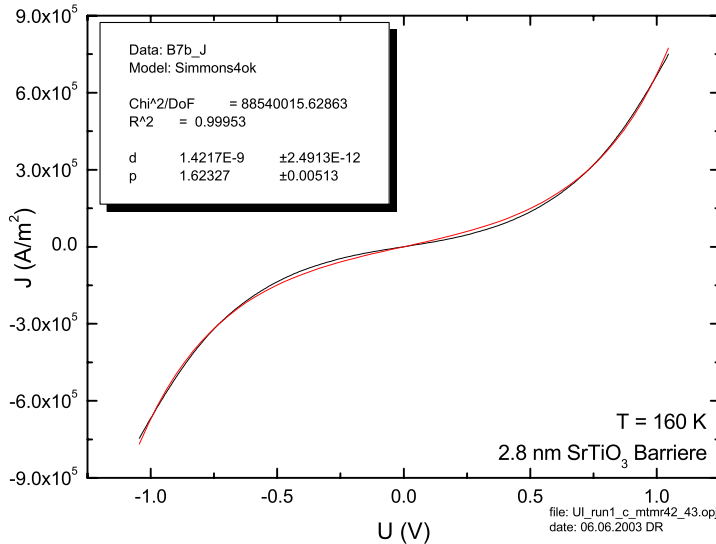


Figure 3: Current-voltage characteristics of a $20 \times 20 \mu\text{m}^2$ magnetite based MTJ with a 2.8 nm thick SrTiO₃ tunnelling barrier at 160 K. The red curve is a fit based on the Simmons model [6].

shows that the two magnetic layers are switch separately and are not coupled across the thin tunnel barrier e.g. via pinholes. This is a crucial prerequisite for the observation of the tunnelling magnetoresistance effect (TMR), because the maximum effect is measured between the parallel and antiparallel magnetic configuration of the junction electrodes.

By measuring the resistance versus temperature, $R(T)$, and current versus voltage, $I(V)$, characteristics of the MTJs, the properties of the tunnel barrier have been determined. Fig. 3 shows the IVC of a MTJ with an area of $20 \times 20 \mu\text{m}^2$ and a SrTiO₃ barrier thickness of 2.8 nm at 160 K. Clearly, a nonlinear IVC is visible. Fitting the measured IVCs to Simmons model [6] we can give a rough estimate for the barrier height and width. The derive values of 1.62 eV and 1.4 nm are reasonable. The IVCs were found to become more and more linear with increasing temperature for all different barrier materials. Together with the decrease of the tunnelling resistance with increasing temperature this is an indication of thermal activated defect states in the tunnel barrier giving rise to a certain amount of inelastic tunnelling current. They could be caused for example by oxygen vacancies in the oxide barrier materials.

The magnetic properties, in particular the coupling between the two ferromagnetic layers in the multilayer structure, have been investigated using a SQUID magnetometer. The coupling between the electrode layers turned out to be strongly dependent on the material used for the tunnelling barrier. Fig. 2 shows the magnetization versus the applied magnetic field, $M(H)$, curve of a magnetic multilayer with magnetite and Ni as the bottom and counter electrodes separated by a 5 nm thick SiO₂ tunnelling barrier. Clearly, in this sample the switching of the two ferromagnetic electrodes layers is visible at the two different coercive fields of about 2 mT for Ni and 38 mT for Fe₃O₄. This

The resistance versus applied magnetic field curves showed a reproducible TMR effect with a symmetrical, nearly ideal switching behavior (see Fig. 4). At room temperature a maximum TMR effect of up to 5% was observed. Compared to values reported in literature this value is large, however, it is still much smaller than the value theoretically expected from the Jullière model for an ideal magnetite/Ni MTJ [7]. A careful analysis of the temperature dependence of the TMR effect revealed that this reduction of the TMR effect was partially caused by a series resistance in the investigated junction geometry. Moreover, tunnelling through defect states in the barrier may be responsible for a further reduction of the measured TMR effect. To determine the spin polarization of the magnetite electrode at room temperature further more detailed experiments with an improved tunnel junction geometry are planned.

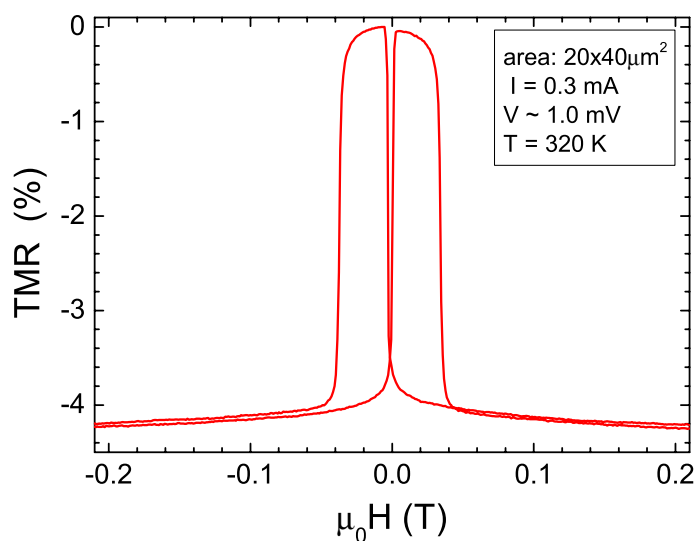


Figure 4: Room temperature TMR effect plotted versus the applied magnetic field for a MTJ with an area of $20 \times 40 \mu\text{m}^2$ and a 2.5 nm thick $\text{Al}_2\text{O}_{3-x}$ barrier.

References

- [1] A. Ney, C. Pampuch, R. Koch, and K. H. Ploog, *Nature* **425**, 485 (2003).
- [2] Z. Zhang, and S. Satpathy, *Phys. Rev. B* **44**, 13319 (1991).
- [3] Y. S. Dedkov, U. Ruediger, and G. Guentherodt, *Phys. Rev. B* **65**, 064417 (2002).
- [4] D. Reisinger, B. Blass, J. Klein, J. B. Philipp, M. Schonecke, A. Erb, L. Alff, and R. Gross, *Appl. Phys. A* **77**, 619 (2003).
- [5] D. Reisinger, M. Schonecke, T. Brenninger, M. Opel, A. Erb, L. Alff, and R. Gross, *J. Appl. Phys.* **94**, 1857 (2003).
- [6] J. G. Simmons, *J. Appl. Phys.* **34**, 1793 (1963).
- [7] M. Jullière, *Phys. Lett. A* **54**, 225 (1975).

Diffusion and Segregation Effects in Doped Manganite/Titanate Heterostructures

Jürgen Simon^a, Jürgen Klein, Daniel Reisinger, Thomas Walther^a, Werner Mader^a, and Rudolf Gross¹

^a Institute for Anorganic Chemistry, University of Bonn, Germany

At present, magnetic tunnel junctions (MTJs) are studied intensively due to their potential application in nonvolatile magnetic random access memory devices [1, 2]. So far, MTJs are mostly based on transition metals with spin polarization $P \leq 50\%$. Since larger P can result in larger values of the tunnelling magnetoresistance (TMR) and, hence, better device performance, MTJs based on half-metallic materials ($P = 100\%$) such as Fe_3O_4 , CrO_2 , the doped manganites of composition $\text{La}_x\text{D}_{1-x}\text{MnO}_3$ (with $D = \text{Ca}$, Sr , and Ba) [3, 4], and the double perovskites like $\text{Sr}_2\text{FeMoO}_6$ [5] or Sr_2CrWO_6 [7] are of great interest. However, it became clear early that the achievable TMR values are not only determined by the bulk spin polarization, as is assumed in the most simple theoretical models [8], but also sensitively depend on the electronic and structural properties of the insulating tunnelling barrier as well as the insulator/ferromagnet interface. It is evident that methods for the experimental determination of the exact interface structure are required in order to be able to correlate electronic and structural properties. Here, we present a transmission electron microscopy (TEM) study of the interface properties of a SrTiO_3 (STO) barrier sandwiched between two ferromagnetic electrodes of doped manganites with different alkaline earth ions D ($\text{La}_{2/3}\text{Ba}_{1/3}\text{MnO}_3$ (LBMO) and $\text{La}_{2/3}\text{Ca}_{1/3}\text{MnO}_3$ (LCMO)).

The MTJs were fabricated as follows [11]: All layers were deposited from stoichiometric targets by pulsed laser deposition at a deposition temperature of 780°C on STO substrates treated in a buffered HF solution. The oxygen pressure was about 200 mTorr, the laser energy density about 2 J/cm^2 , and the laser pulse repetition rate 2 Hz. The lattice mismatch of the manganite films and STO ($a_{\text{bulk}} = 3.905 \text{ \AA}$) is different for the Ca and Ba doped films. While negligible compressive strain of $+0.13\%$ is present for LBMO ($c_{\text{bulk}} = 3.910 \text{ \AA}$), there is large tensile strain of -1.05% for LCMO ($a_{\text{bulk,pseudocubic}} = 3.864 \text{ \AA}$). We note that the complete heteroepitaxial trilayer structure is coherently strained. The STO barrier had a nominal thickness of 8 resp. 7 unit cells in the LCMO resp. LBMO structure. In-situ RHEED was used to monitor the layer-by-layer growth of the structure [12].

TEM specimens were prepared in cross-section by gluing two layered structures "face to face" and subsequent mechanical thinning and finally ion beam milling to perforation. As an example the LCMO/STO/LCMO layered structure is imaged with high resolution in Fig. 1. The STO barrier thickness was determined by counting the (001) lattice fringes which yields a thickness of five perovskite unit cells, equivalent to 2.0 nm. This value is smaller than the nominal value of 8 unit cells as determined from RHEED oscillations during film growth.

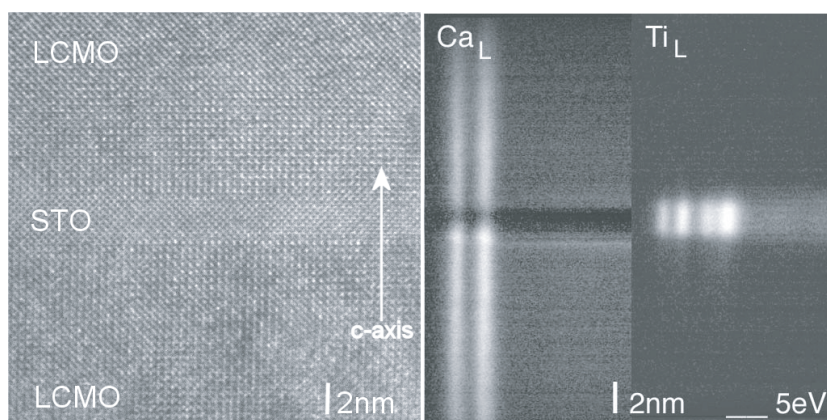


Figure 1: Left: High-resolution TEM (HRTEM) image of a LCMO/STO/LCMO structure. Right: Background subtracted spectroscopic images of the same structure using the Ca_L -edge and the Ti_L -edge.

¹This work is supported in part by the Deutsche Forschungsgemeinschaft and the BMBF (13N8279).

Using a field emission transmission electron microscope (FEG-TEM) equipped with an electron energy imaging filter, we have analyzed the MTJ structures by energy-loss spectroscopic profiling (ELSP) [13]. With the energy filter it is possible to record spectroscopic images that contain a series of electron energy loss (EEL) spectra acquired simultaneously as a function of a spatial co-ordinate. This means that each line of the image basically includes one EEL spectrum. In the experiment we acquired ELSP for each element of interest, which is realized by adjusting the high voltage offset of the microscope to the corresponding ionization energy. Because of the unfavorable ionization energies of Sr, it was not possible to perform ELSP for that element. To improve the signal-to-noise ratio we have acquired 10 spectroscopic images at exposure times of 10 s for each element of interest. Each of the images recorded was deconvoluted by the detector point spread function, then the images from one edge were cross-correlated and summed (see Fig. 1, right). Finally, a chemical profile along the spatial co-ordinate was extracted line by line. The signal-to-noise ratio was improved by integration over an energy range of $\Delta E = 20$ eV from the edge onset. This interval is small enough to neglect the effect of chromatic blurring.

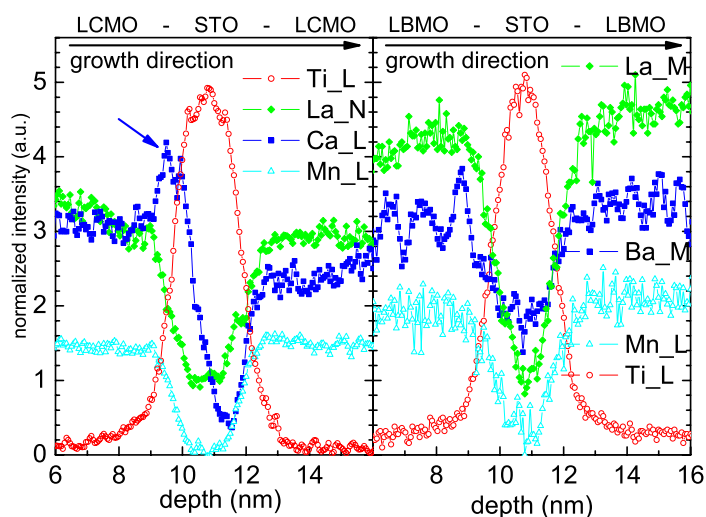


Figure 2: Left: Profiles of Ti, La, Ca, and Mn in the LCMO/STO/LCMO trilayer structure. Right: Profiles of Ti, La, Ba, and Mn in the LBMO/STO/LBMO trilayer.

the interface between the LCMO base electrode and the STO barrier may be interpreted as consisting of a Ca rich LCMO and one unit cell of $(\text{Sr,Ca})\text{TiO}_3$. The chemical thickness of the STO barrier layer measured by the full width at half maximum (FWHM) is 2.0 nm, corresponding to five unit cells of STO. The missing unit cells compared to the nominal thickness of 8 unit cells determined by RHEED are contained in the interface structure at both sides of the barrier. This agrees well with the structural thickness measured from the HRTEM image.

The profiles of the elements Ba, La, Mn and Ti measured for the LBMO/STO/LBMO trilayer are shown in Fig. 2 (right image). Here, the increase of the Ti signal coincides with the decrease of the Ba, La and Mn signals. The profiles appear symmetric with respect to the center of the STO barrier, without any indication for segregation. Despite the poor signal-to-noise ratio a segregation of elements would have been detected. The STO barrier thickness derived from the FWHM of the Ti signal amounts to 2.1 nm and, hence, also is less than the nominal thickness of 7 unit cells.

Another interesting point concerns the Ba signal which does not vanish in the STO layer but only drops by around 30% relative to the LBMO layer. In order to interpret this observation we discuss the relation of the signals in Fig. 2 to the concentration profiles. We first note that the Ba_M core loss energies lie

Fig. 2 (left image) shows the profiles of Ca, La, Mn and Ti measured for the LCMO/STO/LCMO device. As expected the Ti signal strongly increases at the STO interlayer, whereas the signals for La, Mn and Ca strongly decrease. In particular, the Mn signal is completely absent in the center of the 2 nm wide STO barrier region, indicating negligible Mn diffusion. The observed increase of the Ca signal at the interface between the LCMO base electrode and the STO barrier is remarkable (marked by an arrow in Fig. 2). Evidently, there is Ca segregation within the top two unit cells during the growth of the LCMO base electrode. Together with the Ti and Mn profiles the

between those of the Mn_L and La_M edges. As the acquisition time was similar, the spatial resolution of the technique is similar for these edges. Hence, neither differences in delocalisation of inelastic scattering nor drift can be responsible for the different appearance of these profiles. Therefore, our experimental results clearly indicate a remarkably high Ba concentration in the STO barrier layer. The result of simulating the Ba signal in Fig. 2 by fitting Gaussian profiles to it was that Ba diffuses around 1.6 nm into the 2.0 nm thick STO layer from both sides. Although we cannot perform such a fit for the Ca signal due to its asymmetric shape, the non-vanishing Ca signal in the center of the barrier indicates a slightly smaller decay length for Ca segregation. These diffusion effects have to be taken into account in discussing the properties of the STO barrier. Although the data in Fig. 2 also suggest significant La diffusion, the interpretation of the unambiguous La signal is difficult since different effects contribute to the broadening of the signal.

In Fig. 3 we show a secondary ion mass spectroscopy (SIMS) profile [14] for a MTJ based on LBMO electrodes with a two unit cells thick STO barrier layer for comparison. The data is spatially averaged over an area of $500 \times 500 \mu m^2$. Although the Ba signal has the worst signal-to-noise ratio, the Ba diffusion into the barrier can be verified by the loss of Ba in the LBMO electrode in the vicinity of the STO barrier. Note that SIMS also provides information down to the nanometer level of the interface properties in oxide heterostructures, but lacks the spatial resolution of TEM.

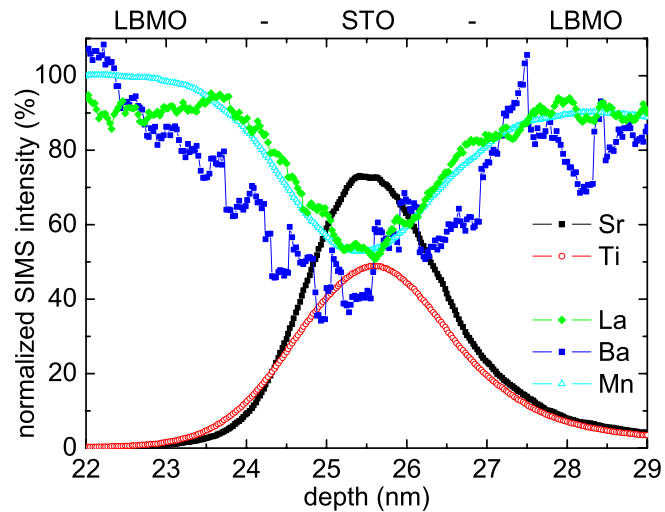


Figure 3: SIMS-profiles of Sr, Ti, La, Ba, and Mn in another LBMO/STO/LBMO trilayer structure. The nominal STO thickness is 2 unit cells.

The different behavior of Ca and Ba can be understood by considering the different ionic radii and the different lattice mismatches of the LBMO and LCMO layers with respect to STO. First, due to the similar ionic radii of Ca^{2+} (1.34 Å) and La^{3+} ions (1.36 Å) for twelve-fold coordination, site-swapping is easily possible. Second, the lattice mismatch between the LCMO layer and STO barrier is large (-1.05%). During nucleation of the epitaxial LCMO film the large tensile coherency strain can be partly accommodated by the LCMO film by incorporating less Ca and/or Ca/La site swapping, thereby forming a Ca rich surface layer. During growth of the LCMO base electrode this Ca rich surface layer is swimming on the film surface and finally results in a Ca rich interface layer between the LCMO base electrode and the STO barrier. Correspondingly, a Ca deficient LCMO layer is expected at the interface between the STO barrier and the LCMO top electrode, in agreement with our observation. Both Ca rich and deficient layers are expected to have strongly reduced Curie temperatures (magnetically dead layers) or may even be antiferromagnetic. Therefore, strongly reduced TMR values are expected for the LCMO/STO/LCMO MTJs grown on STO. In TMR junctions with LCMO electrodes but without STO barrier, high effects can be obtained, as has been shown for example in grain boundary junctions [6]. Also using a well lattice matched $NdGaO_3$ substrate and barrier layer, there is no reason for the formation of Ca rich and deficient interface layers and large TMR values can be observed [15]. For the LBMO based MTJs the situation is different. First, the ionic radius of Ba^{2+} in twelve-fold co-ordination is much larger (1.61 Å) than that of La^{3+} . Therefore, the site-swapping has a higher energy barrier. Second, the good lattice match

to STO (+0.13%) does not require strain accommodation by changing the Ba stoichiometry in the film. As a consequence, the film will grow at the nominal stoichiometry up to the surface. Again, high TMR values should be achievable. We also note that the mechanism described here can lead to a gradient in the oxygen content which in principle can also be studied by TEM [16].

In summary, TEM was used to study local stoichiometry variations in oxide heterostructures. We have shown that interfaces in oxide heterostructures are strongly influenced by both strain effects and ionic radii of the involved ions. In doped manganites, cation segregation was found to take place in order to accommodate epitaxial coherency strain. As a consequence, non-stoichiometric interface layers are formed at the interface to the tunneling barrier which are expected to strongly affect the achievable TMR values of MTJs. In well lattice matched systems like LBMO/STO this problem is avoided and only diffusion processes lead to a small change of the local stoichiometry.

References

- [1] J. S. Moodera and G. Mathon, *J. Magn. Magn. Mater.* **200**, 248 (1999).
- [2] S. S. P. Parkin *et al.*, *J. Appl. Phys.* **85**, 5828 (1999).
- [3] R. von Helmholt, J. Wecker, B. Holzapfel, L. Schultz, and K. Samwer, *Phys. Rev. Lett.* **71**, 2331 (1993).
- [4] J.-H. Park *et al.*, *Nature* **392**, 794 (1998).
- [5] K.-I. Kobayashi, T. Kimura, H. Sawada, K. Terakura, and Y. Tokura, *Nature* **395**, 677 (1998).
- [6] J. B. Philipp, C. Höfener, S. Thienhaus, J. Klein, L. Alff, and R. Gross, *Phys. Rev B* **62**, R9248 (2000).
- [7] J. B. Philipp *et al.*, *Appl. Phys. Lett.* **79**, 3654 (2001).
- [8] M. Jullière, *Phys. Lett. A* **54**, 225 (1975).
- [9] J. M. De Teresa *et al.*, *Science* **286** 507 (1999).
- [10] I. I. Oleinik, E. Y. Tsybal, and D. G. Pettifor, *Phys. Rev. B* **65**, R020401 (2001).
- [11] J. Klein, J. B. Philipp, D. Reisinger, L. Alff, and R. Gross, *phys. stat. sol. (a)* **189**, 617 (2002).
- [12] J. Klein, C. Höfener, L. Alff, and R. Gross, *Supercond. Sci. Technol.* **12**, 1023 (1999); see also *J. Magn. Magn. Mater.* **211**, 9 (2000).
- [13] L. Reimer, I. Fromm, P. Hirsch, U. Plate, R. Rennekamp, *Ultramicroscopy* **46**, 335 (1992).
- [14] The SIMS measurements were performed by U. Ehrke and A. Sears (FEI Company, Bruckmannring 40, 85764 Oberschleißheim, Germany).
- [15] Moon-Ho Jo, N. D. Mathur, N. K. Todd, M. G. Blamire, *Phys. Rev B* **61**, R14905 (2000).
- [16] C. L. Jia, M. Lentzen, K. Urban, *Science* **299**, 870 (2003).

Mn-doped ZnO - A Ferromagnetic Semiconductor?

Karl Nielsen, Lambert Alff, Jürgen Simon^a, Thomas Walther^a, Werner Mader^a, and Rudolf Gross¹

^a Institute for Anorganic Chemistry, University of Bonn, Germany

Over the last decade the interest in the new field of spintronics has been growing steadily. On the one hand, this interest was stimulated by the idea to use of the spin degree of freedom of electrons in electronic devices and thereby to enable the development novel spintronics devices with improved or new functionality. On the other hand, there was growing interest in the physics of spin transport in solids in general.

The key problems in the field of spintronics are the generation, the transport, the manipulation and the detection of spins. Furthermore, with respect to applications, room temperature operation of spintronic devices is a key issue. Since our today's electronic devices are mainly based on semiconducting materials, the injection of spins into usually non-magnetic semiconducting materials is a prerequisite for spintronics. Therefore, considerable research effort was focussed on the development of room temperature ferromagnetic semiconductors that can be used for spin injection.

A possible solution is the realization of diluted magnetic semiconductors (DMS) with Curie temperatures above room temperature. In a DMS a certain amount of the semiconductor ions is replaced by magnetic transition metal ions such as manganese (Mn). In this way magnetic moments are introduced into the lattice, which can be coupled ferromagnetically via the conduction electrons/holes in the semiconducting material. According to theory [1], Mn-doped ZnO with a Mn concentration of 5% and a hole concentration of $3.5 \times 10^{20} \text{ cm}^{-3}$ is a promising candidate for room temperature ferromagnetism. The presence of holes is necessary, because other coupling mechanisms, which work without mobile charge carriers such as the superexchange or dipolar interactions are not strong enough to cause ferromagnetism at high temperature [2]. However, the realization of *p*-doping in ZnO is difficult to achieve, because ZnO has a large number of intrinsic defects naturally leading to *n*-doping, which has to be compensated.

We have grown epitaxial Mn (5%) doped ZnO thin films on single crystalline ZnO substrates using pulsed laser deposition (PLD). To find the optimum deposition conditions the films have been deposited at different substrate temperatures and various values for the deposition pressure and atmosphere (see Table 1). The films can be distinguished according to their color. The films of the first series were black, those of the second yellow and those of the third light yellow.

sample series	first	second	third
substrate temperature	200°C	600°C	600°C
deposition pressure	4.8×10^{-3} mbar	5.9×10^{-3} mbar	3.1×10^{-4} mbar
deposition atmosphere	Ar	Ar/O ₂ (99%/1%)	atomic nitrogen
color	black	yellow	light yellow

Table 1: Deposition conditions used for the growth of the three investigated sample series.

In order to avoid clustering of the Mn ions, low substrate temperatures (200°C and 600°C) have been chosen to reduce the mobility of the atoms on the substrate surface. For the third sample series atomic nitrogen, which was produced by a RF atom source, was used as the deposition atmosphere. The nitrogen atoms are highly reactive and are built in into the growing Mn:ZnO film. Theoretically, this should

¹In collaboration with the Institute for Anorganic Chemistry, University of Bonn, and the Walter Schottky Institute, TU Munich.

result in *p*-doping of ZnO. However, measurement of the Hall effect have clearly shown *n*-doping of our samples, which is most likely due to a large density of intrinsic defects. Furthermore, in the Hall effect data no anomalous contribution was observed. The absence of an anomalous Hall effect indicates that there are no intrinsic ferromagnetic coupling in the Mn:ZnO films.

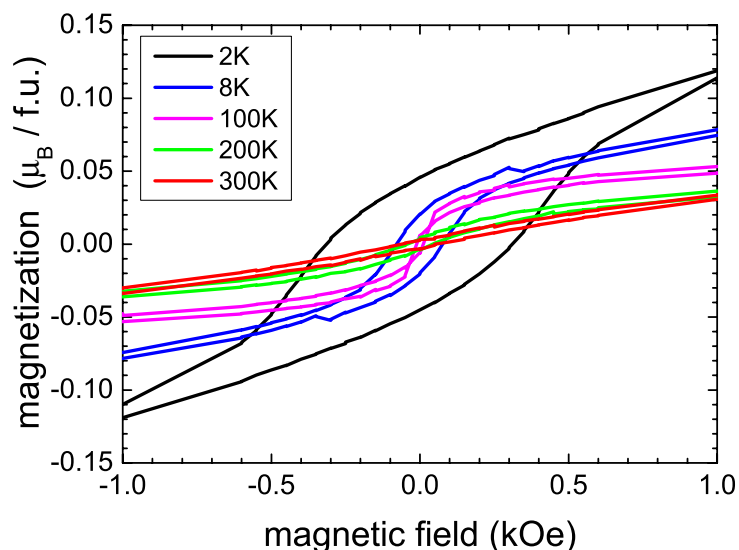


Figure 1: Magnetization curves of a Mn-doped ZnO film measured at different temperatures. The epitaxial films has been prepared in the first samples series

observed hysteresis is related to the defect rich interface layer. For the second and third sample series no ferromagnetism was observed down to 2 K.

In summary, epitaxial Mn-doped ZnO-films were grown on ZnO single crystalline substrates using different deposition conditions. The films of the first sample series showed a magnetic hysteresis at low temperatures, which however may be due to a large defect density at the interface to the substrate. The other samples showed no sign of ferromagnetism. Our attempts to achieve *p*-doping in Mn-doped ZnO by using atomic nitrogen have not been successful so far.

References

- [1] T. Dietl, H. Ohno, F. Matsukara, J. Cibert und D. Ferrand *Science* **287**, 1019 (2000).
- [2] P. Kacman, *Semicon. Sci. Technol.* **16**, R25-R39 (2001).

The magnetic properties of the samples have been measured using a SQUID magnetometer. The Mn:ZnO films of the first sample series show a hysteresis loop below about 90 K suggesting ferromagnetism. At higher temperatures the films behave paramagnetic (see Fig. 1). A transmission electron microscopy analysis of the films revealed a high density of defects at the interface between the epitaxial film and the substrate (see Fig. 2). At present it is not yet clear whether or not this layer with the high defect density is responsible for the observed magnetic hysteresis. However, since no anomalous Hall effect was observed for these films it is tempting to argue that the ob-

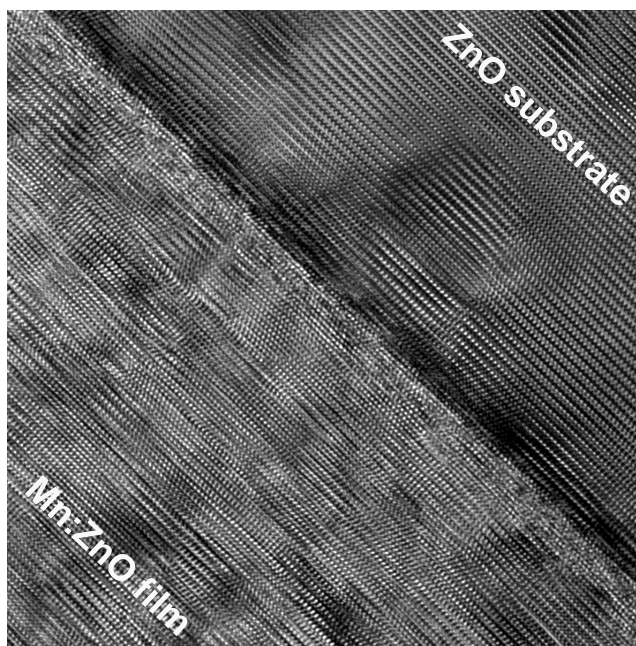


Figure 2: Cross-sectional transmission electron micrograph of an epitaxial Mn-doped ZnO film deposited on a single crystalline ZnO substrate (first sample series).

Hydrogen Control of Ferromagnetism in a Dilute Magnetic Semiconductor

Sebastian T. B. Gönnerwein^a, Thomas A. Wassner^a, Tobias Graf^a, Hans Hübl^a, Jan B. Philipp, Matthias Opel, Rudolf Gross, Achim Köder^b, Wladimir Schoch^b, Andreas Waag^b, and Martin S. Brandt^a ¹

^a Walter Schottky Institut, Technische Universität München, Am Coulombwall 3, 85748 Garching

^b Abteilung Halbleiterphysik, Universität Ulm, 89069 Ulm

Today's microelectronics relies on electronic charges to process and store information. Recently, the advantages of using the electronic spin for such purposes have been realized, and a new class of magneto-electronic or spintronic devices is emerging, such as spin light emitting diodes [1] or spin transistors [2]. Moreover, spintronic devices offer a solid state approach to quantum information processing [3]. Dilute magnetic semiconductors, which combine magnetic ordering with the versatile properties of semiconductors, are possible key ingredients of such devices. A particular benefit of dilute magnetic semiconductors is the possibility to control their ferromagnetic properties by tuning the density of mobile charge carriers. Here, we make use of this tunability in a novel, non-volatile way, using the incorporation of hydrogen to control or pattern the ferromagnetic properties of magnetic semiconductors. Taking $\text{Ga}_{1-x}\text{Mn}_x\text{As}$ as an example, we show that such a hydrogenation electrically passivates the Mn acceptors and removes the holes crucial to the itinerant ferromagnetism [4], and we discuss possible applications of this new approach to the realization of spintronic devices.

The $\text{Ga}_{1-x}\text{Mn}_x\text{As}$ thin films studied were deposited on (100)-oriented, semi-insulating GaAs wafers using low-temperature molecular beam epitaxy. The samples were deuterated using a remote DC plasma at a pressure of 0.3 mbar for 168 h [5]. During the plasma process, the samples were heated to 170°C, well below the growth temperature of 250°C. Deuterium was chosen as the hydrogen isotope in this study due to its lower natural abundance which allows background-free chemical analyses. Here, we will focus on one particular sample, which consists of a 300 nm thick, undoped GaAs high-temperature buffer grown at $T = 585^\circ\text{C}$, followed by a 200 nm thick, undoped GaAs low-temperature buffer layer and the 320 nm thick $\text{Ga}_{0.963}\text{Mn}_{0.037}\text{As}$ layer, both deposited at $T = 250^\circ\text{C}$.

Deuterium incorporation at this concentration drastically changes the magnetic properties of $\text{Ga}_{1-x}\text{Mn}_x\text{As}$ as shown in Fig. 1. In the as-grown films, the magnetization $M(H)$ as a function of the externally applied magnetic field H exhibits a hysteresis loop characteristic for ferromagnetism below the Curie temperature T_C , which is about 70 K for $x = 0.037$. In contrast, the ferromagnetism completely vanishes in the deuterated samples and is replaced by a paramagnetic magnetization behavior, as shown in the inset of Fig. 1.

The effect of hydrogen on nonmagnetic semiconductors has been studied extensively. It has been found that hydrogen or deuterium form complexes with many defects and dopants, and thereby passivate their electronic properties. Indeed, our investigation of the electronic properties indicates that such electrically inactive complexes are also formed upon the deuteration of Ga. In the as-grown sample, the metallic conductivity typical for ferromagnetic $\text{Ga}_{1-x}\text{Mn}_x\text{As}$ is found (Fig. 2), with the characteristic conductivity minimum near T_C caused by spin-dependent scattering [6]. Upon deuteration, the low-temperature dark conductivity is reduced by more than 9 orders of magnitude, and at high temperatures, the typical thermally activated behavior of a semiconductor is observed. Room temperature Hall experiments show that the samples are p-type after hydrogenation, with hole concentrations between 5×10^7 and $5 \times 10^{19} \text{ cm}^{-3}$, depending on the exact plasma exposure times.

¹This work was supported by Deutsche Forschungsgemeinschaft (SFB 348).

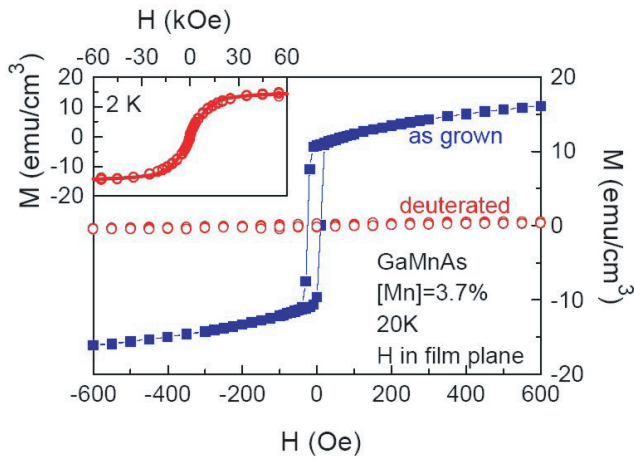


Figure 1: Comparison of the DC magnetization $M(H)$ loops of as-grown $\text{Ga}_{0.963}\text{Mn}_{0.037}\text{As}$ (blue) and after deuteration (red) at $T = 20$ K with the external magnetic field in the plane of the thin film. The ferromagnetic hysteresis present in the as-grown film vanishes after the deuteration. Inset: Magnetization of the deuterated sample at $T = 2$ K and for a much broader range of magnetic fields H . The data are best described by a Brillouin-type magnetization, with $g \approx 2$ and $J = 5/2$ (thick full line) expected for localized Mn atoms with a $3d^5$ configuration (Mn in its oxidation state $2+$).

function for $g \approx 2$ and $J = 5/2$, yielding the thick full line in the inset of Fig. 1.

This can be directly understood from the electron configuration of Mn in GaAs, shown in the inset of Fig. 2 both in the unpassivated and in the deuterated state. In this simple electron counting picture, a pure $3d^5$ configuration with $g \approx 2$ and $J = 5/2$ corresponding to Mn in its oxidation state $2+$ is expected in the latter case [7], in agreement with the magnetization experiments. However, $M_{sat} \approx 15 \text{ emu/cm}^3$ must be assumed in the calculations, which is more than a factor of 2 smaller than $M_{sat} = xN_0g\mu_B J \approx 38 \text{ emu/cm}^3$ expected for the nominal Mn content x determined from XRD, with the density $N_0 = 2.21 \times 10^{22} \text{ cm}^{-3}$ of cation sites in GaAs. Nevertheless, it is important to stress that the saturation magnetization of the as-grown, ferromagnetic film and of the paramagnetic film after deuteration in Fig. 1 are identical within experimental error. Thus, the localized Mn moments are not significantly changed by the deuteration, and the loss of ferro-

Thus, the Mn acceptors can be deuterated essentially, leading to a reduction of the hole density by many orders of magnitude. Therefore, one of the two crucial ingredients for the ferromagnetic properties of $\text{Ga}_{1-x}\text{Mn}_x\text{As}$ films, the charge carrier mediated exchange interaction between the localized Mn magnetic moments, is removed and the ferromagnetism is destroyed. However, the localized Mn magnetic moments should still be present. As shown in the inset of Fig. 1, the magnetization of deuterated $\text{Ga}_{0.963}\text{Mn}_{0.037}\text{As}$ exhibits the paramagnetic, Brillouin-type magnetization $M(H) = M_{sat}B_J(g\mu_B\mu_0 HJ/kT)$ expected in this case. Here, M_{sat} is the saturation magnetization and B_J is the Brillouin function, with the Bohr magneton μ_B , the g -value and the total angular momentum quantum number J of the Mn center, the temperature T , and the Boltzmann constant k . By far the best fit to the experimental data is obtained using the Brillouin

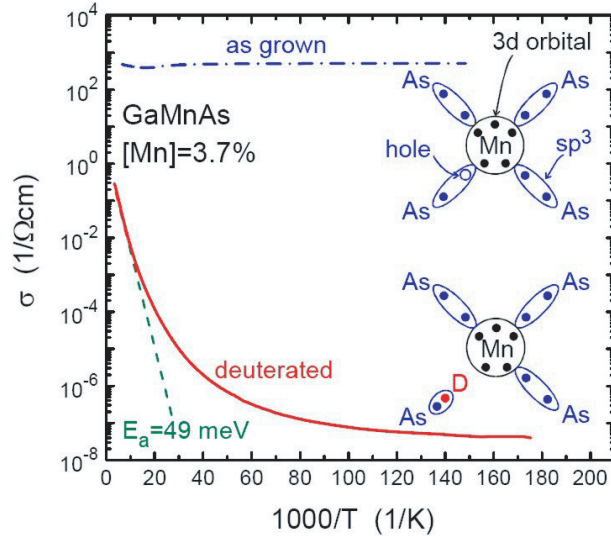


Figure 2: Temperature dependence of the dark conductivity of $\text{Ga}_{0.963}\text{Mn}_{0.037}\text{As}$ before and after deuteration. The as-grown film exhibits a nearly temperature-independent, metallic conductivity (blue). In contrast, deuterated GaMnAs is semiconducting (red), the dark conductivity being activated with $E_a = 49 \text{ meV}$ at high temperatures (green). The insets show an electron-counting picture of the Mn acceptor in GaAs, in which the valence electrons are depicted as full circles in the $4sp^3$ and $3d$ orbitals. Mn incorporated on a substitutional Ga site acts as an acceptor. An electron from the GaAs valence band is thus required to saturate all bonds, resulting in a delocalized hole not shown. Upon deuteration, all bonds are saturated without the need for valence-band electrons. This explains the drastic reduction of the density of free holes and the configuration of Mn after the deuteration.

magnetism can be attributed unambiguously to the effective reduction of the hole concentration.

In summary, we have shown that deuteration changes $\text{Ga}_{1-x}\text{Mn}_x\text{As}$ thin films from a metallic to a semiconducting state and from a ferromagnetic to a paramagnetic state. A controlled incorporation of deuterium or hydrogen, e.g. via a plasma process or by low-energy ion implantation together with appropriate masks or focussed ion beams, should allow to tune the hole density and therefore the magnetic properties, both laterally as well as in the depth of the thin films. In particular, acceptor-hydrogen complexes have been found to dissociate at temperatures well above the growth temperature of $\text{Ga}_{1-x}\text{Mn}_x\text{As}$, so that hydrogen incorporation allows a non-volatile magnetic lithography. This new degree of freedom in the "design" of the electronic and magnetic properties of $\text{Ga}_{1-x}\text{Mn}_x\text{As}$ opens up a number of novel fundamental experiments and device applications. The use of hydrogen to realize ferromagnet/semiconductor/ferromagnet devices represents another intriguing possibility. In contrast to conventional giant magnetoresistance (GMR) or tunnelling magnetoresistance (TMR) devices, which are heterostructures of different materials, hydrogenation allows the formation of such devices from one material only, with the particular benefit of a low density of defects at the interfaces crucial for the performance of such devices.

References

- [1] Fiederling, R., Kelm, M., Reuscher, G., Ossau, W., Schmidt, G., Waag, A., and Molenkamp, L., *Nature* **402**, 787-789 (1999).
- [2] Datta, S. and Das, *Appl. Phys. Lett.* **56**, 665-667 (1990).
- [3] Kane, B. E., *Nature* **393**, 133-137 (1998).
- [4] Dietl, T., Ohno, H., Matsukura, F., Cibert, J. and Ferrand, *Science* **287**, 1019-1022 (2000).
- [5] Stutzmann, M., Chevrier, J., Herrero, C. P., and Breitschwerdt, A., *Applied Physics A* **53**, 47-53 (1991).
- [6] Van Esch, A., Van Bockstal, L., De Boeck, J., Verbanck, G., van Steenberghe, A., Wellmann, P., Grietens, B., Bogaerts, R., Herlach, F., and Borghs, G., *Phys. Rev. B* **56**, 13103-13112 (1997).
- [7] Schneider, J., Kaufmann, U., Wilkening, W., Baeumler, M., and Köhl, *Phys. Rev. Lett.* **59**, 240-243 (1987).

Diffusion Coefficients of Interlayer Water Molecules in Graphite Oxide

Anton Lerf, Alexandra Buchsteiner^a, Jörg Pieper^a, Stephan Schöttl^b, ¹

^a Hahn-Meitner-Institute, Berlin, Germany.

^b National Physics Laboratory, London, UK.

Graphite oxide (GO) has been known and used since the 19th century. Recent interest grew due to proposed application as material for battery electrodes, owing to the possibility of intercalation. Various hydration levels are observed giving rise to different spacing of the carbon layers in the range from 6 Å to 12 Å. Information about the mobility of the water molecules is not yet complete but crucial for the understanding of the structure of the C layers as well as the intercalation process.

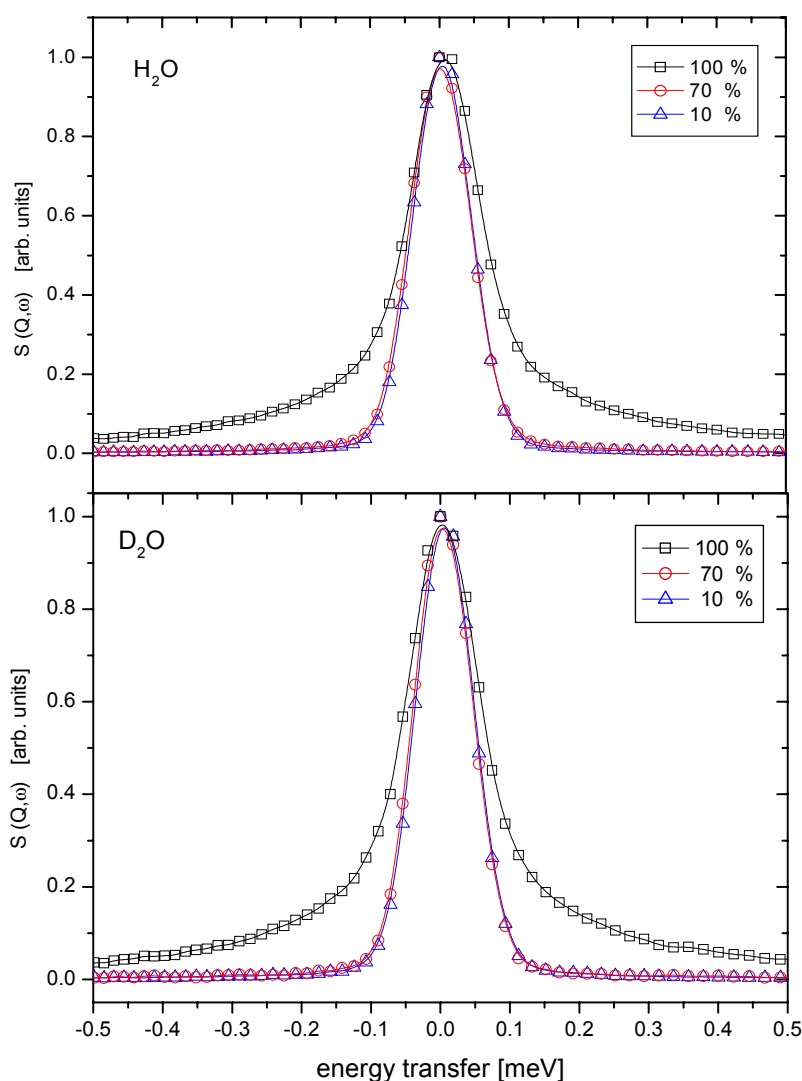


Figure 1: Normalised graphite oxide TOF neutron spectra at a scattering angle of 52°; light water samples in the upper panel; heavy water samples in the upper panel; all hydration levels (10%, 70%, 100%) are shown.

With time-of-flight (TOF) neutron scattering at the spectrometer V3/NEAT diffusion processes for the rotation and translation have been investigated. Three different hydration levels, characterized by the 10%, 70%, and 100% mass of water added per mass (usually 1 g) of dry GO powder, were examined. Both H₂O and D₂O samples were produced. This way contributions from GO and intercalated water can be separated.

Spectra of the six samples were recorded at room temperature with two different energy resolutions of 66 μeV and 100 μeV, and measurement times of 8 to 15 hours, taking advantage of the full available beam time. A preliminary data correction for detector efficiency and sample geometry as well as conversion to $S(Q, \omega)$ could be done on site. The position of the structural Bragg peak depends on hydration and is consistent with x-ray Debye-Scherrer patterns, also taken at HMI. The latter finding proves that the samples can be related

¹This work was supported by the European Union under contract HPRI-CT-2001-02138.

to the above mentioned well-defined hydration degrees and that the hydration level of the corresponding H₂O and D₂O samples was comparable. We found that the layer separation increases nonlinearly with water content. Quasielastic scattering was observed over the whole angle range with clear peaks centered on zero energy transfer. The absolute intensity of the quasielastic contribution to the spectra clearly increases with hydration degree, as expected. Therefore, the spectra promise to be an excellent base for developing models of the water motion.

Fig. 1 shows normalized spectra for all six samples at a scattering angle of 52°. Clearly, the lower water contents (10% and 70%) show similar peak shapes. This means that water added up to 50% has the same properties as water in the almost dry sample. This changes with the 100% sample, where the lower part of the peak broadens substantially. The central part, however, still appears similar to the less hydrated samples. Therefore, a new component of motion must be present for the added water molecules. This component has a shorter time constant, leading to a broader energy distribution.

Superconducting Qubits: Setup for Experimental Characterization

Georg Wild, Heribert Knoglinger, Chiara Coppi, Matteo Mariantoni, Jürgen Schuler, Thomas Brenninger, Wolfgang Hehn, Achim Marx, Christian Probst, and Rudolf Gross ¹

A fundamental new approach to information processing is based on very basic principles from quantum physics. The elementary unit in quantum information processing (QIP) is a two-state quantum system called qubit. Computations are performed by creation of coherent superposition of qubit states and by controlled entanglement of the information on the qubits. Solid state based qubits possibly meet the requirements of scalability and large-scale integration needed for real QIP tasks. Furthermore, in *superconducting* qubits all electrons are condensed in the same macroscopic quantum state which is separated by a gap from the excited quasi-particle states. Due to this gap, the entanglement of the quantum state with quasiparticle states resulting in decoherence is reduced. Hence, the phase coherence time in superconducting qubits is expected to be sufficiently long.

Starting with the new SFB 631 [1] at the WMI the research activities concerning the fabrication and characterization of superconducting phase (flux) qubits have been strongly intensified. Both the experimental prerequisites to characterize superconducting devices and qubits at very low temperatures and the technology to fabricate superconducting flux qubits based on thin aluminum films and Al/Al₂O₃/Al tunnel junctions have been considerably advanced.

Experimental Setup

Any algorithm for quantum computation is based on the *coherent* time evolution of the underlying quantum bits. On one hand this requires sufficiently long intrinsic coherence times but on the other hand one has to ensure that the qubits are thoroughly decoupled from the environment. Therefore, we have developed a hermetically sealed sample stage for the new dilution refrigerator insert (which has been reported on in ref. [2]). All bias lines for electrical transport measurements are filtered with *LCR* low-pass filters at room temperature in a shielded box at the top of the insert and copper-in-powder filters [9] at the base temperature (c.f. Fig. 1) to suppress the coupling of environmental and thermal noise of the resistive elements at higher temperatures through the bias lines. This noise could otherwise enhance the decoherence in the qubit structures. The bias lines are thermally anchored at 4.2 K and at the sample stage base temperature. To avoid heating up the mixing chamber, multifilamentary superconducting Nb wires in a CuNi matrix have



Figure 1: Sample stage attached to the mixing chamber of a ³He/⁴He dilution refrigerator. The bias lines are filtered through copper-in-powder filters. The samples are mounted on a 1" Si-wafer, electrical contacts are established by spring loaded contacts.

¹This work is supported by the Deutsche Forschungsgemeinschaft through SFB 631.

been utilized between 4.2 K and the mixing chamber. To ease the exchange of samples, which are glued to 1" Si-wafers, a contacting scheme based on specially designed spring loaded pins has been developed (c.f. Fig. 1). The contact pins are pressed on gold contact pads sputtered on the Si-wafer. The electrical contact to the samples is established through standard ultrasonic wire bonding. Direct coupling of electromagnetic stray fields to the qubits is eliminated by a silver enclosure. The dilution insert has been tested to run stable for a long time at a base temperature below 25 mK. To provide magnetic shielding the insert is operated in a glass fiber reinforced ("GFK") cryostat with two surrounding μ -metal shields. An additional cryoperm shield surrounds the vacuum can at 4.2 K. The whole setup is situated in a high-frequency shielded room. All the lines of the pumping system and all the electrical lines are carefully fed through the walls of the shielded room.

Fabrication of superconducting devices and qubits

Superconducting flux qubits are based on superconducting loops interrupted by one or more Josephson junctions. The first successfully realized flux qubits depend on a small externally applied magnetic field to generate a defined phase bias in the superconducting ring structure. This flux bias is required to reach a degenerate qubit state [3, 4]. Because of their rather large loop inductance the flux qubits are very susceptible to flux noise resulting in decoherence and a very high precision of the external applied magnetic field is required. To circumvent this problem superconducting flux qubits with intrinsic π -phase bias elements have been suggested. These are expected to be much less susceptible to external noise since the inductance of the superconducting loop can be designed to be very small.

There are several ways to realize intrinsic phase bias elements: phase bias elements using fluxoid quantization in small superconducting loops [5], controllable SNS-Josephson junctions based on conventional superconductors [6], π -junctions based on Josephson junctions between *s*- and *d*-wave superconductors [7] and Josephson junctions with ferromagnetic barriers [8]. The fabrication of these intrinsic phase bias elements is technologically rather challenging. To approach these fabrication problems we have started fabricating individual Josephson junctions, SQUIDS and flux qubit structures based on Al/Al₂O₃/Al technology. Fig. 2 shows a SEM image of a 3-junction flux qubit which is galvanically connected to the readout SQUID [4]. The proper operation of the qubits depends strongly on correctly engineered device parameters. In particular, the thickness of the Al₂O₃ tunnel barriers crucially determines the parameters of the Josephson junctions. Therefore, we are presently optimizing the oxidation parameters to reproducibly fabricate junctions where the Josephson coupling energy is larger than the charging energy by a factor of 50-100. After this optimization procedure of the junctions first flux qubit structures as that shown in Fig. 2 will be tested and thoroughly characterized. In parallel, the more complex fabrication procedures for incorporating intrinsic phase shift elements into the flux qubits will be tackled as the necessary technology is available.

Measurement of escape rates in Josephson junctions

One way to read out flux qubits is to measure the switching of a low-damped SQUID which is coupled to the qubit under investigation out of the zero-voltage state. The current where this switching happens depends on the actual quantum state of the qubit. Since the switching is a statistic process (the switching

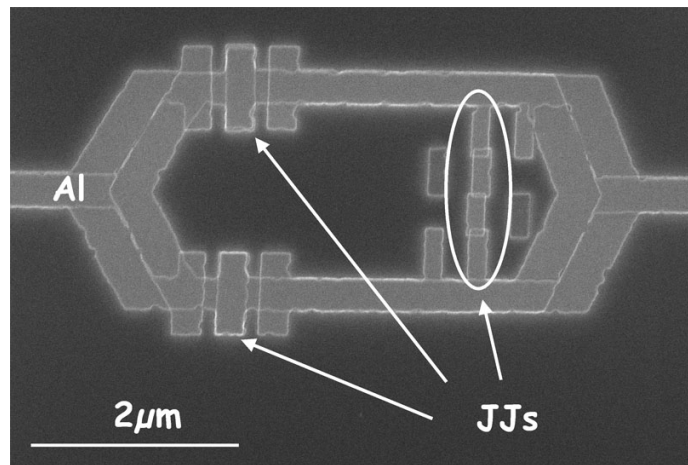


Figure 2: Flux qubit in Chiorescu-design [4]. The 3-junctions and the small loop to the right make up for the qubit which is directly connected to the readout SQUID with two large junctions.

probability out of the zero-voltage state is influenced by thermal fluctuations and quantum tunnelling) and the modification of the flux threading the SQUID by the qubit is small one has to repeat the switching current measurement many times. The resulting switching current histograms can then be used to determine the quantum state of the qubit.

Furthermore, it has been shown that the switching of a single Josephson junction out of the zero-voltage state can be taken as an experimental test for the quantum behavior of a macroscopic degree of freedom, namely the phase difference across a current-biased Josephson junction [9]. The escape rate Γ of a Josephson junction from its zero-voltage state can be determined from switching current histograms. This escape rate shows a crossover from a thermally activated behavior at higher temperatures to a tunnelling type behavior at very low temperature. This crossover is shown in Fig. 3, where the escape temperature T_{esc} (which is determined from Γ) is plotted versus the bath temperature. On the other hand, to observe the temperature dependence of T_{esc} shown in Fig. 3 efficient shielding of the sample from environmental noise is crucial. Thus, measurements of the temperature dependence of escape rates on individual Josephson junctions serve as a very sensitive test bed for the experimental setup. Any deviation from the linear relation $T_{\text{esc}} \simeq T$ at higher temperatures or a crossover to a temperature independent behavior at too high temperatures strongly indicates that external contributions cause a premature switching of the junction.

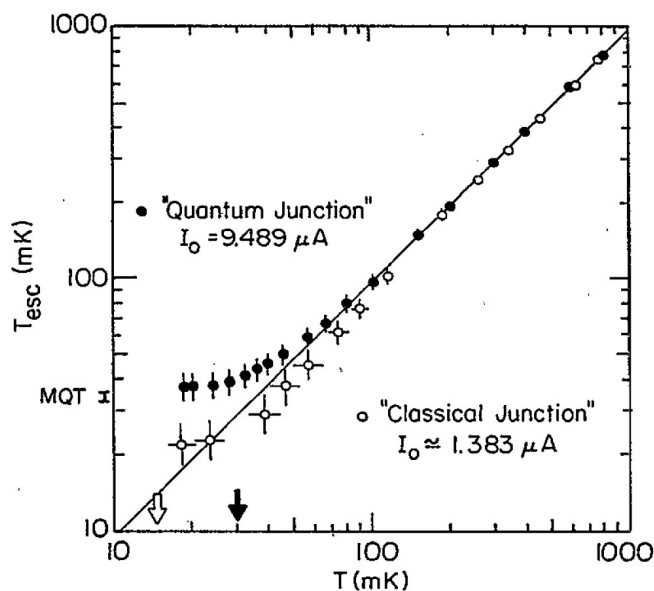


Figure 3: Escape temperature of Nb/Al₂O₃/Pb junction vs temperature determined from switching current histograms [9].

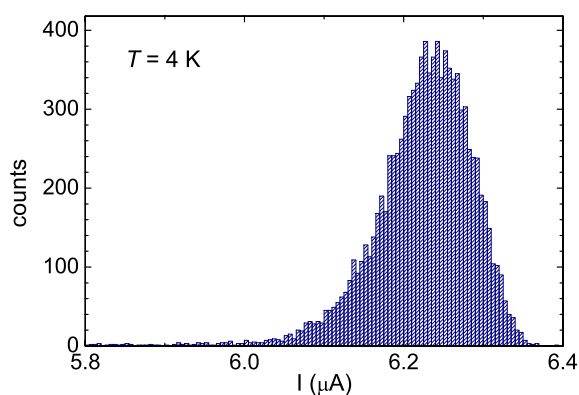


Figure 4: Switching current histogram obtained for a HTS grain boundary Josephson junction at 4.2 K.

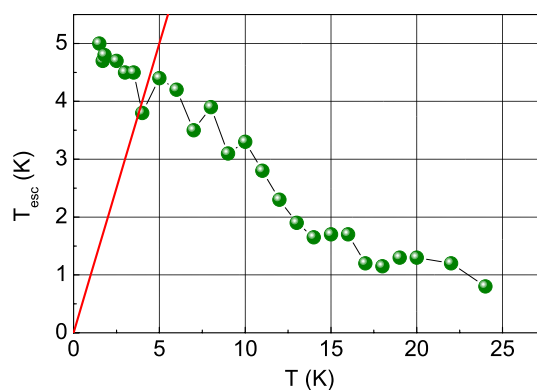


Figure 5: T_{esc} vs bath temperature T for the same junction as in Fig. 4 determined from switching current histograms.

We have established the experimental techniques required for switching current measurements. This setup consists of a special critical current detection electronics and a Labview based software which facilitates the recording of a large number of critical current measurements and performs an immediate evaluation of the histograms and switching rates. This setup has been successfully used in escape rate measurements on high-temperature superconductor (HTS) Josephson junctions. With these HTS grain

boundary junctions (GBJs) we could test the experimental switching current measurement setup over a broad temperature range in a different cryogenic setup while we were able to simultaneously optimize the filters in the new dilution refrigerator insert. Fig. 4 shows a typical switching current histogram measured on a $1\ \mu\text{m}$ wide GBJ at 4.2 K. Clearly, the temperature dependence of T_{esc} shown in Fig. 5 (derived from a number of histograms as in Fig. 4) strongly deviates from the expected behavior which is depicted by the red line. There are at least two reasons for this behavior. First the measurements have been performed in a cryogenic insert where the bias lines are not optimally filtered and thus external noise may significantly enhance the switching especially at low temperatures. Second the dynamics of the GBJs cannot be described within the (“simple”) RCSJ model, since one also has to consider a large external frequency dependent damping which is due to the high kinetic inductance of the superconducting electrodes (c.f. [10]). As has been shown in Ref. [11] such a frequency dependent damping strongly modifies both the junction current voltage characteristics and the temperature dependence of the escape rates. Presently, we have started escape rate measurements on a well characterized Nb/A $\frac{1}{2}$ O $\frac{3}{2}$ /Nb Josephson junction which has been shown to follow nicely the dependence depicted in Fig. 3 [12] in the new dilution refrigerator insert to characterize the filters in this setup. Only if we are able to reproduce the data that have been measured on this junction before we may safely assume that the bias line filtering is sufficient to perform experimental investigations on quantum coherent behavior in qubit structures.

References

- [1] *see* <http://www.wmi.badw-muenchen.de/SFB631/>
- [2] Annual report 2002, Walther-Meissner-Institut, <http://www.wmi.badw.de/ueberuns/jahresberichte/2002.pdf>
- [3] J. E. Mooij, T. P. Orlando, L. S. Levitov, L. Tian, and C. H. van der Wal, S. Lloyd, *Science* **285**, 1036 (1999).
- [4] I. Chiorescu, Y. Nakamura, C. J. P. M. Harmans, and J. E. Mooij, *Science* **299**, 1869 (2003).
- [5] J. B. Majer, J. R. Butcher, and J. E. Mooij, *Appl. Phys. Lett.* **80**, 3638 (2002).
- [6] J. J. A. Baselmans, A. F. Morpurgo, B. J. van Wees, and T. M. Klapwijk, *Science* **397**, 43 (1999).
- [7] L. Ioffe, V. B. Geshkenbein, M. V. Feigel'man, A. L. Fauchière, G. Blatter, *Nature* **398**, 679 (1999).
- [8] A. I. Budzdn et al., *Sov. Phys. JETP* **74**, 124 (1992).
- [9] J. M. Martinis, M. H. Devoret, and J. Clarke, *Phys. Rev. B* **35**, 4682 (1987).
- [10] Annual report 2001, Walther-Meissner-Institut, <http://www.wmi.badw.de/ueberuns/jahresberichte/2001.pdf>, pp. 41.
- [11] D. Vion, M. Götz, P. Joyez, D. Esteve, and M. H. Devoret, *Phys. Rev. Lett.* **77**, 3435 (1997).
- [12] T. Bauch, *priv. communication.*

Epitaxial Growth of Sr_2CrWO_6 Thin Films

Petra Majewski, Jan B. Philipp, Stephan Geprägs, Mitja Schonecke, Matthias Opel, Andreas Erb, Lambert Alff, and Rudolf Gross¹

The double perovskite Sr_2CrWO_6 is an interesting material both due to its rich physics and its interesting properties with respect to applications in spin electronics. A high Curie temperature (up to 458 K for ceramic samples [1]) and a large low field magnetoresistance effects have been found for ceramic samples and thin films of this material [2]. However, the temperature dependence of the resistivity and the magnetotransport properties of Sr_2CrWO_6 are still under debate, since no single crystals are available for this material. On the one hand, for polycrystalline ceramic samples the effect of grain boundaries is masking the intrinsic behavior. On the other hand, for epitaxial Sr_2CrWO_6 thin films without any grain boundaries the intrinsic transport behavior is masked by a parasitic currents through the SrTiO_3 substrate [3]. The insulating SrTiO_3 substrates become (semi-)conducting under the preparation conditions of the thin films (substrate temperatures between 700°C and 840°C, Ar atmosphere). This has been shown in detail by recent studies of Szot *et. al.* [4] for SrTiO_3 substrates, which were reduced at a temperature of 800°C under vacuum conditions ($p_{\text{O}_2} \leq 10^{-8}$ Torr). Here, we report on the properties of samples of epitaxial Sr_2CrWO_6 thin films grown under various deposition conditions.

The Sr_2CrWO_6 films were deposited on (001) SrTiO_3 substrates from stoichiometric targets [2] by laser molecular beam epitaxy using a pulsed 248 nm KrF excimer laser operated at a repetition rate of 2 Hz. The SrTiO_3 substrates were atomically flat after etching in buffered HF and a high temperature annealing step in oxygen atmosphere. For the films grown on Nb doped (1% Nb) (001) SrTiO_3 substrates some of the substrates were not annealed in an oxygen atmosphere prior to the deposition process. The growth process was monitored by RHEED (Reflection High Energy Electron Diffraction) and the surface quality was examined by in-situ AFM (Atomic Force Microscopy) after the deposition process. Fig. 2 shows the RHEED intensity oscillations of the (0,0) diffraction spot recorded during the deposition process of two different *c*-axis oriented Sr_2CrWO_6 films. The molecular layer-by-layer or Frank-van der Merwe growth mode [5] is achieved for a deposition in an Ar/O₂ (99%/1%) atmosphere at a substrate temperature of 800°C and an energy density on the target of ~ 1.3 J/cm². A single RHEED oscillation corresponds to the growth of half a unit cell of Sr_2CrWO_6 , which was confirmed by X-ray reflectometry. Sample DP27 (see Fig. 2a) was grown in such way that the film material required for the growth of a single unit cell was provided in a short pulse sequence followed by a pause to allow for surface reorganization. It can be clearly seen in Fig. 2a that the RHEED intensity after each pulse package is continuously decreasing. This is caused by the fact that for the growth of exactly one unit-cell 12.4 laser pulses instead of 13 pulses would have been necessary. The intensity was found to increase significantly during the longer break after 104 pulses due to an ongoing surface reorganization process. Sample DP33 (Fig. 2b) was

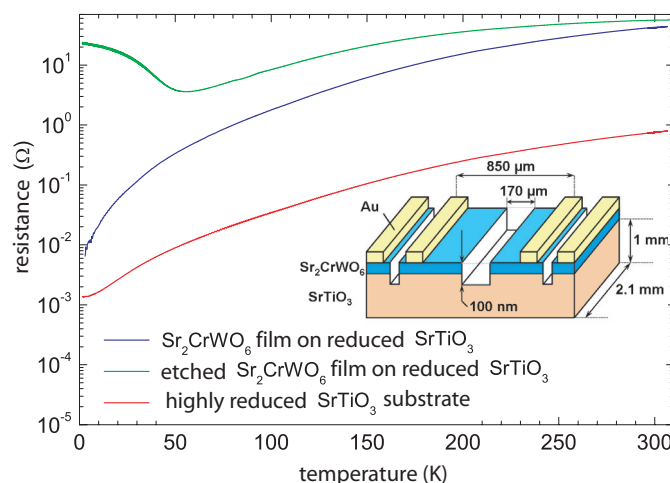


Figure 1: Resistance versus temperature of a Sr_2CrWO_6 film deposited on SrTiO_3 . Also shown is the $R(T)$ dependence of the same sample after etching and that of a highly reduced SrTiO_3 substrate [3].

¹This work is supported by the BMBF through project 13N8279.

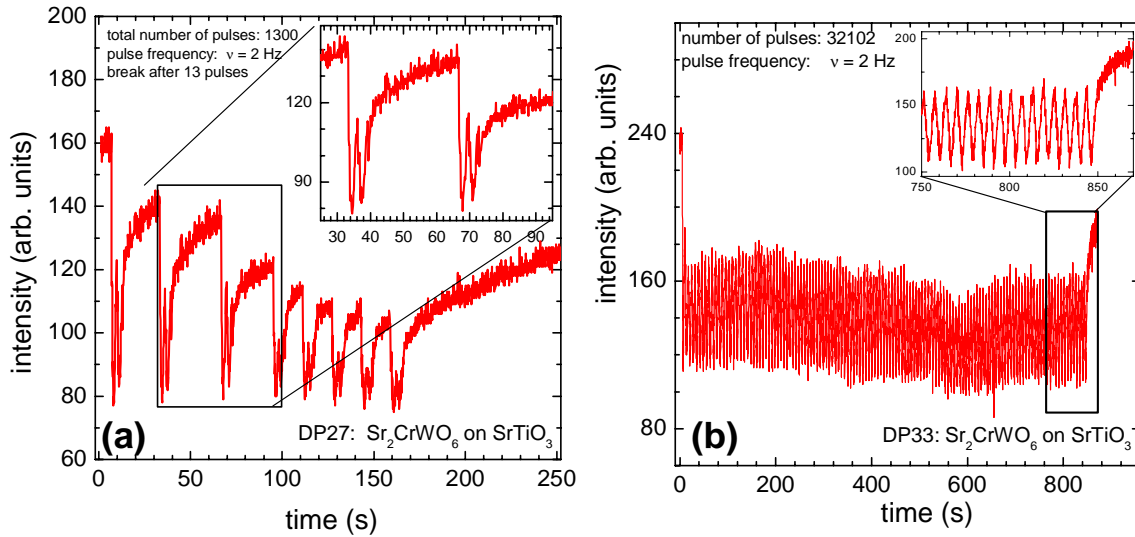


Figure 2: RHEED intensity oscillations observed during the growth of Sr_2CrWO_6 thin films, the inset shows part of the pattern on an enlarged scale. (a) film DP27 grown on a (001) SrTiO_3 substrate and (b) film DP33 grown on a Nb doped (001) SrTiO_3 substrate.

grown in a different mode. Here, the target was ablated continuously by laser pulses at a repetition rate of 2 Hz with breaks only after high numbers of pulses (up to 1 708 pulses in a row). Fig. 2b shows that the intensity of the maxima of the oscillations almost stays constant and increases again after the ablation is stopped. Clear RHEED oscillations were recorded for this sample during the whole growth process involving 32 102 laser pulses corresponding to a final thickness of 1 012 nm.

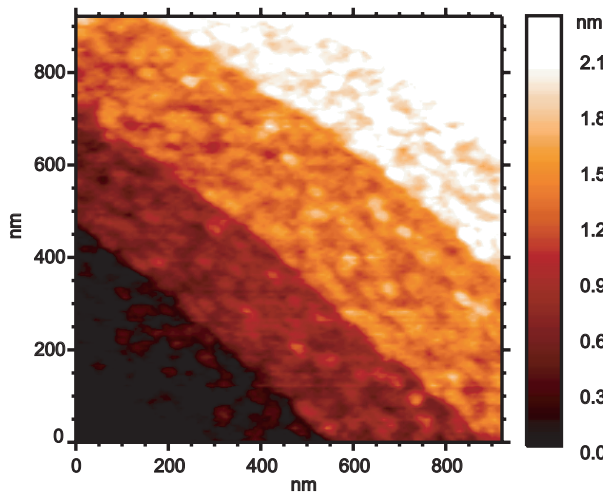


Figure 3: AFM image of a 42 nm thick epitaxial Sr_2CrWO_6 film grown on a (001) SrTiO_3 substrate. About 200 nm wide terraces separated by about 4 nm high steps are clearly visible.

As the SrTiO_3 substrates become conducting under low oxygen partial pressure of $p_{\text{O}_2} \lesssim 10^{-8}$ Torr at the high deposition temperatures, a set of samples was grown at different values of the oxygen partial pressure and a substrate temperature of 800°C . Their crystalline quality was examined by x-ray diffraction. The best results were obtained for films grown in an Ar/O_2 (99%/1%) atmosphere at a total pressure of $p = 5.5 \times 10^{-4}$ Torr. Their crystalline properties have been described already in the previous paragraph. For films grown at deposition atmospheres with a higher oxygen content (2%, resp. 3%), the film quality was found to deteriorate considerably: $\text{FWHM}_{(2\%)} = 0.23^\circ$, $\text{FWHM}_{(3\%)} = 0.31^\circ$. Therefore, the oxygen content of

Fig. 3 shows an in-situ AFM image of a 42 nm thick film. Clearly, a terrace structure caused by the nonvanishing substrate miscut with about 0.4 nm high steps corresponding to half a unit cell of Sr_2CrWO_6 can be seen. The AFM image clearly demonstrates the very small surface roughness of the film achieved by the layer-by-layer growth mode. X-ray analysis shows a good crystalline quality of the films. Only (00ℓ) peaks were detected within the resolution of our four circle x-ray diffractometer for the samples grown on SrTiO_3 . The rocking curves of the (004) film peaks had a full width at half maximum (FWHM) of only 0.04° .

As the SrTiO_3 substrates become conducting under low oxygen partial pressure of $p_{\text{O}_2} \lesssim 10^{-8}$ Torr at the high deposition temperatures,

the deposition atmosphere has to be less than about 1% to achieve films with a high crystalline quality. In order to examine, whether or not an oxygen partial pressure of $p_{O_2} = 5.5 \times 10^{-6}$ Torr is sufficient to keep the SrTiO₃ substrate insulating, two separate measuring bridges were patterned into sample DP26. The film was overetched up to a depth of 110 nm (film thickness 87 nm). This means that in case of an insulating substrate no current can flow between both bridges. However, a significant conductivity was measured between both bridges in a simple two probe measurement at room temperature. From this we can conclude that it is impossible to achieve Sr₂CrWO₆ films with a high crystalline quality without making the surface of the SrTiO₃ substrate conducting by reducing the oxygen partial pressure. We note that also a reduction of the deposition temperature to 600°C does not solve the problem, since the crystalline quality of the Sr₂CrWO₆ films is also reduced ($\text{FWHM}_{(600^\circ\text{C})} = 0.30^\circ$).

In summary, we have grown epitaxial Sr₂CrWO₆ thin films with very high crystalline quality on doped and undoped (001) SrTiO₃ substrates by laser molecular epitaxy. In order to avoid that the SrTiO₃ substrate becomes conducting, the oxygen partial pressure and/or the substrate temperature have been changed. However, both a high crystalline quality of the Sr₂CrWO₆ films and an insulating behavior of the SrTiO₃ substrate could not be achieved at the same time. Therefore, a different approach to solve this problem is necessary (e.g. an insulating buffer layer).

References

- [1] J. B. Philipp, P. Majewski, L. Alff, A. Erb, and R. Gross, T. Graf, and M.S. Brandt, J. Simon, T. Walther, and W. Mader, D. Topwal, and D.D. Sarma, *Phys. Rev. B* **68**, 144431 (2003).
- [2] J. B. Philipp, D. Reisinger, M. Schonecke, A. Marx, A. Erb, L. Alff, and R. Gross, *Appl. Phys. Lett.* **79**, 3654 (2001).
- [3] J. B. Philipp, *Spinabhängiger Transport in Übergangsmetalloxiden*, PhD Thesis, TU München(2003).
- [4] K. Szot, W. Speier, R. Carius, U. Zastrow, and W. Beyer, *Phys. Rev. Lett.* **88**, 075508 (2002).
- [5] T. Terashima, Y. Bando, K. Iijima, K. Yamamoto, K. Hirata, K. Hayashi, K. Kamigaki, and H. Terauchi, *Phys. Rev. Lett.* **65**, 2684 (1990).

Single Crystal Growth of Cuprate Superconductors

Andreas Erb

The physics of the cuprate superconductors is one of the most intensively studied fields in modern solid state physics. Nevertheless, up to now there is no commonly accepted theory of high-temperature superconductivity. On the other hand, strong progress has been made especially in the last years in the quality of the available samples of the cuprate superconductors as well as in the precision of the measurement techniques. A good example for this development is the detection of the fusion of the vortex lattice by specific heat measurements [1, 2] in newly developed ultra pure samples [3, 4, 5] with extremely low flux pinning. This experiment would not have been possible without the improvement in sample quality as well as in the development of the measuring techniques. Thus, the interesting field of vortex physics could only be studied after the sample quality and the measurement technique had reached a higher standard. The same applies for a series of other experiments.

It is for this reason that a new laboratory for crystal growth of oxide systems has been build up at the Walther-Meißner-Institute in the last years. With the installation of a mirror furnace at the end of last year this laboratory has been completed. We can now routinely grow single crystals of the cuprate superconductors and other oxide systems in highest quality. Concerning the quality of cuprate single crystals for the different compounds one can state the following:

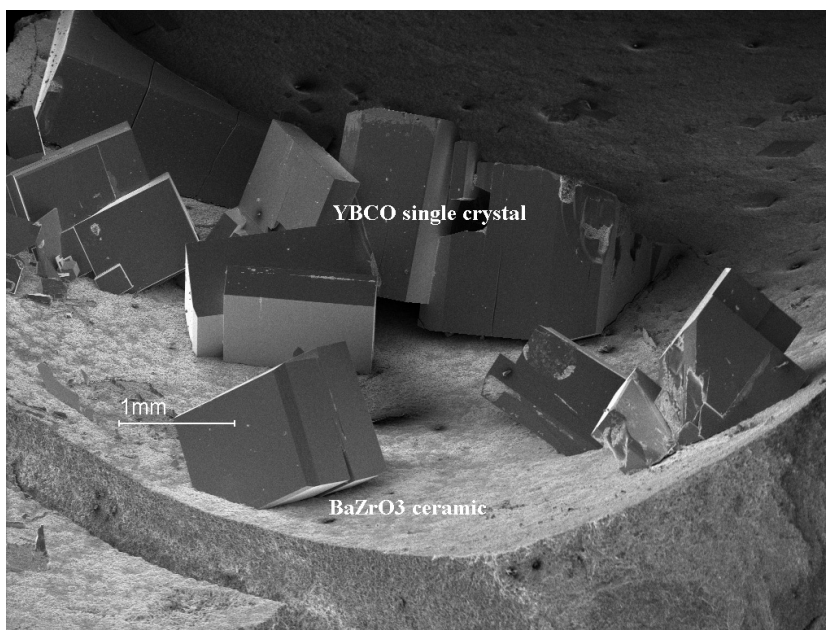


Figure 1: Single crystals of the high temperature superconductor $\text{YBa}_2\text{Cu}_3\text{O}_{7-\delta}$ inside a BaZrO_3 crucible.

$\text{YBa}_2\text{Cu}_3\text{O}_{7-\delta}$:

Because of the low solubility of the 123 compounds

in the flux (solvent) high quality single crystals without flux inclusions can only be grown in high temperature solution growth experiments in nonreactive crucibles. With the development of the inert BaZrO_3 crucibles the problem of the crucible corrosion has been solved and we are able to grow single crystals of the 123 compounds with purities up to 99.995 %. Generally, it should be mentioned that the stoichiometric $\text{YBa}_2\text{Cu}_3\text{O}_{7-\delta}$ compound would be the ideal compound to probe the phase diagram of the high temperature superconductors. However, unfortunately not the whole doping regime is accessible using this compound only.

Bi-2212 ($\text{Bi}_2\text{Sr}_2\text{CaCu}_2\text{O}_8$), Bi-2201 ($\text{Bi}_2\text{Sr}_2\text{CuO}_6$) and Bi-2223 ($\text{Bi}_2\text{Sr}_2\text{Ca}_2\text{Cu}_3\text{O}_{10+\delta}$):

Besides the 123-compounds the Bi-based compounds are interesting high- T_c materials, which also allow to study the phase diagram in a wider range. The family of the Bi-based high- T_c materials consists of 3 compounds: the so-called 1-layer compound $\text{Bi}_2\text{Sr}_2\text{CuO}_6$ with a transition temperature of $T_c \approx 10$ K the 2-layer compound $\text{Bi}_2\text{Sr}_2\text{CaCu}_2\text{O}_8$ with a T_c of about 93 K and the 3-layer compound

$\text{Bi}_2\text{Sr}_2\text{Ca}_2\text{Cu}_3\text{O}_{10+\delta}$ with a T_c of about 110 K.

The first single crystals of these compounds have been grown in crucibles and the problem of impurities from crucible corrosion has been a problem for these compounds as well. With the development of mirror furnaces, in which the compounds can be grown containerfree by the travelling solvent floating zone (TSFZ) technique, a major improvement of the sample quality has been achieved for these compounds. Especially the compound Bi-2212

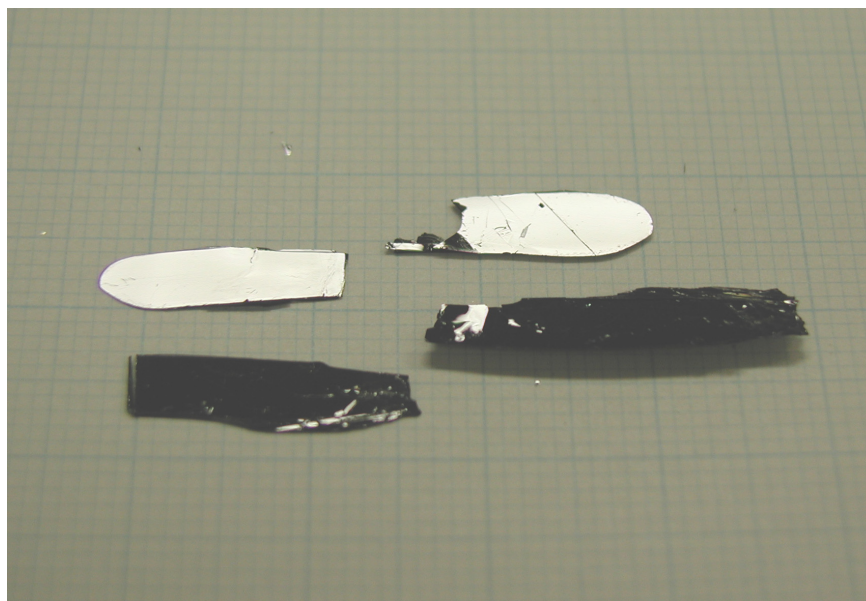


Figure 2: Single crystals of the high temperature superconductor $\text{Bi}_2\text{Sr}_2\text{CaCu}_2\text{O}_8$ grown by the Travelling-Solvent-Floating-Zone technique using a mirror furnace.

allows to cover a broad region on the p -doped region of the phase diagram of the cuprates by doping with Yttrium. We now routinely grow cm-sized crystals of the Bi-2212 and Bi-2201 compound with various doping using the mirror furnace.

214-systems: $\text{La}_{2-x}\text{Sr}_x\text{CuO}_4$, $\text{Nd}_{2-x}\text{Ce}_x\text{CuO}_4$ and $\text{Pr}_{2-x}\text{Ce}_x\text{CuO}_4$:

214-systems with the 2 compounds $\text{La}_{2-x}\text{Ba}_x\text{CuO}_4$ and $\text{La}_{2-x}\text{Sr}_x\text{CuO}_4$ were the first cuprate superconductors, which have been found [6]. Coming from the antiferromagnetic compound RE_2CuO_4 , increasing the doping with Sr^{2+} on the p -doped or Ce^{4+} on n -doped side of the phase diagram leads to the formation of a solid solution crystal, which becomes superconducting when the doping is sufficiently high. The formation of a solid solution for these compounds makes it relatively easy to cover the whole range of the doping. On the other hand it leads to intrinsic homogeneity problems during crystal growth especially for crystals which are grown in a crucible growth process. The quality of these compounds can be highly increased, when they are grown by TSFZ-technique in a mirror furnace. First growth experiments for these compounds have also been carried out and the results were promising.

In summary, all the relevant compounds required for the systematic study of the phase diagram of the cuprate superconductors, both on the p - and n -doped side, can now be grown at the crystal laboratory of the Walther-Meißner-Institute.

References

- [1] A. Junod, M. Roulin, J.-Y. Genoud, B. Revaz, A. Erb, E. Walker. *Physica C* **275**, 245 (1997).
- [2] M. Roulin, A. Junod, A. Erb, E. Walker. *J. Low Temp. Phys.* **105**, 1099 (1996).
- [3] A. Erb et al. *Physica C* **245**, 245 (1995).
- [4] A. Erb, E. Walker, R. Flükiger. *Physica C* **258**, 9 (1996).
- [5] A. Erb et al. *J. Low Temp. Phys.* **105**, 1023 (1996).
- [6] J. G. Bednorz and K. A. Müller. *Z. Phys. B* **64**, 189 (1986).

Redox Reactions and Iron Uptake in Vermiculites from Spain

Anton Lerf, Friedrich E. Wagner^a, Juan Poyato^b

^a Physics Department, Technical University of Munich, Germany

^b Universidad de Sevilla, Spain

Natural clay minerals of the 2:1 type very often contain Fe ions in the octahedral and/or tetrahedral layers. It is known for a long time that at least the octahedral iron ions are easily accessible to redox reactions; a striking example for this are the colour reactions of some amines intercalated into smectites [1]. Oxidation of the octahedral structural iron ions has also been considered as an important step in the weathering of micas to vermiculite [2]. To evaluate the extent of redox reactions one needs to know the $\text{Fe}^{2+}/\text{Fe}^{3+}$ ratio before and after the reaction. However, it is notoriously difficult to determine this ratio in natural and modified clay minerals by wet chemical methods.

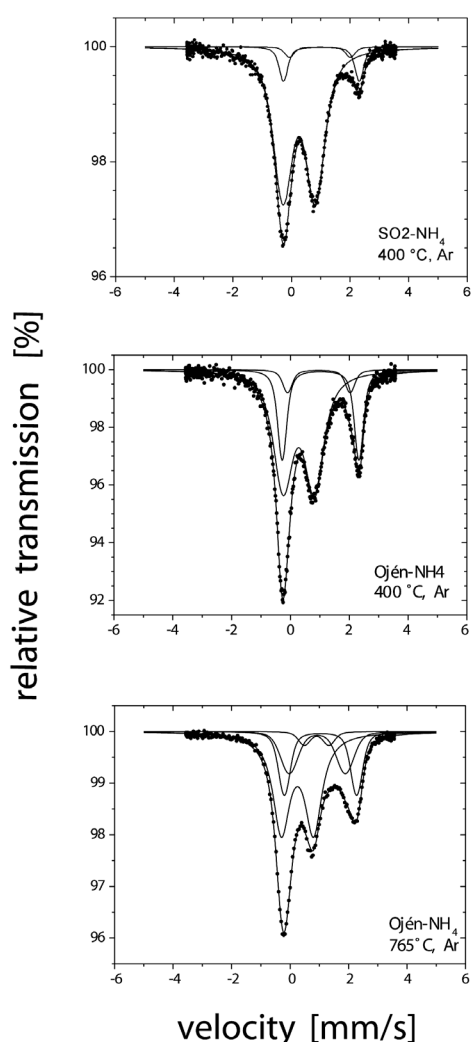


Figure 1: Mössbauer spectra of NH_4 -vermiculites from Santa Olalla and Ojen measured at room temperature after heating the sample in argon at a heating rate of $6\text{ °C}/\text{min}$. The highest temperature applied is given in the figures.

The most suitable method to derive reliable $\text{Fe}^{2+}/\text{Fe}^{3+}$ ratios is Mössbauer spectroscopy. We report here the Mössbauer parameters measured mainly at room temperature for the vermiculites of Ojen and Santa Olalla, Spain, after various chemical modifications. The emphasis is mainly on the determination of the $\text{Fe}^{2+}/\text{Fe}^{3+}$ ratio. We investigated the maximum extent of reduction in the two vermiculites mentioned above and the iron uptake in the Santa Olalla vermiculite. In previous experiments we carried out reduction only in aqueous solutions [3]. In these experiments on the vermiculite of Santa Olalla not more than 25 % of Fe^{2+} could be obtained. The possible degree of reduction is remarkably higher in case of the vermiculite from Ojen, but does not exceed 40 % of Fe^{2+} if the sample is reduced in aqueous solution. The reason for this restriction and the difference of both vermiculites is not clear at the moment. However, we could increase the Fe^{2+} content dramatically when the hydrazinium intercalation compounds were heated up to 400 °C and the ammonium compounds to 700 °C . An even higher degree of reduction has been obtained by treating the sodium vermiculite (Santa Olalla) in a stream of H_2/N_2 (5:95). The highest amount of Fe^{2+} thus obtained is in the order of 60 %.

If the reduction is carried out at 400 °C or below, the Fe^{2+} site with the higher quadrupole splitting increases more strongly than the other. In the samples

treated at 700°C the opposite effect is observed. In addition the Fe^{2+} sites with low quadrupole splitting show a rather broad Gaussian distribution. Such a Mößbauer spectrum is obtained also for biotites treated at 850°C and interpreted as a consequence of oxygen defect formation [4]. Thus it could be possible that the high temperature reduction is accompanied with dehydration of the octahedral layer. The preference of formation of one of the two Fe^{2+} site may be indicative for the presence of Fe^{3+} sites with different redox potentials. This suggestion is further supported by the different redox behavior of strongly reduced samples with respect to organic redox active intercalates. For example the uptake of the redox active methylviologen (MV^{2+}) in the Na-vermiculite does not lead to a change of the $\text{Fe}^{2+}/\text{Fe}^{3+}$ ratio. However, if the Na-vermiculite treated with hydrogen is brought in contact with the methylviologen solution, this solution becomes strongly blue, indicative for the formation of the reduced monoradical MV^{\cdot} . This is accompanied with a remarkable drop of the Fe^{2+} content.

An interesting electron mediator in the interlayer space could be the Fe-ion itself. It is known to bind organic species in the interlayer space and, especially the Fe^{3+} -ions induce oxidation reactions in the interlayer space, including the formation of the conducting polypyrrole system [5]. In addition, this ion is magnetic and could induce some magnetic ordering between the iron sites in the host layers. We tried to intercalate Fe^{2+} as well as the Fe^{3+} ions. Preliminary experiments show that most of the Fe^{3+} is deposited on the external surface of the clay particles, even at low pH. This is due to the formation of positively charged iron oxide nuclei which interact strongly with the negatively charged clay surfaces prior to intercalation. If one tries to circumvent this problem by insertion of positively charged polynuclear iron clusters, the same result is obtained since the clusters became destroyed before intercalation. Only the amount of iron-oxides deposited seems to be lower. The Mößbauer spectra that the species intercalated is very probable the dimer $[\text{Fe}_2\text{O}_2(\text{H}_2\text{O})_y]^{4+}$.

References

- [1] E.A. Hauser and M.B. Leggett, *J. Amer. Chem. Soc.* **62**, 1811 (1940).
- [2] C.B. Roth, M.L. Jackson, E.G. Lotse, and J.K. Syers, *Isr. J. Chem.* **6**, 261 (1968).
- [3] A. Lerf, F.E. Wagner, and J. Poyato, *Solid State Ionics* **141-142**, 479 (2001).
- [4] C.S. Hogg and R.E. Meads, *Miner. Mag.* **40**, 79 (1975).
- [5] A. Moreale, P. Coos, and C. Badot, *Clay Miner.* **20**, 29 (1985).

Dilution Refrigerator with Pulse-Tube Precooling: a "Dry" Millikelvin Cooler

K. Uhlig

In last year's report we described the setup of a $^3\text{He}/^4\text{He}$ dilution refrigerator which was precooled by a closed-cycle refrigerator, a so-called pulse tube fridge. This commercially available cooler replaces the commonly used liquid helium (and nitrogen) bath in our cryostat [1].

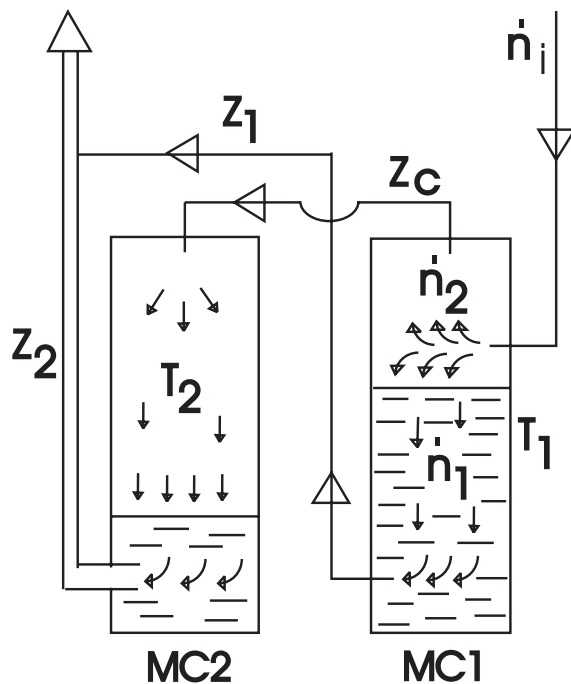


Figure 1: Flow scheme of a double mixing chamber (see text).

DMC is shown in Fig. 1; its working method is as follows: The flow of ^3He (\dot{n}_i), after it leaves the last heat exchanger and enters the first mixing chamber (MC1), is divided in two streams. The first one (\dot{n}_1) is diluted in MC1, and its cooling capacity is used to precool the remaining part of the stream (\dot{n}_2) to the temperature T_1 of MC1 which is then diluted in the second mixing chamber MC2. The flow distribution is mainly controlled by the flow impedances z_1 and z_2 of the exit tubes of MC1 and MC2. With this method the base temperature T_2 of MC2 is lowered by nearly a factor of two compared to a single mixing chamber. By measuring the temperatures of MC1 and MC2 the external heat leak flowing into MC2 can be calculated. This heat leak is of special interest as it could be caused by the small vibrations of the pulse-tube cooler and possibly limits the base temperature of the dilution unit.

In Fig.2 the temperatures at several locations of the dilution refrigerator are depicted as a function of the ^3He throughput. The temperature of the first step exchanger is in the vicinity of 60 mK, and the one of the second step exchanger of about 30 mK. Then we find the temperature of MC1, depending on the throughput, between 10 mK and 14 mK; and finally the lowest temperatures were measured in MC2 between 4.5 mK and 6 mK. The lowest temperature found was 4.3 mK; the melting curve of ^3He and PLTS 2000 data were used for millikelvin thermometry.

The advantages of this novel type of refrigerator are eye-catching. Not only does it eliminate the fussing with regular refills of the helium dewar, but even more importantly it now facilitates taking measurements without interruption. The resistance and capacitance of electrical leads remain constant during the experiment, and with this cryostat there are no frozen or wet helium recovery lines after a helium transfer.

To demonstrate the performance of the cooler it was equipped with a better dilution unit than before. It consisted of a continuous heat exchanger, two small step heat exchangers and had a so-called double mixing chamber (DMC) [2]. A sketch of a

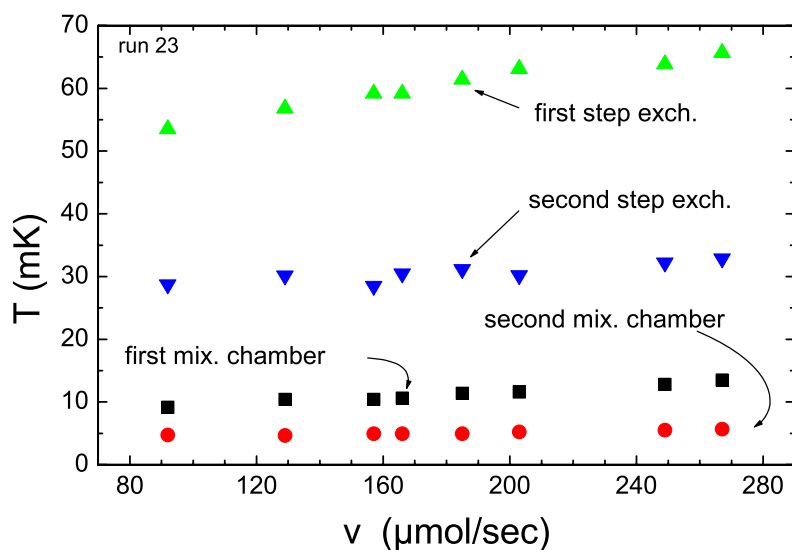


Figure 2: Temperatures at various stages of the dilution refrigerator.

Presumably the temperature gap between the experimental values of T_2 and the expected values of $T_2(0)$ is caused by a heat leak which in the case explained above amounts to 75 nW; it is constant over the entire range of ^3He throughputs measured. Possible sources for a heat leak are frictional heating and thermal conduction in the connection lines z_1 , z_2 , and z_c , or heating effects due to vibrations of the pulse-tube refrigerator and the roots pump which circulates the ^3He . It is also conceivable that a combination of the effects enumerated above is causing the heating. It would be important for future experiments to pin down the source of the heat leak.

References

- [1] K.Uhlig, *Cryogenics* **42**, 73 (2002).
- [2] G. M. Coops, A. T. A. M. de Waele, and H. M. Gijssman, *Cryogenics* **19**, 659 (1979).

In Fig.3 the base temperatures T_2 of MC2 is shown in more detail (T_2 is plotted as a function of the still cooling power). Also included in the graph is a calculated curve $T_2(0)$ for the temperature of the second mixing chamber which was derived from the corresponding temperatures T_1 of MC1

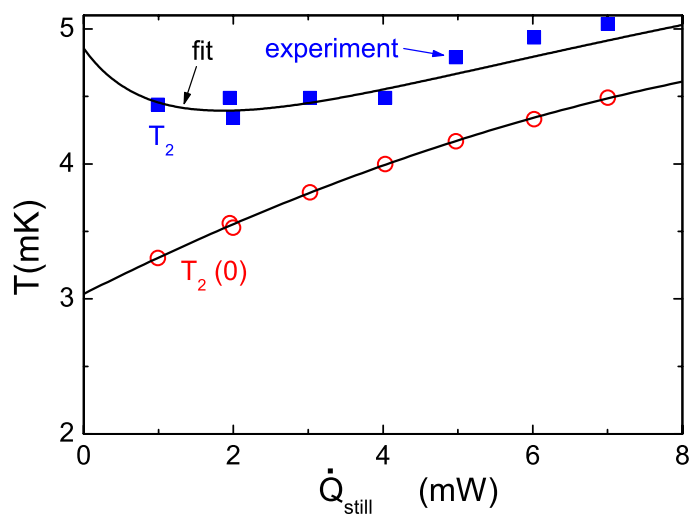


Figure 3: Experimental values of the second mixing chamber T_2 and theoretically expected temperature curve $T_2(0)$ for a vanishing external heat leak. The fit to the data is made with a theoretical model [2].

Experimental Facilities and Infrastructure

Within the last years, several new experimental facilities and various components of the technical infrastructure have been installed at the Walther-Meissner-Institute. On the following pages a brief overview is given on the main equipment and techniques that are available at the Walther-Meissner-Institute at present.

UHV-Laser-MBE

The Walther-Meissner-Institute operates a UHV-Laser-Molecular Beam Epitaxy (L-MBE) system for the growth of complex oxide heterostructures. The system has been designed to meet the special requirements of oxide epitaxy. The UHV cluster tool consists of the following main components:

- central transfer chamber.
- load-lock chamber with heater system for substrate annealing.
- laser deposition chamber with in-situ reflection high energy electron diffraction (RHEED) system, laser substrate heating system, and atomic oxygen source. The RHEED system has been modified to allow for the operation at high oxygen partial pressure up to 0.5 mbar.
- surface characterization chamber with UHV scanning force microscope (Omicron).
- metallization chamber with a four heart electron gun system and a liquid nitrogen cooled sample stage. The sample holder can be tilted for shadow evaporation.
- KrF excimer laser.

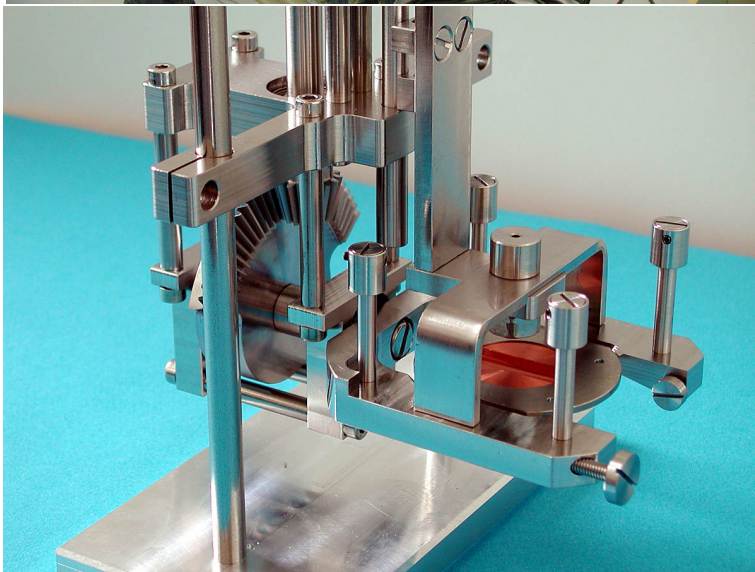
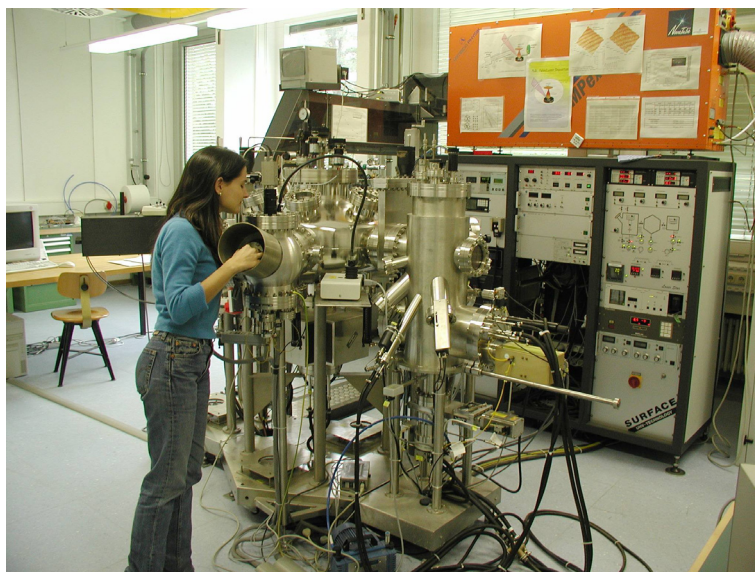


Figure 1: Top: UHV-Laser-Molecular Beam Epitaxy System. Bottom: Sample holder for metallization chamber allowing for evaporation under different angles.

The system is used for the growth of complex oxide heterostructures consisting of superconducting, magnetic and dielectric materials such as the high-temperature superconductors, the doped manganites, the double perovskites, magnetite etc..

During 2002 and 2003, the laser molecular beam epitaxy system (laser-MBE) which was installed at the Walther-Meissner-Institut during 2001 has been extended and modified. In particular, the substrate heating system and the temperature control unit was changed from a resistive radiation heater to a new infrared laser heating system (see Fig. 3, left) including a pyrometer for determining the sample temperature. In addition, a source for atomic oxygen has been added. The main advantage of the new heating system is that only the substrate is heated while the surrounding parts are hardly affected (Fig. 3, right). In this way one can achieve an essentially better vacuum at temperatures well above 1000°C . The achievable substrate temperature is limited by the melting point and the size of the substrate material (approx. 1410°C for a $5 \times 5 \text{ mm}^2$ silicon substrate). The laser heating system has already been successfully used for removing the amorphous silicon oxide layer from the surface of silicon substrates at 1150°C . This is required for the epitaxial growth of oxide thin films on this substrate.

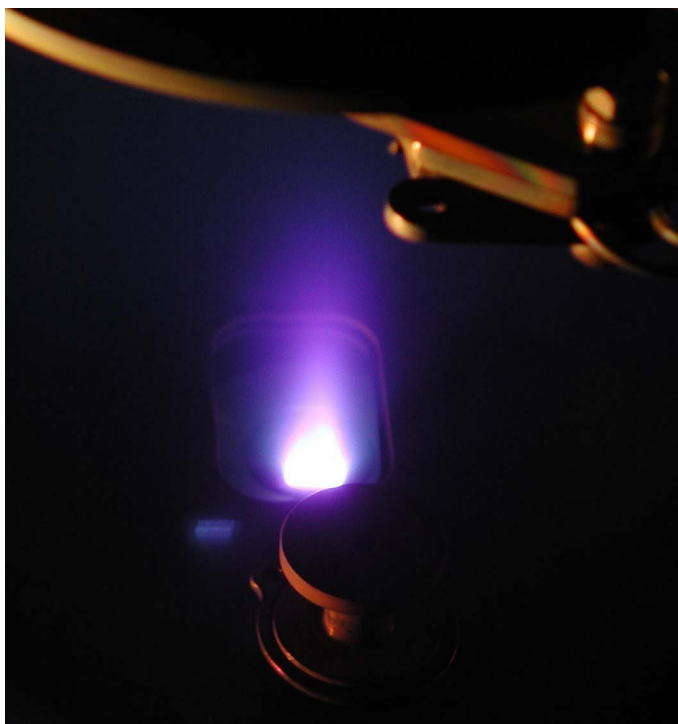


Figure 2: Pulsed Laser Deposition (PLD): When the pulse of the UV laser (KrF excimer laser, 248 nm) hits the target, the target material is ablated and the so-called laser “plume” containing highly excited atoms and molecules is formed.

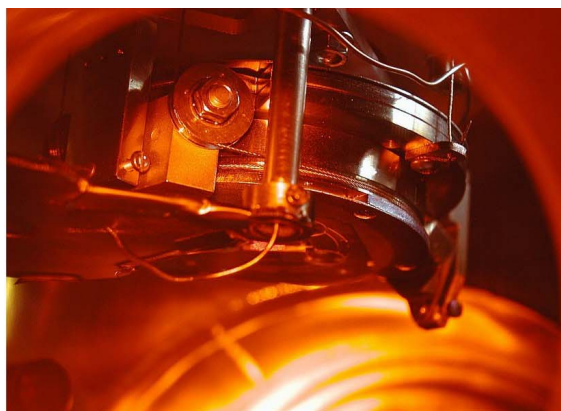


Figure 3: Components of the laser heating system: The substrate is heated using an IR diode laser head that is located in a separate box far away from the deposition chamber (left). The laser light is brought to the substrate (right) via an optical fiber.

Single Crystal Growth and Synthesis of Bulk Materials

Transition metal oxides are of great interest due to their various interesting physical properties (e.g. high temperature superconductivity, colossal magnetoresistance, ferroelectricity, nonlinear optical properties etc.) and their high potential for applications. In the last 2 years a new laboratory for the synthesis of bulk materials and single crystals has been built up at the WMI. With the installation of a four-mirror image furnace the laboratory is now fully operational. With this furnace crystals of various high temperature superconducting materials or other transition metal oxides can be grown as single crystals using the travelling solvent floating zone technique. The furnace consists basically of 4 elliptical mirrors with a common focus on the sample rod and with halogen lamps in their other focus. By irradiation of the focused light the sample rod is locally heated and eventually molten. The molten zone can be moved up and down along the entire sample rod under simultaneous rotation. By repeated melting and crystallization of the sample seed selection takes place and the formerly polycrystalline rod is transformed into a single crystal. Single crystal growth can be performed with this furnace at maximum temperatures up to 2200°C in the pressure range from 10^{-5} mbar up to 10 bar and in oxidizing, reducing as well as inert atmosphere.



Figure 4: The four-mirror image furnace installed at the crystal laboratory of the WMI. Crystals can be grown by the floating zone and traveling solvent floating zone technique at temperatures up to 2200°C and pressures up to 10 bar.

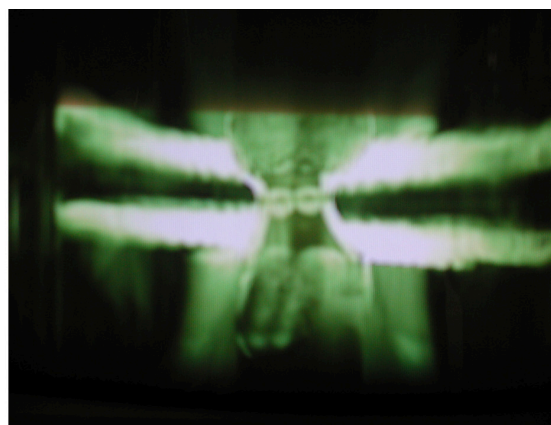
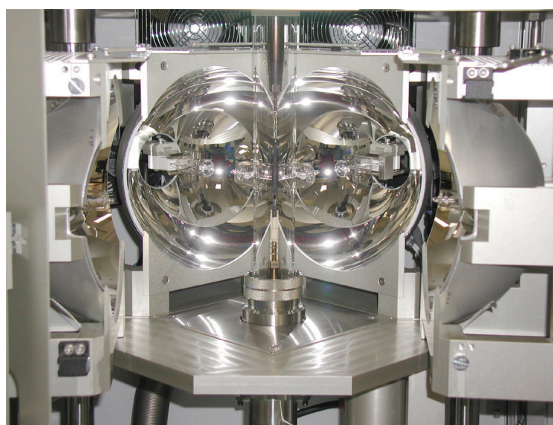


Figure 5: Left: Central part of the image furnace with the four elliptical mirrors. In the center one can see the quartz tube with the poly-crystalline rod. Right: View on the molten zone of TiO_2 (melting point: 1800°C) obtained by a CCD camera.

The X-ray diffraction systems

For x-ray analysis the Walther-Meissner-Institute operates two X-ray diffractometers (Bruker D8 Advance and D8 Discover). The two-circle system is used for powder diffraction. In this system the samples can be heated in oxygen atmosphere up to 1600°C. It is equipped with a Göbel mirror and an area detector to save measuring time. The second system is a high resolution four-circle diffractometer that can be used for reciprocal space mappings. It is equipped with a Göbel mirror and an asymmetric two-fold monochromator and allows for the texture analysis of thin film superlattices and single crystalline materials. In both systems measurements can be carried out fully computer controlled.

Beyond these two Bruker x-ray systems a Laue camera for single crystal analysis and a Debye-Scherrer camera are available.



Figure 6: The two-circle X-ray diffractometer Bruker D8 Advance.

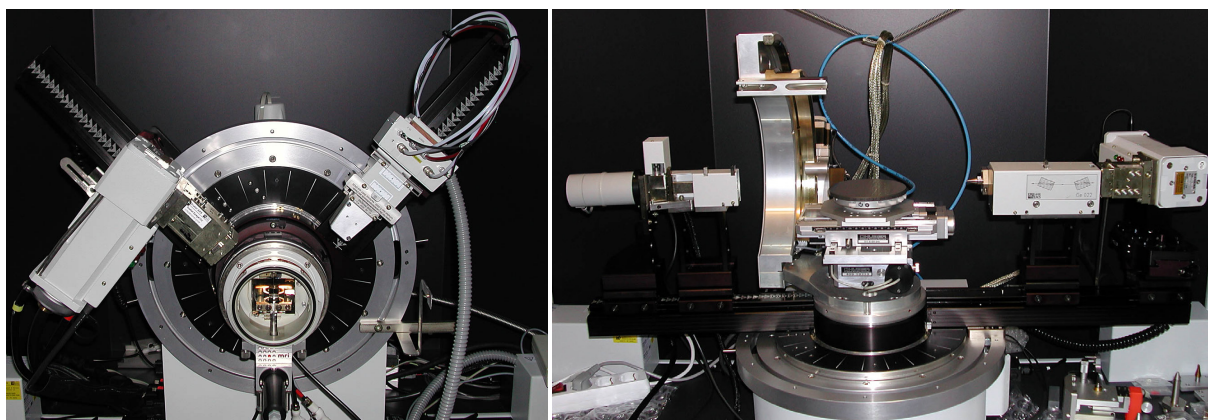


Figure 7: Left: High temperature sample holder of the D8 Advance system. Right: Four-circle high resolution X-ray diffractometer Bruker D8 Discover.



Figure 8: Quantum Design SQUID magnetometer.

The SQUID-magnetometer

For the analysis of the magnetic properties of materials, a Quantum Design SQUID magnetometer system as shown in Fig. 8 is used at the WMI. The SQUID magnetometer allows for measurements in the temperature regime from 1.5 to 400 K and provides excellent sensitivity particularly in the low field regime. Due to the excellent sensitivity of the system, thin film samples with a very small sample volume can be analyzed. In a special inset, samples can be measured up to temperatures well above room temperature (up to 700°C). For

this option the sample volume has to be reduced. The SQUID magnetometer is equipped with a superconducting solenoid allowing for a maximum field of 7 T. At present, the magnetometer is used for the characterization of magnetic materials (both in bulk and thin film form). Examples are the doped manganites, magnetite, the double perovskites or magnetic semiconductors.

The High Field Laboratory

Transport and thermodynamic properties of samples are often studied as a function of applied magnetic field. For such measurements several superconducting magnets are available at the WMI. Two of them (8/10 and 15/17 Tesla magnet system) are located in the high magnetic field laboratory in the basement of the WMI. The magnet systems are lowered below the ground level to facilitate the access to the top flange and the change of the sample sticks. The magnet systems are decoupled from the building to avoid noise due to mechanical vibrations. A variety of sample holders can be mounted allowing for e.g. sample rotation during the measurement. For standard sample holders the accessible temperature regime is $1.5 \text{ K} < T < 300 \text{ K}$. However, also $^3\text{He}/^4\text{He}$ dilution refrigerator inserts ($T > 20 \text{ mK}$) or high temperature units ($T < 700 \text{ K}$) can be mounted. All measurements are fully computer controlled (by the use of the LabView software tool) allowing for remote control and almost continuous measurements.



Figure 9: High field laboratory with Oxford 17 T magnet system.



The Clean Room Facility

For the fabrication of nanostructures and superconducting as well as spintronic devices the WMI operates a class 1000 clean room facility with an area of about 50 m². This clean room facility has been put into operation at the WMI within the year 2001. The clean room is subdivided into two parts for optical lithography and electron beam lithography, respectively. The clean room facility is equipped with the standard tools for optical lithography such as resist coaters, hot plates, wet benches, a Karl Süss MJB3 mask aligner and an optical projection lithography system. The technical infrastructure for the clean room is located in the basement of the WMI directly below the clean room area.



Figure 10: Top: Part of the clean room facility with optical lithography equipment and clean room benches. Bottom: Resist coater and hot plates.

Electron Beam Lithography

The Electron Beam Lithography System is installed in one part of the clean room facility. It consists of a Philips XL 30 SFEG scanning electron microscope (SEM) with a Raith Elphy Plus electron beam lithography system and a laser stage. The SEM is equipped with a hot field emitter and typically provides a beam diameter of less than 1.5 nm at ≥ 10 keV or about 2.5 nm at 1 keV. The lithography unit allows the fabrication of nanostructures down to about 10 nm. We have realized the controlled fabrication of metallic strip patterns with a strip width of about 20 nm. The electron beam lithography is used for the fabrication of nanostructures in metallic and oxide systems required for the study of quantum effects in mesoscopic samples.

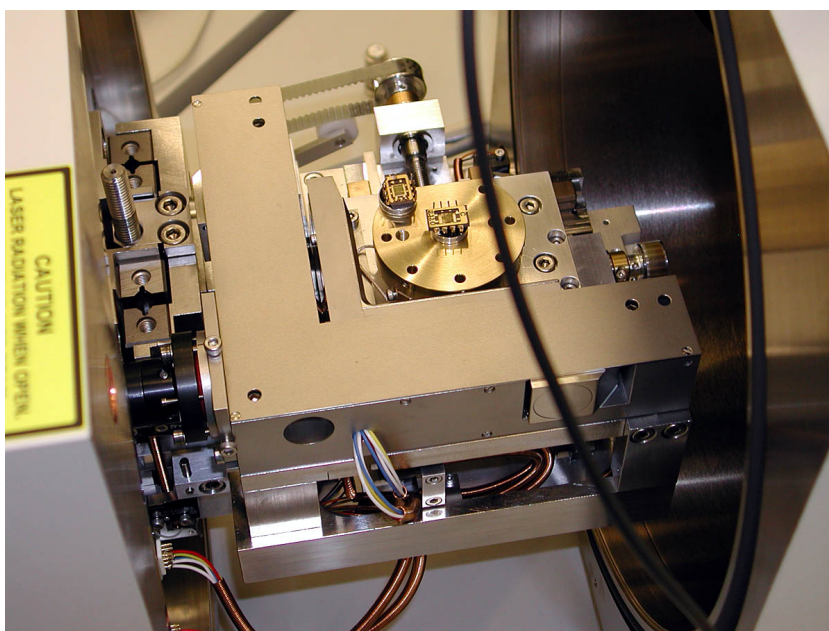
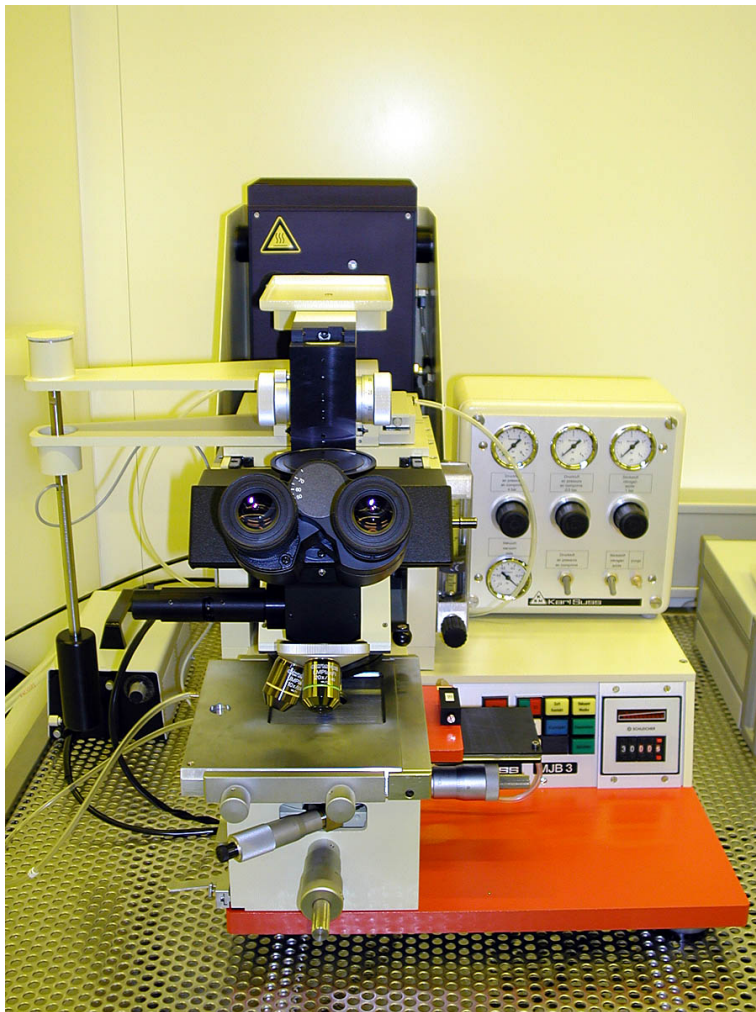


Figure 11: Top: Philips XL 30 SFEG Scanning Electron Microscope with Raith Elphy Plus Lithography System. Bottom: Raith Laser Stage.



Optical Lithography

For optical lithography a Karl Süss MJB 3 maskaligner or an optical microscope based projection system are used. The maskaligner is operating in the 1 : 1 soft or hard contact mode and is using chromium metal masks. In the projection system the mask pattern is demagnified by a factor of 5 to 100. Therefore, cheap foil masks can be used. With both systems microstructures with a lateral dimension down to $1\mu\text{m}$ can be fabricated.

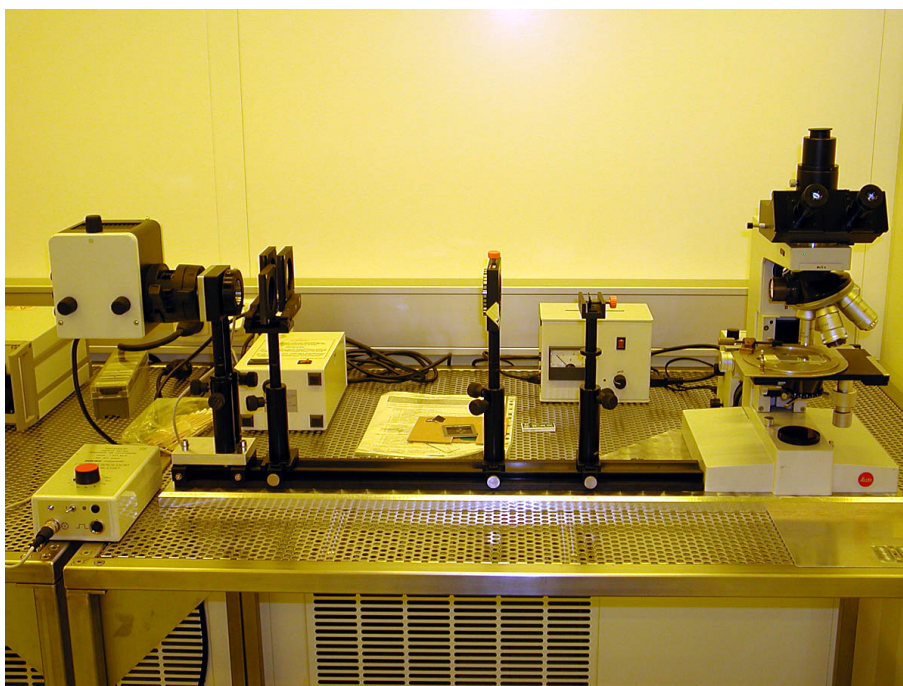


Figure 12: Top: Süss MJB 3 maskaligner for optical lithography. Bottom: Optical projection lithography based on an optical microscope.

Low and Ultra-low Temperature Facilities

The Walther-Meissner-Institute operates several low and ultra-low temperature facilities that have been developed and fabricated in-house.

The lowest temperature is achieved by the nuclear demagnetization cryostat “Bayerische Millimühle 2”. This ultra-low temperature facility consists of an in-house built dilution refrigerator and originally of two nuclear demagnetization stages. The first of those is based on a hyperfine enhanced van Vleck paramagnet PrNi_5 (0.9 mole), the second, which has been removed a few years ago, was based on purified copper (0.2 mole). The lowest temperature reached with this system was slightly below $30 \mu\text{K}$ in the copper nuclear spin system. At the moment, the first stage can be cooled to below $400 \mu\text{K}$ and, due to the large heat capacity of PrNi_5 , it stays below the mixing chamber temperature (5 mK) for nearly 3 weeks. In this cryostat three measuring sites are provided, two in a magnetic field compensated region and one in the center of an 8 T magnet. They are suitable for specific heat measurements, for capacitive torque- and SQUID magnetometry, as well as for transport measurements (electrical und thermal conductivity). The cryostat is also equipped with a pressure cell for liquid and solid ^3He , which at the moment is used for nuclear spin resonance measurements below 1 mK.

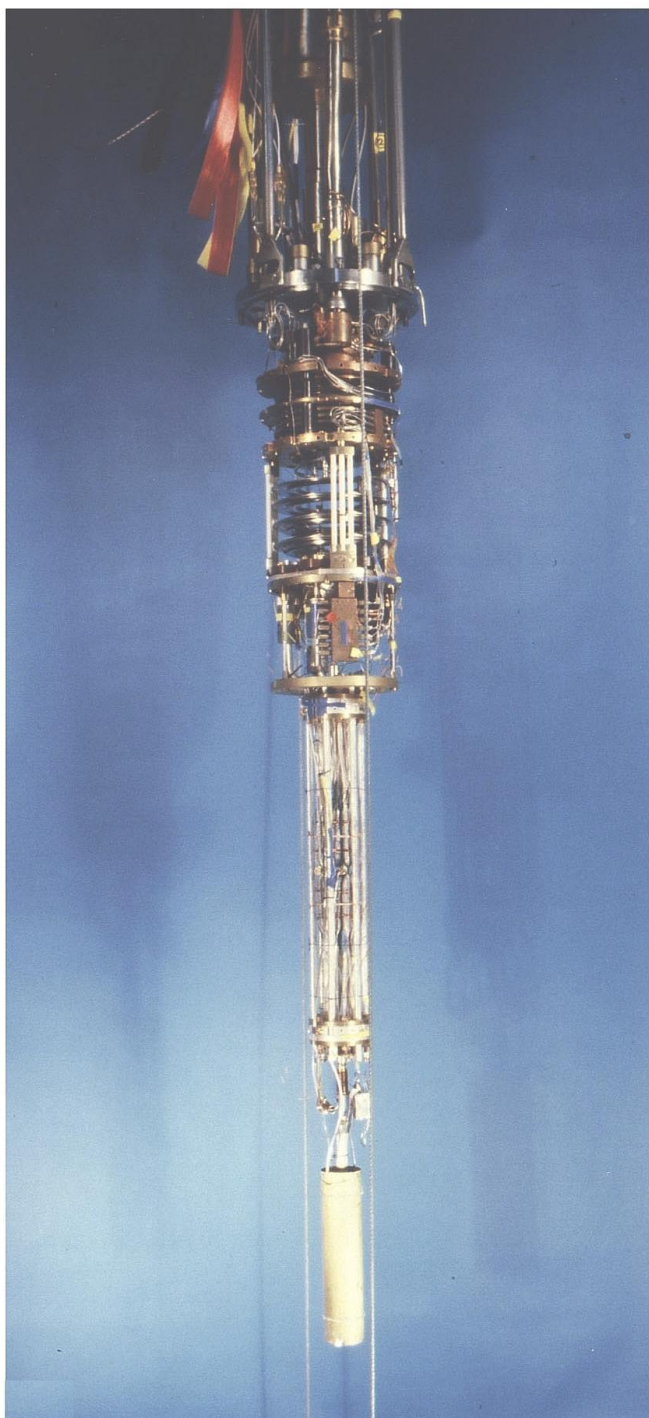


Figure 13: The dilution refrigerator and the nuclear demagnetization stage of the nuclear demagnetization cryostat “Bayerische Millimühle 2”.



Figure 14: A “dry” millikelvin cooler: dilution refrigerator with pulse-tube pre-cooling.

Within the last years, the Walther-Meissner-Institute has developed a dilution refrigerator with pulse-tube pre-cooling. We denote such system as a “dry millikelvin cooler”, since it does no longer require liquid helium for precooling. In contrast, this ultra-low temperature system is pre-cooled using a pulse tube refrigerator. The system is under test at the moment and temperature below 10 mK have already been achieved at the mixing chamber.

We note that the pulse-tube refrigerator based precooling system also cannot only be used for providing the base temperature of a dilution refrigerator but also for various other cryogenic systems. The dry systems are highly attractive for locations where the supply with liquid helium is complicated and/or expensive. In future they even may displace standard liquid helium systems in low temperature laboratories.

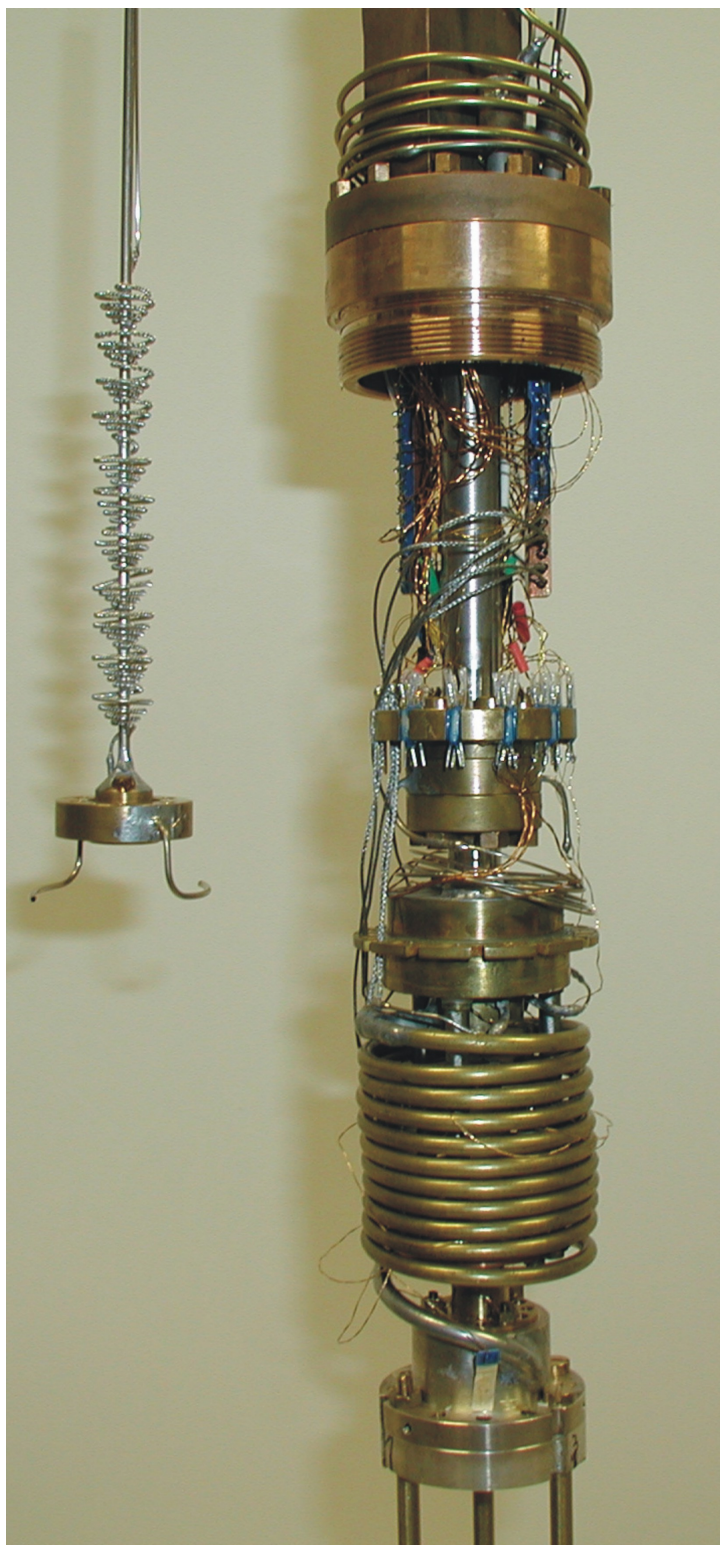


Figure 15: Dilution refrigerator insert with the Joule-Thompson stage, the heat exchanger and the mixing chamber.

The Walther-Meissner-Institute also develops and fabricates dilution refrigerator inserts for temperatures down to about 20 mK. The inserts fit into all cryogenic systems (e.g. superconducting magnets) having a two inch bore. They allow fast sample change and rapid cool down cycles of less than five hours.

The dilution refrigerator inserts are engineered and fabricated in-house and are also provided to other low temperature laboratories for ultra low temperature experiments.

New Network Infrastructure

Since 2002 a new era for electronic data transfer began at the Walther-Meissner-Institute. A new data network infrastructure started operation. It was planned and installed in close cooperation with the Leibniz-Rechenzentrum and is based on fiber optic cables. It replaces the old coaxial ring line ("yellow cable") which was installed in the early days of computer network technology. About 270 double fiber optic lines with an average length of 50 m were installed in the WMI together with the corresponding number of data link sockets in all the labs and offices. In the basement of the institute, one room has been renovated, which is now hosting a new central fiber optic network switch (see Fig. 16). There, the fibers coming from all rooms in the WMI meet together (Fig. 17, left). The switch provides the data link between the nodes within the WMI as well as from the WMI to the internet. The structured concept of the new network consisting of single node-to-node connections leads to higher reliability and efficiency for the data transfer as compared to the old coaxial ring lines (Fig. 17, right). With possible transfer rates up to 10 GBit/s per node the new WMI fiber optic network is prepared for the coming generations of hardware and software.



Figure 16: In the basement of the WMI a new stacked switch providing 68 fiber optic connectors was installed to switch data packets within the WMI as well as from the WMI to the internet and vice versa.



Figure 17: Left: 270 double optical fibers from all rooms of the WMI joining at the central switch. Right: The old coaxial cables after removal.

Publications

1. WELTER B., KROCKENBERGER Y., EINZEL D., NAITO M., ALFF L., GROSS R.,
Pseudogap and conservation of states in electron doped high-temperature superconductors.
Physica B **388-389**, 299 (2003).
2. EINZEL D.,
Interpolation of BCS Response Fluctuations.
J. of Temp. Phys. **130**, 493-508 (2003).
3. EINZEL D.,
Analytic Two-Fluid-Description of Unconventional Superconductivity.
J. of Low Temp. Phys. **131**, 1-24 (2003).
4. RAO M.S. Ramachandra, RAVINDRANATH V., GROSS R.,
Evidence of reduction in spin disorder by Ho³⁺ doping in La_{0.7}Ca_{0.3}MnO₃.
Phil. Mag. **B 83**, 1631 (2003).
5. PHILIPP J.B., REISINGER D., SCHONECKE M., OPEL M., MARX A., ERB A., ALFF L., GROSS R.,
Epitaxial growth and transport properties of Sr₂CrWO₆ thin films.
J. Appl. Phys. **93**, 6853 (2003).
6. REISINGER D., BLASS B., KLEIN J., PHILIPP J.B., SCHONECKE M., ERB A., ALFF L., GROSS R.,
Sub-unit cell layer-by-layer growth of Fe₃O₄, MgO, and Sr₂RuO₄ thin films.
Appl. Phys. A **77**, 619-621 (2003).
7. ALFF L., WELTER B., KROCKENBERGER Y., GROSS R., MANSKE D., NAITO M.,
Hidden pseudogap regime under the dome of superconductivity in electron doped cuprate high-temperature superconductors.
Nature **422**, 698 (2003).
8. GÖNNENWEIN S.B.T., GRAF T., WASSNER T., BRANDT M.S., STUTZMANN M., PHILIPP J.B., GROSS R., KOEDER A., SCHOCH W., WAAG A.,
Spin wave resonance in Ga_xMn_{1-x}As.
Appl. Phys. Lett. **82**, 730 (2003).
9. BARKOV F.L., VINNIKOV L. Ya., KARTSOVNIK M.V., KUSHCH N.D.,
Vortex lattice anisotropy in the conducting plane of organic superconductors.
Physica C **385**, 568-570 (2003).
10. KOVALEV A.E., KARTSOVNIK M.V., ANDRES D., JANSEN A.G.M., KUSHCH N.D.,
Heat capacity of the (ET)₂KHg(SCN)₄ below the "kink" transition.
Synthetic Metals **133-134**, 131-132 (2003).
11. KARTSOVNIK M., GRIGORIEV P., BIBERACHER W., GRÖGER A., ANDRES D., PESOTSKII S., KUSHCH N.,
Effects of low dimensionality on the classical and quantum parts of the magnetoresistance of layered metals with a coherent interlayer transport.
Synthetic Metals **133-134**, 111-112 (2003).
12. VENTURINI F., HACKL R., MICHELUCCI U.,
Comment on Nonmonotonic d_{x²-y²} Superconducting Order Parameter in Nd_{2-x}Ce_xCuO₄.
Phys. Rev. Lett. **90**, 149701 (2003).
13. KARTSOVNIK M., GRIGORIEV P., BIBERACHER W.,
Slow oscillations of magnetoresistance in layered organic metals.
Synthetic Metals **135-136**, 655-656 (2003).
14. KLEIN J., PHILIPP J.B., REISINGER D., OPEL M., MARX A., ERB A., ALFF L., GROSS R.,
Orbital order and anisotropic transport properties in doped manganites induced by epitaxial coherency strain.
J. of Appl. Phys. **93**, 7373-7375 (2003).
15. REISINGER D., SCHONECKE M., BRENNINGER T., OPEL M., ERB A., ALFF L., GROSS R.,
Epitaxy of Fe₃O₄ on Si(001) by pulsed laser deposition using a TiN/MgO buffer layer.
J. of Appl. Phys. **94**, 1857-1863 (2003).
16. MAKI K., DORA B., KARTSOVNIK M., VIROSZTEK A., KORIN-HAMZIC B., BASLETIC M.,
Unconventional Charge-Density Wave in the Organic Conductor α -(BEDT-TTF)₂KHg(SCN)₄.
Phys. Rev. Lett. **90**, 256402 (2003).

17. CUSTERS J., GEGENWART P., NEUMAIER K., WILHELM H., OESCHLER N., ISHIDA K., KITAOKA Y., GEIBEL C., STEGLICH F.,
Quantum criticality in YbRh_2Si_2 .
J. Phys.: Condens. Matter **15**, 2047-2053 (2003).
18. JANOSSY A., FEHER T., ERB A.,
Diagonal Antiferromagnetic Easy Axis in Lightly Hole Doped $\text{Y}_{1-x}\text{Ca}_x\text{Ba}_2\text{Cu}_3\text{O}_6$.
Phys. Rev. Lett. **91**, 177001 (2003).
19. PHILIPP J.B., MAJEWSKI P., ALFF L., ERB A., GROSS R., GRAF T., BRANDT M.S., SIMON J., WALTHER T., MADER W., TOPWAL D., SARMA D.D.,
Structural and doping effects in the half-metallic double perovskite A_2CrWO_6 (A = Sr, Ba and Ca).
Phys. Rev. B **68**, 144431 (2003).
20. GRAF T., GJUKIC M., HERMANN M., BRANDT M.S., STUTZMANN M., GÖRGENS L., PHILIPP J.B., AMBACHER O.,
Growth and characterization of GaN: Mn exitaxial films.
J. of Appl. Phys. **93**, 9697 (2003).
21. VENTURINI F.,
Evidence for a Metal-Insulator Transition in Overdoped Cuprates: New Raman Results
B. Kramer (Ed.): Adv. in Solid State Phys. **43**, 253-266 (2003).
22. ANDRES D., KARTSOVNIK M.V., GRIGORIEV P.D., BIBERACHER W., MÜLLER H.,
Orbital quantization in the high-magnetic-field state of a charge-density-wave system.
Phys. Rev. B **68**, 201101 (2003).
23. REISINGER D., SCHONECKE M., BRENNINGER T., OPEL M., ERB A., ALFF L., GROSS R.,
Epitaxy of Fe_3O_4 on Si(001) by pulsed laser deposition using a TiN/MgO buffer layer.
J. Appl. Phys. **94** 1857 (2003).
24. UHLIG K.,
Messung tiefster Temperaturen.
Akademie Aktuell **9**, (2003).
25. PÉREZ-RODRIGUEZ J.L., PÉREZ-RODRIGUEZ L.A., POYATO J., LERF A.,
Layer charge modification by mechanical treatment of the Santo Olalla vermiculite.
Solid State Phenomena **90-91**, 515-520 (2003).
26. EINZEL D.,
Supraleitung und Suprafluidität: zum Physik-Nobelpreis 2003
Akademie Aktuell, Zeitschrift d. BAdW (2003).
27. ALFF L., PHILIPP J.B., REISINGER D., KLEIN J., CARBONE G., VIGLIANTE A., GROSS R.,
Biaxial strain and orbital order in $\text{La}_{2/3}\text{Ca}_{1/3}\text{MnO}_3$ thin films.
Physica B **329-333**, 965-966 (2003).
28. CUSTERS J., GEGENWART P., WILHELM H., NEUMAIER K., TOKIWA Y., TOVARELLI O., GEIBEL C., STEGLICH F., PEPIN C., COLEMAN P.,
The break-up of heavy electrons at a quantum critical point.
Nature **424**, 524 (2003).
29. MILLAN-CHACARTEGUI C., DEPPE F., SCHUBERTH E.A.,
Pulsed NMR in the Nuclear Spin Ordered Phases of Solid ^3He in a Silver Sinter.
Physica B **329**, 394 (2003).
30. GÖNNENWEIN S.B.T., WASSNER T.A., GRAF T., HÜBL H., PHILIPP J.B., OPEL M., GROSS R., KÖDER A., SCHOCH W., WAAG A., BRANDT M.S.,
Hydrogen control of ferromagnetism in a dilute magnetic semiconductor.
Nature, submitted for publication (07/2003).
31. RAMA N., PHILIPP J.B., OPEL M., ERB A., SANKARANARAYANAN V., GROSS R., RAO M.S. Ramachandra,
Effect of rare earth ion substitution on the magnetic and transport properties of $\text{Pr}_{0.7}\text{RE}_{0.04}\text{Sr}_{0.26}\text{MnO}_3$ (RE = Er, Tb and Ho).
European Phys. J. B, submitted for publication (06/2003).
32. PHILIPP J.B., MAJEWSKI P., REISINGER D., GEPRÄGS S., OPEL M., ERB A., ALFF L., GROSS R.,
Magnetoresistance and magnetic properties of the double perovskites.
Acta Physica Polonica A, accepted for publication (09/2003).

33. UHLIG K.,
"Dry" dilution refrigerator with pulse-tube precooling.
Cryogenics, accepted for publication (2003).
34. GÖNNENWEIN S.T.B., HÜBL H., STUTZMANN M., BRANDT M.S., OPEL M., PHILIPP J.B., GROSS R., KOEDER A., SCHOCH W., WAAG A.,
Spin wave investigation of the macroscopic magnetic properties of the ferromagnetic semiconductor $\text{Ga}_{1-x}\text{Mn}_x\text{As}$.
Phys. Rev. B, submitted for publication (2003).
35. LERF A., CHAPKOVA P.,
Dye/inorganic nanocomposites.
Encyclopedia of Nanosciences, in press (2003).
36. PÉREZ-RODRIGUEZ J.L., POYATO J., JIMÉNEZ DE HARO M.C., PÉREZ-MAQUEDA L.A., LERF A.,
Thermal decomposition of ammonia vermiculite from Santa Olalla and its relation to the metal ion distribution in the octahedral layer.
Phys. Chem. Miner., accepted for publication (2003).
37. JIMÉNEZ DE HARO M.C., MARTINEZ BLANES J.M., POYATO J., PÉREZ-MAQUEDA L.A., LERF A., PÉREZ-RODRIGUEZ J.L.,
Effects of mechanical treatment and exchanged cation on the microporosity of a vermiculite.
J. Phys. Chem. Sol., in press (2003).
38. LERF A.,
Different modes and consequences of electron transfer in intercalation compounds.
J. Phys. Chem. Sol., in press (2003).
39. LERF A., WAGNER F.E., POYATO J., PÉREZ-RODRIGUEZ J.L., PÉREZ-RODRIGUEZ L.A.,
Reduction Reactions in Hydrazinium and Ammonium Vermiculites from Spain induced by heating.
J. Mater. Chem., submitted for publication (2003).
40. GOLOV A.I., EINZEL D., LAWES G., MATSUMOTO K., PARPIA J.M.,
Dissipation Mechanisms Near the Superfluid ^3He Transition in Aerogel.
Phys. Rev. Lett., submitted for publication, (2003).
41. EINZEL D., MANSKE D.,
Electronic Raman Response in Anisotropic Metals.
Phys. Rev. (Brief Reports), submitted for publication (2003).
42. BROWN S.P., CHARALAMBOUS D., JONES E.C., FORGAN E.M., ERB A., KOHLBRECHER J.,
Observation of a Triangular to Square Flux Lattice Phase Transition in $\text{YBa}_2\text{Cu}_3\text{O}_7$.
Phys. Rev. Lett., submitted for publication (2003).
43. BIBERACHER W., CHRIST P., KARTSOVNIK M.V., ANDRES D., MÜLLER H., KUSHCH N.,
Anisotropic susceptibility of $\alpha - (\text{BEDT} - \text{TTF})_2\text{KHg}(\text{SCN})_4$.
Journal de Physique IV (France), accepted for publication (2003).
44. KARTSOVNIK M.V., ANDRES D., BIBERACHER W., GRIGORIEV P.D., SCHUBERTH E.A., MÜLLER H.,
New electronic phase transitions in $\alpha - (\text{BEDT} - \text{TTF})_2\text{KHg}(\text{SCN})_4$.
Journal de Physique IV (France), accepted for publication (2003).
45. KARTSOVNIK M., ANDRES D., GRIGORIEV P., BIBERACHER W., MÜLLER H.,
Interplay between the orbital quantization and Pauli effect in a charge-density-wave organic conductor.
Physica B, accepted for publication (2003).
46. SCHUBERTH E.A., MILLAN-CHACARTEGUI C., SCHÖTTL S.,
Pulsed NMR in the Nuclear Spin Ordered Phases of Solid ^3He in a Silver Sinter.
J. Low Temp. Phys. accepted for publication (2003).
47. FISCHER F., GRAYSON M., SCHUBERTH E.A., SCHUH D., BICHLER M., ABSTREITER G.,
New Anisotropic Behavior of Quantum Hall Resistance in (110) GaAs Heterostructures at mK Temperatures and Fractional Filling Factors.
Physica E, submitted for publication (2003).
48. RAMA N., PHILIPP J.B., OPEL M., CHANDRASEKARAN K., SANKARANARAYANAN V., GROSS R., RAO Ramachandra M.S.,
Study of Magnetic properties of A_2BNbO_6 (A=Ba, Sr, (BaSr) and B= Fe and Mn) double perovskites.
IEEE Trans. Magn., submitted for publication (10/2003).

49. SIMON J., WALTHER T., MADER W., KLEIN J., REISINGER D., ALFF L., GROSS R.,
Diffusion and segregation effects in doped manganite/titanate heterostructures.
Appl. Phys. Lett., submitted for publication (10/2003).

Completed and ongoing Ph.D. and Diploma Theses

Ph.D. Theses

1. **Raman Scattering Study of Electronic Correlations in Cuprates: Observation of an Unconventional Metal-Insulator Transition**
Francesca Venturini, April 2003
2. **Spinabhängiger Transport in Übergangsmetalloxiden**
Jan Boris Philipp, Juli 2003.
3. **Rampenkontakte auf der Basis von supraleitenden und magnetischen Übergangsmetalloxiden**
Mitja Schonecke, seit Dezember 1998
4. **Spinabhängiger Transport und Quanteninterferenzeffekte in mesoskopischen metallischen Systemen**
Jürgen Schuler, seit Dezember 1998.
5. **Symmetrie des Ordnungsparameters und Pseudogap-Verhalten in Hochtemperatur-Supraleitern**
Bettina Welter, seit August 2000.
6. **Elektronische und magnetische Eigenschaften von organischen Metallen und Supraleitern**
Dieter Andres, seit September 2000.
7. **Heteroepitaktische Schichtstrukturen aus oxidischen Materialien**
Daniel Reisinger, seit Oktober 2000.
8. **Herstellung und Charakterisierung von supraleitenden Quantenbits**
Frank Deppe, seit April 2002.
9. **Physik elektronendotierter Kupratsupraleiter**
Yoshiharu Krockenberger, seit Oktober 2003.
10. **Spininjektion in Halbleiter mit ferromagnetischen Oxiden**
Petra Majewski, seit November 2002.
11. **Herstellung und Charakterisierung supraleitender Quantenbits**
Chiara Coppi, seit April 2003.
12. **Raman scattering in materials with quantum phase transitions**
Leonardo Tassini, seit April 2003.
13. **Supraleitende Quantenbits mit π -Josephson-Kontakten für die Quanteninformationsverarbeitung**
Matteo Mariani, seit November 2003.
14. **Wachstum und Physik künstlicher magnetischer Heterostrukturen**
Karl Nielsen, seit Dezember 2003.

Diploma, Bachelor, Master Theses

1. **Patterned Mask Characterization Using EUV Scatterometry**
Jan Perlich, April 2003.
2. **Mn-dotiertes ZnO - ein ferromagnetischer Halbleiter?**
Karl Nielsen, November 2003.
3. **Herstellung und Charakterisierung von supraleitenden Quantenbits**
Markus Tober, seit Juni 2002.
4. **Magnetisierungsmessungen an festem ^3He bei ultratiefen Temperaturen**
Matthias Kath, seit April 2003.
5. **Dotierungsexperimente an ferromagnetischen Doppelperovskiten**
Stephan Geprägs, seit Juni 2003.
6. **Tiefenexperimente an supraleitenden Quantenbits**
Georg Wild, seit Juni 2003.
7. **Untersuchung der Spinpolarisation ferromagnetischer Oxide mittels Ferromagnet/Supraleiter-Tunnelkontakten**
Stephanie Wagner, seit Juli 2003.
8. **Herstellung supraleitender Quantenbits mittels Elektronenstrahl-Lithographie**
Heribert Knoglinger, seit August 2003.
9. **Thermodynamische Untersuchung einer tankinternen Hochdruckpumpe für LH_2**
Florian Kuhn, seit Oktober 2003.
10. **Tunnelspektroskopie an elektrondotierten Hochtemperatur-Supraleitern**
Andreas Winkler, seit Dezember 2003.
11. **Ferromagnetische Tunnelkontakte auf Basis von Doppelperowskiten**
Andrea Boger, seit Dezember 2003.
12. **Experimente zur Spinpolarisation von Magnetit**
Suleman K. Qureshi, seit Dezember 2003.

Research Projects and Cooperations

Many of our research projects have benefited from the collaboration with external groups via joint research projects, individual collaborations, exchange programs and visitors. Several collaborations are based on joint projects which are financially supported by different organizations (see list below). A large number of collaborations also exists with several universities and other research institutions without direct financial support. These are also listed below.

Funded Projects

Deutsche Forschungsgemeinschaft: Sonderforschungsbereiche

Sonderforschungsbereich 631: Festkörperbasierte Quanteninformationsverarbeitung: Physikalische Konzepte und Materialaspekte

1. Teilprojekt A3/A4: Supraleitende Bauelemente mit π -Kontakten als Grundelemente für Quanteninformationssysteme
Gross, Alff, Marx
2. Teilprojekt C5: Spinabhängiger Transport in nanostrukturierten Festkörpern
Marx, Gross, Opel
3. Teilprojekt S: Verwaltung des Sonderforschungsbereichs
Gross

Deutsche Forschungsgemeinschaft – Normalverfahren

1. Untersuchung des niederfrequenten $1/f$ Rauschens in Josephson-Kontakten aus Hochtemperatur-Supraleitern zur Charakterisierung elementarer Rauschzentren und Klärung der Transportmechanismen
(A. Marx und R. Gross, Az. Ma 1953/1-1+2)
2. Heteroepitaxie von Übergangsmetalloxiden
(L. Alff und R. Gross, Az. Al 560/1-1+2)
3. Kristalline organische Metalle und Supraleiter: Synthese und elektronische Eigenschaften, gefördert von der DFG und der russischen Stiftung für Grundlagenforschung (RFFI)
(W. Biberacher, WMI, und N. Kushch, Institut für Probleme der chemischen Physik, Cernogolovka, Az.: 436 RUS 113/592/0)
4. Untersuchung des Wechselwirkungspotentials in Kuprat-Supraleitern durch Vergleich verschiedener spektroskopischer Methoden
(R. Hackl, Az. HA 2071/2-1+2)
5. Neue funktionale Schichtsysteme auf der Basis künstlicher heteroepitaktischer Mehrlagenstrukturen aus Übergangsmetalloxiden
im Rahmen des Schwerpunktprogramms 1157 *Integrierte elektrokeramische Funktionsstrukturen*
(R. Gross und L. Alff, Az. GR 1132/13-1)

6. Forschergruppe “Hochtemperatur-Supraleitung”
Partner: Walther-Meißner-Institut Garching (Koordination), Max-Planck-Institut für Festkörperforschung Stuttgart, Universität Würzburg, IFW Dresden
(L. Alff, A. Erb, R. Gross, R. Hackl)
geplanter Start: März 2004

Bundesminister für Bildung, Wissenschaft, Forschung und Technologie (BMBF)

1. Verbundprojekt: Ultra–schnelle und ultra–verlustarme Informationstechnik–Komponenten
Teilvorhaben: Transport– und Rauscheigenschaften von Nano–SiGe–Bauelementen
(R. Gross und A. Marx, Förderkennzeichen: 13N7902)
Partner: DaimlerChrysler AG, AMO GmbH.
2. Wissenschaftlich–Technologische Zusammenarbeit mit Indien: Ferromagnetische Oxide mit hoher Spinpolarisation
(R. Gross, Projektkennzeichen: IND 01/009)
Partner: Prof. Dr. M. S. R. Rao, Indian Institute of Technology, Madras, India.
3. Verbundprojekt: Spinelektronik und Spinoptoelektronik in Halbleitern
Teilprojekt: Ferromagnetische metallische Oxide mit hoher Spinpolarisation für die Spinelektronik
(R. Gross, Förderkennzeichen: 13N8279)
Partners: Universities of Würzburg, Hamburg, Regensburg, Hannover and Marburg, Max–Planck–Institute Halle, Siemens AG, Infineon Technologies, Aixtron GmbH.
4. Wissenschaftlich–Technologische Zusammenarbeit mit Ungarn: Transporteigenschaften hochkorrelierter Schichtsysteme
(R. Hackl, Projektkennzeichen: HUN 01/008)
Partner: Ungarische Akademie der Wissenschaften, Institut für Festkörperphysik und Optik, Prof. Dr. Istvan Tüttö.

European Union

1. European Science Foundation Network “*Thin Films for Novel Oxide Devices: THIOX*”
(R. Gross; coordination: Prof. D. Blank, University of Twente, The Netherlands)
partners: several European Universities and research facilities.
2. Research and Training of Young Researchers on the Magnetic Properties of ^3He by Means of Neutron Diffraction
(E. Schuberth; coordination: Dr. Konrad Siemensmeyer, Hahn–Meitner Institute Berlin GmbH)
European Community, Contract No.: HPRN-CT-2000-00166
Partners: Hahn–Meitner Institut, Berlin, Univ. of Florida, Royal Holloway College, London, Univ. Liverpool, CNRS, Grenoble and Univ. Paris, Saclay.
3. European Science Foundation Network “*Vortex Matter at Extreme Scales and Conditions*”
(R. Gross; coordination: Prof. Moshchalkov, Univ. Leuven)
Partners: several European Universities and research facilities.
4. High Field Infrastructure Cooperative Network
(W. Biberacher, coordination by CNRS Grenoble, contract No.: HPRI-CT-1999-40013)
Partners: in total 31 participants.

Deutscher Akademischer Austauschdienst (DAAD)

1. Projektbezogener Personenaustausch mit Spanien, Acciones Integradas Hispano-Alemanas (A. Lerf)
Centro de Investigaciones Cientificas "Isla de Cartuja", Universidad de Sevilla, Prof. Dr. Jose Luis Perez Rodriguez

Alexander von Humboldt Stiftung

1. Humboldt Forschungsstipendium "Devereaux"
(R. Hackl, Förderkennzeichen IV-USA/109800 6 STP)

INTAS

1. *Magnetic quantum oscillations in layered organic superconductors*
(W. Biberacher, Förderkennzeichen INTAS 01-0791)

Collaborations

Other collaborations without direct project funding involve:

- Technion, Israel (Prof. G. Koren, Dr. E. Polturak)
- NTT, Japan (Prof. Dr. H. Takayanagi, Dr. M. Naito)
- University of Bonn (Prof. W. Mader)
- Tokyo Institute of Technology, Japan (Prof. K. Koinuma)
- Materials Physics Laboratory, Helsinki University of Technology (Dr. Tero Heikkilä)
- Department of Condensed Matter Physics, The Weizmann Institute of Science, Israel (Dr. Moshe Schechter)
- Chalmers University of Technology, Gothenburg, Sweden (Prof. Dr. P. Delsing)
- University of Waterloo, Department of Physics, Ontario, Canada (Prof. Dr. T.P. Devereaux)
- Ludwig–Maximilians–University Munich, Germany (Prof. Kotthaus, Prof. von Delft, Dr. F. Wilhelm)
- University of Tübingen, Germany (Prof. R. Kleiner, Prof. D. Kölle)
- University of Würzburg, Germany (Prof. W. Hanke, Prof. L. Molenkamp)
- University of Augsburg, Germany (Prof. Dr. P. Hänggi)
- Max–Planck Institut für Metallforschung, Stuttgart (Dr. P. Wochner, Dr. A. Vigliante)
- Hungarian Academy of Sciences, Technische Universität Budapest, Budapest, Hungary (Prof. Dr. K. Kamaras, Dr. Attila Virosztek, Prof. Dr. A. Zawadowski)
- Eötvös Lorand University, Budapest, Hungary (Dr. I. Tüttö)
- Università di Roma "La Sapienza", Roma, Italy (Prof. Dr. Paolo Calvani)
- Institut für Experimentelle Physik, Slowakische Akademie der Wissenschaften, Kosice (Prof. K. Flachbart)
- Northwestern University Evanston, Illinois
- University of Florida
- Institute of Solid State Physics, Chernogolovka, Russia (Dr. R.P. Shibaeva, Prof. Dr. V. Ryazanov, Prof. Dr. Lev Vinnikov)
- Institute of Problems of Chemical Physics, Chernogolovka, Russia (Prof. Dr. O.A. Dyachenko)
- High–Magnetic–Field Laboratory, Grenoble, France (Dr. J. Sheikin)
- National Pulsed–Magnetic–Field Facility, Toulouse, France (Dr. L. Brossard)
- B. Verkin Institute for Low Temperature Research and Engineering, Kharkov, Ukraine (Prof. V.G. Peschansky)
- Institute for Material Science, Barcelona, Spain (Prof. E. Canadell)
- Department of Chemistry, University of Cambridge, UK (Dr. Jacek Klinowski)
- Institut für Technologie Anorganischer Stoffe der TU Graz, Austria (Prof. Besenhard)
- University of Nantes, France (Prof. M. Danot)
- Université Paris Sud, Orsay, France (Prof. J.P. Pouget, Dr. P. Fourry-Leylekian)
- Landau Institute for Theoretical Physics, Chernogolovka, Russia (Dr. P. Grigoriev)

Stays abroad

Extended visits of members of the Walther-Meissner-Institute at foreign research laboratories:

1. **Rudolf Hackl**

Università di Roma La Sapienza, Istituto Nazionale di Fisica della Materia (Prof. Paolo Calvani and Prof. Carlo Di Castro) Rom, Italien
02. - 03. 01. 2003

2. **Rudolf Gross**

Indian Institute of Technology (Prof. Dr. M. S. R. Rao), Madras, Indien
12. 12. – 20. 12. 2003

3. **Rudolf Hackl**

Technical University of Budapest and Research Institute for Solid State Physics (Profs. I. Tüttö, A. Virosztek, A. Zawadowski), Budapest, Ungarn
20. 02. – 26. 02. 2003

4. **Rudolf Hackl**

DFG-OTKA Workshop, Technical University of Budapest and Research Institute for Solid State Physics (Profs. I. Tüttö, A. Virosztek, A. Zawadowski), Budapest, Ungarn
15. 05. – 21. 05. 2003

5. **Rudolf Hackl**

Technical University of Budapest and Research Institute for Solid State Physics (Profs. I. Tüttö, A. Virosztek, A. Zawadowski), Budapest, Ungarn
06. 12. – 14. 12. 2003

6. **Matthias Opel**

Materials Science Research Centre, Indian Institute of Technology Madras, India (Prof. Dr. M.S. Ramachandra Rao)
12. 01. – 09. 02. 2003

7. **Jan B. Philipp**

Materials Science Research Centre, Indian Institute of Technology Madras, India (Prof. Dr. M.S. Ramachandra Rao)
12. 01. – 09. 02. 2003

8. **Mark Kartsovnik, Dieter Andres, Werner Biberacher**

High Magnetic Field Laboratory, Grenoble, France
02. 02. – 09. 02. 2003

9. **Mark Kartsovnik, Werner Biberacher**

High Magnetic Field Laboratory, Grenoble, France
28. 05. – 05. 06. 2003

Conference Talks and Seminar Lectures

Lambert Alff

1. **Hidden pseudogap in electron doped high-temperature superconductors**
24. - 28. 02. 2003
Korrelationstage, Dresden
2. **Electron doped high-temperature superconductors: The dark side of the phase diagramm**
24. - 28. 03. 2003
DPG Frühjahrstagung, Dresden
3. **What can we learn from electron-doped high-temperature superconductors?**
04. 07. 2003
FU Berlin
4. **Thin films of magnetoresistive oxide materials for spintronics: Technology aspects and physical properties**
22. 07. 2003
MPI für Metallforschung, Stuttgart
5. **Korngrenzen in oxidischen Materialien: Von Josephson-Kontakten mit Hochtemperatur-Supraleitern zu Tunnelmagnetowiderstandsbauelementen**
16. 09. 2003
Vienna University of Technology
6. **Korngrenzen in oxidischen Materialien: Von Josephson-Kontakten mit Hochtemperatur-Supraleitern zu Tunnelmagnetowiderstandsbauelementen**
23. 10. 2003
Ruhr-Universität Bochum, Seminar des Graduiertenkollegs 384
7. **Korngrenzen in oxidischen Materialien: Von Josephson-Kontakten mit Hochtemperatur-Supraleitern zu Tunnelmagnetowiderstandsbauelementen**
06. 11. 2003
Universität Karlsruhe

Dietrich Einzel

1. **Analytic Two-Fluid Description of Unconventional Superconductivity**
11. 01. 2003
Kommissionssitzung WMI, Garching
2. **Superconductivity and Superfluidity**
30. 10. 2003
Festkörperkolloquium der TUM, Garching

Rudolf Gross

1. **Magnetoresistance and magnetic properties of the double perovskites**
R. Gross
E-MRS 2003 Fall Meeting,
September 15 - 19, 2003, Warsaw, Poland.
2. **Physics and technology of metallic nanostructures**
R. Gross
Workshop Nanoscience and Nanotechnology
September 29, 2003, Munich, Germany.
3. **The double perovskite system A_2CrWO_6**
R. Gross
International Workshop Imagine Magnetic and Superconducting Materials,
October 23 - 25, 2003, Barcelona, Spain.

4. Metallic Nanostructures

R. Gross
Workshop *Nanotechnology in Bavaria*
December 1, 2003, Unterschleißheim, Germany.

5. Hardware concepts for solid state based quantum computing

R. Gross
Tutorial at the 12th *International Symposium on the Physics of Semiconductor Devices*
December 15, 2003, Madras, India.

6. Conductance of superconductor/normal metal nanostructures

R. Gross
12th *International Symposium on the Physics of Semiconductor Devices*
December 16 - 20, 2003, Madras, India.

7. Spinelectronics based on half-metallic oxides

December 18, 2003
Materials Science Research Center, Indian Institute of Technology, Madras, India.

Rudolf Hackl**1. The diagram of the cuprates: single- vs. many-particle properties**

14. - 20. 06. 2003
International Conference on *Dynamic Inhomogenities in Complex Oxides*, Bled, Slovenien

2. The phase diagram of the cuprates: surprises at high doping level

02. 04. 2003
Ecole Polytechnique Federale de Lausanne, Schweiz

3. Raman scattering experiments on electronic excitations in copper-oxygen compounds

05. 12. 2003
University of Zagreb, Croatia

4. A Raman study of competing ordering phenomena in cuprates

12. 12. 2003
Budapest University of Technology and Economics, Budapest, Ungarn

Mark Kartsovnik**1. New electronic phase transitions in $\alpha - (\text{BEDT} - \text{TTF})_2\text{KHg}(\text{SCN})_4$**

21. - 26. 09. 2003
ISCOM, Port Bourgenay, France

Anton Lerf**1. Different modes and consequences of electron transfer in intercalation compounds**

01. - 05. 06. 2003
13th International Symposium on Intercalation Chemistry, Poznan

Karl Neumaier**1. Insertable dilution refrigerators**

02. 10. 2003
Institute of Experimental Physics, Slovak Academy of Sciences, Kosice, Slovakei

Matthias Opel**1. Raman Scattering in high-Tc Superconductors**

22. 01. 2003
Materials Science Research Centre, Indian Institute of Technology, Madras, India

Jan Boris Philipp

1. **Spin-polarized transport in metal oxides**
22. 01. 2003
Materials Science Research Centre, Indian Institute of Technology, Madras, India
2. **The double perovskite system Sr_2CrWO_6**
28. 01. 2003
Solid State & Structural Chemistry Unit, Indian Institute of Science, India

Erwin Schuberth

1. **Pulsed NMR and Static Magnetization Measurements**
09. - 12. 05. 2003
Workshop on Neutron Scattering from Solid ^3He : Advances of the Experiment in Munich: Hahn-Meitner Institut, Berlin
2. **Kernspinordnung in festem ^3He : NMR und Neutronenstreuexperimente**
26. 06. 2003
Festkörperkolloquium, TU München
3. **Pulsed NMR in the Nuclear Spin Ordered Phases of Solid ^3He in a Silver Sinter**
03. - 08. 08. 2003
Quantum Fluids and Solids Conference, Albuquerque, USA
4. **Eigenschaften von Festkörpern und Flüssigkeiten bei sehr tiefen Temperaturen**
28. 10. 2003
Lüscher Lectures über Kondensierte Materie, Lehrerfortbildung, Dillingen

Kurt Uhlig

1. **$^3\text{He}/^4\text{He}$ dilution refrigerator with pulse-tube precooling**
30. 03. - 02. 04. 2003
University of Twente
2. **Dilution refrigerator precooled by pulse-tube fridge**
07. 11. 2003
European Network on Applied Cryodetectors, MPI für Physik, München

Francesca Venturini

1. **Evidence for a metal-insulator transition in the cuprates: new Raman results**
24. - 28. 02. 2003
Korrelationstage, Dresden
2. **Evidence for a metal-insulator transition in overdoped cuprates: new Raman results**
24. - 28. 03. 2003
DPG Frühjahrstagung, Dresden
3. **Quantitative Comparison of Different Spectroscopies**
15. - 16. 05. 2003
DFG-OTKA Workshop on Promoting Hungarian-German Cooperation in Physics, Budapest, Germany
4. **Evidence for a metal-insulator transition in the cuprates: new Raman results**
03. 04. 2003
ETH-Zürich, Hönggerberg, Schweiz

Seminars, Courses, Lectures and other Scientific Activities

The WMI Seminars

The Friday Seminar — Walther-Meissner-Seminar on Current Topics in Low Temperature Physics

1. **Supraleitung, d -Dichtewelle und elektronische Raman-Streuung in Hoch- T_c -Supraleitern**
Dr. Roland Zeyher, MPI-FKF, Stuttgart
10. 01. 2003
2. **Ballistic Quasiparticles in Helium Quantum Fluids**
Dr. Dietrich Einzel, WMI Garching
24. 01. 2003
3. **Macroscopic Quantum Tunneling in Superconductor -2DEG- Superconductor Josephson Junctions**
Dr. Thilo Bauch, Chalmers Technical Highschool, Göteborg University
13. 02. 2003
4. **Theoretical and practical aspects of pulse-tube refrigeration**
Dr. I.A. Tanaeva, Eindhoven University of Technology
14. 02. 2003
5. **Electrodynamics in correlated systems**
Prof. Dr. Leonardo Degiorgi, Solid State Physics Lab, ETH Zürich
17. 02. 2003
6. **Borocarbide superconductors: their discovery, current status and our recent work**
Prof. Dr. L.C. Gupta, Tata Institute of Fundamental Research, Mumbai, India
28. 02. 2003
7. **Properties and prospects of the electron-doped manganites $\text{La}_{1-x}\text{Ce}_x\text{MnO}_3$**
Dr. Steffen Wirth, MPI für chemische Physik fester Stoffe, Dresden
11. 04. 2003
8. **MiniGRAIL - the first spherical gravitational wave antenna**
Dr. Arlette de Waard, Kamerlingh-Onnes Laboratory, Leiden University
16. 05. 2003
9. **Mechanisms of π -transitions in SFS Josephson junctions**
Dr. A. Golubov, University of Twente
23. 05. 2003
10. **Plastic Electronics - Dünnschichttransistoren aus organischen Werkstoffen**
Dr. Barbara Stadlober, Joanneum Research mbH, Graz
02. 06. 2003
11. **Experimental investigation of the persistent current qubits**
Dr. E. Ilichev, IPHT, Jena
06. 06. 2003
12. **MRI-Magnete auf dem Weg zur unsichtbaren Kryogenik**
Dr. Florian Steinmeyer, Siemens AG, Erlangen, Medical Solutions
13. 06. 2003
13. **Effect of substitution of RE-ions on the magnetotransport properties in CMR manganites**
Prof. Dr. M.S. Ramachandra Rao, Indian Institute of Technology, Madras
16. 06. 2003
14. **Neuere Ergebnisse der inelastischen Neutronenstreuung zur Elektron-Phonon-Kopplung in Hochtemperatur-Supraleitern**
Dr. Lothar Pintschovius, Forschungszentrum Karlsruhe
23. 06. 2003
15. **Radio-frequency SQUID amplifier: applications in reading out charge QUBITs**
Matteo Mariani, Chalmers University of Technology
25. 06. 2003
16. **Condensation energy and quasiparticle dispersion in superconductors with phase fluctuations**
Dr. Thomas Eckl, Universität Würzburg

27. 06. 2003
17. **Low temperature properties of the heavy fermion semiconductor SmB_6**
Dr. Karol Flachbart, Institute Exp. Physics, Slovak Academy Science, Kosice, Slovakia
30. 06. 2003
 18. **Spin and charge correlations in low-dimensional organic solids**
Prof. Dr. Michael Lang, Johann-Wolfgang-Goethe-Universität Frankfurt
04. 07. 2003
 19. **Theory of Light Scattering in Strongly Correlated Quantum Systems**
Prof. Dr. T.P. Devereaux, Dept. of Physics, University of Waterloo
14. 07. 2003
 20. **Electronic Transport of YBCO Grain Boundaries above and below T_c**
Dr. Christof W. Schneider, Experimental Physics VI, Electronic Correlations and Magnetism, University of Augsburg
18. 07. 2003
 21. **Heat conduction in the vortex state of NbSe_2 : evidence for multi-band superconductivity**
Prof. Dr. Makariy Tanatar, Dept. of Physics, University of Toronto, Canada
29. 09. 2003
 22. **Pomeranchuk instability, soft Fermi surfaces and a new route to non-Fermi liquid behavior**
Prof. Dr. Walter Metzner, MPI für Festkörperforschung, Stuttgart
24. 10. 2003
 23. **Sind physikalische Observable prinzipiell auf fundamentale Theorien reduzierbar?**
Prof. Dr. Harald Atmospacher, Institut für Physik, Universität Freiburg
31. 10. 2003
 24. **Elementary excitations in hole and electron-doped cuprates: kink feature and resonance peak**
Dr. Dirk Manske, MPI für Festkörperforschung, Stuttgart
14. 11. 2003
 25. **Superconductivity in non-doped cuprates: breakdown of the doped Mott insulator scenario for high- T_c superconductivity**
Prof. Michio Naito, NTT Basic Research Laboratory, Atsugi, Kanagawa, Japan
17. 11. 2003
 26. **Josephson Vortices in Superconducting Tunnel Junctions**
Prof. Dr. Alexey Ustinov, Phys. Institut III, Universität Erlangen-Nürnberg
21. 11. 2003
 27. **Halbleiter-Spinelektronik: Spininjektion, Spintransport und Spinkohärenz in Halbleiterheterostrukturen**
Dr. Bernd Beschoten, II. Phys. Institut, RWTH Aachen
28. 11. 2003
 28. **Elektronische Transporteigenschaften dünner oxidischer Perowskitschichten**
Priv.-Doz. Dr. Gerhard Jakob, Institut für Physik, Johannes-Gutenberg Universität Mainz
05. 12. 2003
 29. **Elektrochemische Untersuchungen der Defektchemie von perowskitischen Oxiden**
Prof. Dr. W. Sitte, Institut für Phys. Chemie, Montan-Universität, Leoben
09. 12. 2003
 30. **Magnetismus und Spin in hybriden Schichtsystemen: vom de Haas-van Alphen-Effekt zur Spintronik**
Priv.-Doz. Dr. Dirk Grundler, Institut für Angew. Physik und Zentrum für Mikrostrukturforschung, Universität Hamburg
12. 12. 2003

The Tuesday Seminar – SS 2003

1. **Aktive Galaxienkerne**
Petra Majewski, Walther-Meissner-Institut, Garching
08. 04. 2003
2. **Elektronspinresonanz in ZnO:Mn**
Tobias Graf, Walter-Schottky-Institut, Garching
15. 04. 2003

3. **Neues vom Doppelperovskit Sr_2CrWO_6**
Boris Philipp, Walther-Meissner-Institut, Garching
06. 05. 2003
4. **Phase diagram of the electron-doped superconductor $\text{La}_{2-x}\text{Ce}_x\text{CuO}_4$**
Dr. Akihito Sawa, Universität Augsburg
13. 05. 2003
5. **$^3\text{He}/^4\text{He}$ -Mischkühler mit Pulsrohr-Vorkühlung**
Kurt Uhlig, Walther-Meissner-Institut, Garching
20. 05. 2003
6. **Elektronenübertrag in Schichtverbindungen**
Anton Lerf, Walther-Meissner-Institut, Garching
27. 05. 2003
7. **Kristallzüchtung im Spiegelofen**
Andreas Erb, Walther-Meissner-Institut, Garching
03. 06. 2003
8. **New optical properties of quantum dots: beyond the standard atom picture**
Prof. Dr. Khaled Karrai, Center for NanoScience
17. 06. 2003
9. **Extraordinary magnetoresistance in narrow-gap semiconductors: fundamental physics and practical applications**
Prof. Dr. Stuart Solin, Washington University, St. Louis, USA
08. 07. 2003
10. **Heteroepitaxie von Übergangsmetalloxiden**
Mitja Schonecke, Walther-Meissner-Institut, Garching
15. 07. 2003
11. **Mn-dotiertes Zinkoxid - ein ferromagnetischer Halbleiter?**
Karl Nielsen, Walther-Meissner-Institut, Garching
22. 07. 2003

Topical Seminar on Quantum Information Processing – WS 2002/2003

This topical seminar was held for students in the 7th and 8th semester. It was part of the special physics courses in magnetism and magnetoelectronics as well as on superconductivity and low temperature physics offered by the WMI.

1. **Einzelne Quantenbits — Präparation, Messung, Manipulation, Kontrolle**
Dietrich Einzel
26. 11. 2002
2. **Zwei-Qubit-Systeme — Verschränkung, EPR-Paradoxon, Bell-Ungleichungen**
Dominik Bauer
03. 12. 2002
3. **Quantenkryptographie und Teleportation**
Stefan Ahlers
10. 12. 2002
4. **Quantencomputing — Modelle, Gatter, Algorithmen**
Sebastian Bauer
17. 12. 2002
5. **Der Ionenfallen-Quantencomputer**
M. Janoschek
07. 01. 2003
6. **Der NMR-Quantencomputer**
Martin Stadlbauer
14. 01. 2003
7. **Qubits basierend auf Spins in Nanostrukturen**
Dominik Heiss
21. 01. 2003

8. **Supraleitende Qubits I: Ladungs-Qubits**
Stefanie Wagner
28. 01. 2003
9. **Supraleitende Qubits II: Fluss/Phasen-Qubits**
Markus Tober
04. 02. 2003

Topical Seminar on Mesoscopic Systems and Nanotechnology – WS 2003/2004

This topical seminar is held for students in the 7th and 8th semester. It is part of the special physics course on superconductivity and low temperature physics offered by the WMI.

1. **Einführung in die Physik mesoskopischer Systeme: Längen-, Energie- und Zeitskalen**
Achim Marx
18. 11. 2003
2. **Herstellungsverfahren für nanostrukturierte Festkörper**
Edwin Menzel
25. 11. 2003
3. **Quanteninterferenzeffekte bei Ladungstransport in mesoskopischen Systemen: Aharonov-Bohm-Effekt, Schwache Lokalisierung, universelle Leitwertfluktuationen**
Bernhard Musch
02. 12. 2003
4. **Der Quantenhalleffekt**
M. Schmidt
09. 12. 2003
5. **Ladungsquantisierungseffekte in kleinen Tunnelkontakten: Der Einzelelektronen-Transistor**
Holger Specht
16. 12. 2003
6. **Mesoskopische Supraleiter/Normalleiter/Supraleiter Systeme**
Andreas Brandlmaier
13. 01. 2004
7. **Physik ultrakleiner Josephson-Kontakte**
Chiara Coppi
20. 01. 2004
8. **Physikalische Eigenschaften von Kohlenstoff-Nanoröhrchen**
A. Kaniber
27. 01. 2004
9. **Elektronischer Transport durch atomare Punktkontakte**
Christian Jäger
03. 02. 2004
10. **Molekulare Elektronik**
Thomas Niemczyk
10. 02. 2004

Lectures

Lambert Alff

- WS 2002/2003
 - Magnetismus (Introduction to Magnetism)
 - Übungen zu Experimentalphysik III in Gruppen (Experimental Physics III, exercises) (with R. Gross)
- SS 2003
 - Übungen zu Experimentalphysik IV in Gruppen (Experimental Physics IV, exercises) (with R. Gross)
- WS 2003/2004
 - Magnetismus (Introduction to Magnetism)
 - Übungen zu Experimentalphysik III in Gruppen (Experimental Physics IV, exercises) (with R. Gross)

Dietrich Einzel

- WS 2002/2003
 - Mathematische Methoden der Physik I (Mathematical Methods of Physics I)
 - Übungen zu Mathematische Methoden der Physik I (Mathematical Methods of Physics I, Problem Sessions)
- SS 2003
 - Mathematische Methoden der Physik II (Mathematical Methods of Physics II)
 - Übungen zu Mathematische Methoden der Physik II (Mathematical Methods of Physics II, Problem Sessions)
 - Theorie der Supraleitung (Theory of Superconductivity)
 - Akademie Unterwegs (Seminar organisiert von den Sprechern der Wissenschaftler der BAdW)
- WS 2003/2004
 - Mathematische Methoden der Physik I (Mathematical Methods of Physics I)
 - Übungen zu Mathematische Methoden der Physik I (Mathematical Methods of Physik I, Problem Sessions)
 - Farbe (Seminar organisiert von den Sprechern der Wissenschaftler der BAdW)

Rudolf Gross

- WS 2002/2003
 - Experimentalphysik III (Experimental Physics III)
 - Übungen zu Experimentalphysik III in Gruppen (Experimental Physics III, exercises)
 - Magnetoelektronik II (Magnetoelectronics II, with A. Marx)
 - WMI-Seminar über aktuelle Fragen der Tieftemperatur-Festkörperphysik (WMI Seminar on Current Topics of Low Temperature Solid State Physics) (with D. Einzel)
 - Seminar über Quanteninformationsverarbeitung (Seminar on Quantum Information Processing)
- SS 2003
 - Magnetoelektronik I (Magnetoelectronics I, with A. Marx)
 - Experimentalphysik IV (Experimental Physics IV)
 - Übungen zu Experimentalphysik IV in Gruppen (Experimental Physics IV, exercises)
 - WMI-Seminar über aktuelle Fragen der Tieftemperatur-Festkörperphysik (WMI Seminar on Current Topics of Low Temperature Solid State Physics) (with D. Einzel)

- WS 2003/2004
- Applied Superconductivity: Josephson Effects and Superconducting Electronics
 - WMI-Seminar über aktuelle Fragen der Tieftemperatur-Festkörperphysik (WMI Seminar on Current Topics of Low Temperature Solid State Physics) (with D. Einzel)
 - Festkörperkolloquium (Colloquium on Solid State Physics (with D. Einzel)
 - Seminar über Mesoskopische Systeme und Nanotechnologie (Seminar on Mesoscopic Systems and Nanotechnology)

Anton Lerf

- WS 2002/2003
- Nanostrukturierte Materie (Nanostructured Materials)
 - Einführung in die Festkörperchemie (mit Prof. Köhler), (Introduction to Solid State Chemistry)
- WS 2003/2004
- Einführung in die Festkörperchemie (mit Prof. Köhler), Introduction to Solid State Chemistry)
 - Stoffströme in Natur und Technik (mit Prof. Köhler), Material fluxes in nature and technology)

Erwin Schubert

- WS 2002/2003
- Experimente bei tiefsten Temperaturen (Experiments at very low temperatures)
- SS 2003
- Angewandte Physik: Supraleitung und Tieftemperaturphysik II (Applied Physics: Superconductivity and Low Temperature Physics II)
- WS 2003/2004
- Experimente bei tiefsten Temperaturen (Experiments at very Low Temperatures)

Staff of the Walther-Meissner-Institute

Director

Prof. Dr. Rudolf Gross

Technical Director

Dr. Karl Neumaier

Administration/Secretary's Office

Jutta Laaser

Emel Dönertas

Scientific Staff

Dr. habil. Lambert Alff

Dr. Werner Biberacher

Dr. habil. Dietrich Einzel

Dr. habil. Andreas Erb

Dr. habil. Rudi Hackl

Dr. Mark Kartsovnik

Prof. Dr. Anton Lerf

Dr. Achim Marx

Dr. Matthias Opel

Dr. Christian Probst

Dr. habil. Erwin Schubert

Dr. Kurt Uhlig

Dipl.-Phys. Dieter Andres

Dipl.-Phys. Boris Philipp

Dipl.-Phys. Daniel Reisinger

Dipl.-Phys. Mitja Schonecke

Dipl.-Phys. Jürgen Schuler

Dipl.-Phys. Francesca Venturini

Dipl.-Phys. Bettina Welter

Dipl.-Phys. Chiara Coppi

Dipl.-Phys. Petra Majewski

Dipl.-Phys. Yoshiharu Krockenberger

Dipl.-Phys. Karl-Wilhelm Nielsen

Dipl.-Phys. Leonardo Tassini

Dipl.-Phys. Matteo Mariantoni

Technical Staff

Thomas Brenninger

Joachim Geismann

Gabrielle Görblich

Ulrich Guggenberger

Dieter Guratzsch

Wolfgang Hehn

Josef Höss

Julius Klaus

Robert Müller

Jan Naundorf

Georg Nitschke

Walter Nitschke

Christian Reichlmeier

Harald Schwaiger

Helmut Thies

Siegfried Wanninger

Assistants

Sybilla Plöderl

Brigitte Steinberg

Permanent Guests

Prof. Dr. B. S. Chandrasekhar

Dr. Robert Doll

Prof. Dr. Schöllhorn

Guest Researchers

1. Prof. Dr. B.S. Chandrasekhar
permanent guest
2. Dr. Robert Doll
permanent guest
3. Prof. Dr. Schöllhorn
permanent guest
4. Prof. Dr. Carlo di Castro, Universität Rom, Italy
29. 01. – 02. 02. 2003
5. Dr. Thilo Bauch, Chalmers Technical Highschool, Göteborg University
11. 02. – 13. 02. 2003
6. Dr. Pavel Grigoriev, Hochfeldlabor, Grenoble
25. 02. – 04. 03. 2003
7. Dipl.-Phys. S. Fagot, Université Paris Sud, Orsay, France
10. 03. – 23. 03. 2003
8. Dr. Attila Viroztek, Technische Universität, Budapest
05. 05. – 14. 05. 2003
9. Prof. Dr. M.S. Ramachandra Rao, Materials Science Research Centre, Chennai, India
15. 05. – 08. 07. 2003
10. Dr. Karol Flachbart, Institut f. Exp. Physik, Slowakische Akademie der Wissenschaften, Kosice, Slowakei
27. 05. – 27. 06. 2003, 24. 11. – 08. 12. 2003
11. Prof. Dr. Thomas Peter Devereaux, University of Waterloo
01. 06. – 31. 08. 2003
12. Prof. D.D. Sarma, Indian Institute of Science, Indien
03. 06. – 06. 06. 2003
13. Prof. Dr. Patrik Fazekas, Central Research Institute for Solid State Physics and Optics, Budapest
11. 06. – 14. 06. 2003
14. Prof. Dr. Juan Poyato Ferrera, Instituto de Ciencia de Materiales, Sevilla, Spain
01. 07. – 31. 07. 2003
15. Prof. Dr. Jeevak M. Parpia, Dept. of Physics, Cornell University, USA
20. 07. – 26. 07. 2003
16. Dr. V. Krinichny, Institute for Problems of Chemical Physics, Chernogolovka, Russia
04. 08. – 10. 08. 2003
17. Dr. Natalya Kushch, Institute of Problems of Chemical Physics, Chernogolovka, Russland
18. 09. – 25. 11. 2003
18. Dr. Makary Tanatar, Dept. of Physics, University of Toronto, Canada
27. 09. – 01. 10. 2003
19. Dr. Dirk Manske, MPI für Festkörperphysik, Stuttgart
12. 11. – 14. 11. 2003
20. Prof. Dr. Alfred Zawadowski, Budapest University
14. 11. – 30. 11. 2003
21. Prof. Dr. I. Tüttö, Central Research Institute for Solid State Physics and Optics, Budapest
13. 12. – 23. 12. 2003

Commission for Low Temperature Physics

Members of the Commission for Low Temperature Physics of the Bavarian Academy of Sciences:

Kaiser, Wolfgang, Leiter (Technische Universität München)
Brenig, Wilhelm, stellv. Leiter (Technische Universität München)
Gross, Rudolf (Walther-Meißner-Institut)
Landwehr, Gottfried (Universität Würzburg)
Hänsch, Theodor (Max-Planck Institut für Quantenoptik, Garching)
Koch, Frederick (Technische Universität München)
Kotthaus, Jörg Peter (Ludwig-Maximilians-Universität München)
Rainer, Dierk (Universität Bayreuth)
Renk, Karl Friedrich (Universität Regensburg)
Schwoerer, Markus (Universität Bayreuth)